

Fermi surface local geometry and anomalous quantum transport

Dissertation

zur Erlangung des Doktorgrades der Naturwissenschaften

(Dr. rer. nat.)

der

Naturwissenschaftlichen Fakultät II

Chemie, Physik und Mathematik

der Martin-Luther-Universität

Halle-Wittenberg

vorgelegt von

Frau **Elena Derunova**

geb. am 25.09.1989 in Voronezh, Russia

Betreuer: Dr. Mazhar N. Ali, Prof. Dr. Stuart S. P. Parkin

Gutachter:

- Prof. Dr. Stuart S. P. Parkin
- Prof. Dr. Arthur Ernst
- Prof. Dr. Jamal Berakdar

Tag der öffentlichen Verteidigung: 29.03.2022

“Пути господни неисповедимы”
(God works in mysterious ways).

Folk saying.

Contents

List of Figures	10
Introduction	11
1 Electronic eigenstates in semimetals	15
1.1 Bandstructure	15
1.2 Spin-orbit coupling	20
1.3 Semimetal classification	21
2 Computational transport theory	27
2.1 Density functional theory	27
2.2 Semiclassical transport	30
2.3 Green's functions	34
3 Introduction into topology	37
3.1 Topological spaces and manifolds	37
3.2 Tangent bundles	40
4 Topological properties of the eigenstates	43
4.1 Gauge invariance	43
4.2 Gauge induced topology and Berry curvature	46
4.3 Topological indexes, EBR, and connectivity of the eigenstates	48
4.4 Berry curvature and anomalous transport effects	51
5 Prediction of topologically driven spin Hall effect from first principles calculation	57

5.1	Crystal symmetries and gapped anti-crossings	58
5.2	Topologically driven spin Hall Effect	60
5.3	Symmetries demanded anti-crossing and spin Hall conductivity in the A15 superconductors family	63
5.4	Chemical doping and design strategy to maximize spin Hall conductivity	69
6	Fermi surface local geometry and Hall effects	73
6.1	Anti-crossings and non-differentiable Fermi surface orbits	75
6.2	Local properties of the Fermi surface	76
6.3	Hyperbolicity and anomalous orthogonal transport	79
6.4	H-index for the Fermi surface showing fundamental correlations with AHC and SHC	83
6.5	Geometrical treatment for breaking limit of anomalous Hall conductivity: example of CrPt3	85
7	Towards geometrical classes of the bandstructures	91
	Summary	99
	Supplementary information	101
	Bibliography	113
	Publications	121
	Acknowledgments	123
	Curriculum Vitae	125
	Eidesstattliche Erklärung	127

List of Figures

1.1	Representation of a function in the Fourier space. (a) Duality between momentum coordinates k and spacial coordinates x : at every fixed x a value of the wavefunction $\psi(x)$ can be expressed as a sum of the basic functions (harmonics), depending on k and drawn in the top panel in different colors. (b) Distribution of the Hamiltonian's eigenvalues in the momentum space. The vertical colored lines represents the hidden x axis for the different harmonics shown in (a).	18
1.2	Dimensionality of the momentum space and corresponding FS. (a) 1D momentum space shown as a horizontal line demands 0D FS, shown as green points. (a) 2D momentum space shown as a horizontal plane demands 1D FS, shown as green circle. (c) 3D momentum space demands the FS to be a 2D surface, which is a boundary of the Fermi sea formed by occupied states. Two components of the Fermi surface represents electron pocket, where the Fermi sea remains outside of the pocket, and hole pocket, where the Fermi sea is inside. Thus, to smoothly pass from outside to inside though the FS, the Fermi sea makes a particular geometrical feature at the passing point on the FS.	19
1.3	Degeneracies in the bandstructure of topological semimetals in one dimensional case. The Dirac point type of degeneracy shown on the left is made off two double degenerate (with Kramers degeneracy) bands crossing each other, whereas the Weyl point shown on the left is made off non degenerate bands, e.g. spin-split by turning on SOC.	22
1.4	Classification of topological semimetals in two dimensional case.	23
1.5	Degeneracy in three dimensional case appearing on the Fermi surface. The red color represents degenerate points, blue points from the valence band, green points from the conduction band.	25

List of Figures

1.6	Degeneracies on the Fermi surface for $ZrSiS$, Mn_3Sn , W_3W . (a) Isolated degeneracies in $ZrSiS$ FS. Calculated FS slice is top left, measured FS slice is bottom left. At the right side the measured bulk bandstructure confirming isolated type of degeneracy: the bulk bandstructure remains 2D up to -1.4 eV and thus its slice at the Fermi level is 1D. (b) Isolated and irregular degeneracies in Mn_3Sn . The slice of the bandstructure is shown: the orange color represents filled states, purple not filled and red color between them represents FS. The irregular degeneracies are marked as WP (Weyl point) and isolated are marked as "Fermi arc". (c) Irregular degeneracies in W_3W	26
2.1	Orbits on the FS in the magnetic field. (a) Closed orbits. (b) Open orbits. (c) Magnetic breakdown, when the orbits intersect.	31
2.2	Dynamics in momentum space induced by the electric field. (a) change of momentum within a band along the field direction. (b) Transformation of the FS as a shift along the field direction.	32
3.1	Sphere as 2D manifold: A degeneracy of the differentiation map for a sphere in 3D space, B: football as example of an atlas on the sphere that resolve degeneracy of differentiation map.	39
3.2	Schematic diagram of the construction of manifold on a topological space.	40
3.3	Construction of the tangent space. (a) Tangent vectors for a 2D band as projected into (k_x, k_y) plane (purple arrows): the tangent vector to the FS in this coordinate system has coordinates $(\partial_x = \partial\varepsilon/\partial k_x, \partial_y = \partial\varepsilon/\partial k_y)$. (b) Equivalence between normal and tangent vectors for the 1D FS: one transforms to another by rotating 90°. (3) Normal vectors distribution on the 2D FS can be similarly replaced by the distribution of tangent plane, a.k.a. tangent bundle.	41
4.1	Action of the U(1) gauge on complex space. The complex plane is represented as a sphere, by identifying poles on the sphere with zero and infinity on the complex plane. A point on the sphere represents value of the wavefunction $\psi(x)$. Multiplication by a complex number $ a =1$ rotates the sphere and thus the point ψ moves along a circle parallel to equator of the sphere.	44

List of Figures

4.2	Action of the U(2) gauge on the complex space. The two components of spinfull band (ψ_{up}, ψ_{down}) are the points on two spheres. Then if each sphere rotates, the total parameter space of angles of rotation is a torus.	45
4.3	Gauge connection on the banstructure. Disconnection between momentum is resolved due to geometrical phase represented as segment on the circle on the right.	46
4.4	Gauge action on the reciprocal space.	47
4.5	Connectivity of bands. Different colors of the bands represent different EBR corresponding to the atomic positions schematically shown in the same color. The difference between different topological materials is in the amount and location of the one EBR group of bands at the Fermi level.	50
4.6	Spin and anomalous Hall effects. The applied voltage V_{in} results into spin accumulation on the sides of the sample for SHE or into perpendicular volatage V_{Hall}	52
5.1	Symmorphic and nonsymmorphic symmetry.	58
5.2	Bandstructure folding mechanism for non-symmorphic symmetry.	59
5.3	Schematic of the "Failed TI" bandstructure for the spin Hall purposes.	62
5.4	Crystal structure (a) and Brillouin zone(BZ) (b) for W_3W and A15 family (SG 223).	63
5.5	Electronic structures of W_3W without (a) and with(b) SOC, respectively. Dirac crossings are visible (without SOC) along the Γ -X-M lines, both at and below the E_F . Panel (c): spin Hall conductivity versus energy plot of W_3W	64
5.6	spin Berry curvature distribution in the the 001 and 110 planes of the BZ of W_3W where red and blue areas represent positive and negative regions.	65
5.7	Panel a) The electronic structure of W_3W near the Dirac crossings decomposed into the various orbital and crystallographic site ($2a$ and $6c$) contributions. Thickness of the bands indicates the extent of the orbital or orbital group contribution to a band. By symmetry, the $2a$ site's orbitals group into the t_{2g} and e_g sets. The $6c$ site has lower degeneracy. The d_{xy} is not shown as it does contribute to the relevant bands. Panel b,c) The electronic structures with SOC included, illustrating the orbital hybridization driven by SOC, opening gaps and generating spin Berry curvature.	66

List of Figures

5.8	Panel a,b,c) Electronic structure of Ta ₃ Sb without and with SOC as well as its SHC versus energy plot. Ta ₃ Sb's has a peak in its SHC at its E _F . Panel d) Zoomed in band structure highlighting the 8-fold degeneracy near the E _F . Panel d) Topological protected surface states (projected to the 001 face) in Ta ₃ Sb connecting the conduction and valence bands along X-Γ-M.	67
5.9	Bandstructures and SHC of (a) W ₃ Si (b) Ta ₃ Sn (c) Cr ₃ Os (d) Ta ₃ Os. The red line is without SOC and the black line is with.	68
5.10	Adjustment of the Fermi level in the squar nets compounds CeBiTe	69
5.11	Electronic structures of Ta ₃ Ta, W ₃ Re and W ₃ Ta, without and with SOC included, as well as their spin Hall conductivity versus energy plots.	70
6.1	Connection of a Dirac point to a irregular Fermi surface orbit.	75
6.2	Relation between local and global Fermi surface paths.	77
6.3	(a) Schematic representation of a typical Fermi surface where the green plane (T _K E _F) represents the tangent plane at point K on the Fermi surface and v _F is the group velocity. (b) A locally elliptic cut of a Fermi surface with tangent plane and velocity vectors drawn as green arrows. (c) A locally Euclidean cut and (d) A locally hyperbolic cut. E. Illustration of anomalous Hall (AHE) and spin Hall (SHE) measurement geometries.	78
6.4	Deformation of singularity for a hyperbolic point on the Fermi surface.	81
6.5	Schematic distribution of the hyperbolic and non-hyperbolic regions of the Fermi surface in the reciprocal unit cell for the AHE compounds of varying magnitude.	82
6.6	Schematic distribution of the hyperbolic and non-hyperbolic regions of the Fermi surface in the reciprocal unit cell for the SHE compounds of varying magnitude.	83
6.7	Definition of the vector F _{Hall} as a projection of unit vector from the FS tangent plane.	84
6.8	Correlation graph left: <i>experimentally</i> determined intrinsic AHC vs \mathbb{H}_F for various materials ((l) identifies layered structures). Right: <i>experimentally</i> determined intrinsic AHC vs predicted values of AHC via the Kubo formalism.	85
6.9	Correlation graph of the predicted SHC values via the Kubo formalism vs \mathbb{H}_F , as defined in the text.	86

List of Figures

6.10 (a) Bandstructure of $CrPt_3$. Blue and yellow colors represent two topologically disconnected (having different EBRs) sets of bands crossing the Fermi level. These sets are disconnected by the continuous gap present between them; i.e. true semimetallic behavior. (b) Graph of energy resolved AHC predicted in two different ways: red dashed line is the Kubo based prediction, black dashed line stems from the linear correlation between H_F and AHC calculated separately for FS contributions from each set of bands, then summed together for total \mathbb{H}_F	87
7.1 Schematic representation of topology on the Hamiltonian's domain and spectrum of the corresponding Hamiltonian.	92
7.2 Relation between the structure of Hamiltonian's domain and the spectrum of Hamiltonian (a.k.a. bandstructure) and $\Phi_{crystal}$ for Bloch bands and EBR. . . .	93
7.3 Construction of an atlas of maps f_i on the bandstructure (for 1D bandstructure).	94
7.4 Diagram of the classes of local geometries in different dimensions. The left column shows the 8 Thurston geometries for 3D manifolds, like band structures, presented schematically and with their symbols of geometry. The middle column shows the three smooth (and non-smooth) classes for 2D manifolds like Fermi surfaces. The right hand column shows the classifications of 1D paths, like Fermi surface paths, resulting from further reduction of dimension. Arrows illustrate the connection between certain higher dimension geometrical classes and their lower dimensional counterparts; green arrows showcase how hyperbolic 2D manifolds can result in all types of 1D paths.	95
7.5 Visual analogy between curved by mass real space and curved by the crystal potential momentum space.	96
7.6 Electronic structure without and with SOC included as well as the SHC vs energy plot for Nb_3Os	101
7.7 Electronic structure without and with SOC included as well as the SHC vs energy plot for Nb_3Al	102
7.8 Electronic structure without and with SOC included as well as the SHC vs energy plot for Nb_3Au	103
7.9 Electronic structure without and with SOC included as well as the SHC vs energy plot for Nb_3Bi	104

List of Figures

7.10	Electronic structure without and with SOC included as well as the SHC vs energy plot for Ta ₃ Au	105
7.11	Electronic structure without and with SOC included as well as the SHC vs energy plot for Ta ₃ Ir	106
7.12	Electronic structure without and with SOC included as well as the SHC vs energy plot for Cr ₃ Ir	107
7.13	Electronic structure without and with SOC included as well as the SHC vs energy plot for Ti ₃ Ir	108
7.14	Electronic structure without and with SOC included as well as the SHC vs energy plot for Ti ₃ Pt	109
7.15	Electronic structure without and with SOC included as well as the SHC vs energy plot for V ₃ Pt	110
7.16	Schematic plot of negatively and positively contributing bands to the \mathbb{H}_F . The red circle highlights the band habit at the BZB (Brillouin zone boundary) where the sign of the curvature (second derivative of the band) is used for identification of the contribution type. A consistent choice of BZB is used for analysis of all bands.	111
7.17	\mathbb{H}_F dependence of k-mesh density for Fe and Co ₂ FeSi. y-axis is the calculated total \mathbb{H}_F , and the x-axis is k-points cubed.	111

Introduction

While the mathematical concept of topology originally arose as a purely theoretical discipline, topological physics exploded onto the scene after the experimental realization of Topological Insulators (TI) [1, 2, 3] in 2007. This opened the door for mathematics, mixed with material science, to become an important fundamental and technological topic for researching novel physical phenomena, as well as technologically relevant properties [2, 4, 5]. The idea of using topological invariants for the classifications of an Hamiltonian's eigenstates in crystalline solids, i.e. electronic bands in energy-momentum space (E vs k), has been used to successfully predict protected electronic states and properties including the quantum Hall effect [6, 7]. There have also been attempts to use topology to characterize other types of experimentally observed transport phenomena (e.g. the non-quantized anomalous Hall effect (AHE), spin Hall effect (SHE), skyrmion/domain wall dynamics and superconductivity) based on the non-quantized properties of a gauge generated field on the electronic band, which is known as the Berry phase [8]. However, for the prediction of quantum transport effects mostly only a curl of the Berry phase, a.k.a. the Berry curvature, is used. This Berry curvature based approach works relatively well for predicting the intrinsic AHE and SHE (where carriers acquire a velocity component orthogonal to an applied electric field without an externally applied magnetic field), but has had accuracy issues with compounds like Ni [9]. The topological theories of electronic band structures for strongly correlated phenomena, like superconductivity and charge density wave formation, however, are not as successfully used as macro models such as the Ginzburg-Landau and the Mott-Hubbard theories [10, 11].

Topology, as a branch of mathematics, studies possible ways to introduce continuity into the space of abstract objects like wavefunctions. This allows the use of methods of classical differential calculus for the Hamiltonian, considering it simply as a function acting on numbers (e.g. crystal momentum indexing the wavefunction), rather than on the wavefunctions. In order to do this the space of the wavefunctions is considered as a manifold. The "shape" of this manifold, resulting in connectivity between the wavefunctions, results in non-trivial properties of the Hamiltonian. The connected bands of eigenfunctions of the Hamiltonian can be grouped into the set of bands according to its elementary band representation (EBR), for which the simplified consideration of the Hamiltonian, acting as a function on numbers is applicable, and thus the semiclassical approximation with the Berry curvature correction is valid, as it was recently presented in the work on topological quantum chemistry [12]. The study of the eigenstates' connectivity and their topological properties by introducing indexes and geometrical phases, like the Berry phase, however, doesn't allow full implementation of methods of topology into quantum

Introduction

transport theories. The currently used approach works well for classification, in the way it was done in the topological quantum chemistry database, but fundamentally it doesn't change the semiclassical transport formalism. So far, quantum transport theories of, for example, AHE are based on Green's functions for calculation of two bands transition to estimate Berry phase-related properties [8].

In this work, the limits of this approach will be discussed and an alternative approach, based on the geometrical properties of the Fermi surfaces of topological semimetals, will be proposed. The Fermi surface, as well known, governs transport properties of metals, but for semimetals, where the Fermi surface consists of both electron and hole pockets, the theory works only on the assumption, that pockets don't intersect with each other. Otherwise, the intersection leads to a so-called magnetic breakdown, at the intersection of the corresponding Fermi surface orbits and it results in quantum tunneling. The point of the intersection corresponds to an intersection of the bands, known as a Dirac or a Weyl point and its effect on transport can be described in terms of the Berry curvature. However, as will be discussed in this work, the intersection in the Fermi surface orbits can happen within one band pocket, without an intersection of different bands, which can also lead to quantum transport effects. The properties of the Fermi surface orbits as being self-intersecting, independently of how many bands they have been formed by, can be traced using the tangent planes distribution on the Fermi surface. This allows for the possibility of making a local classification of the Fermi surface in the geometrical types corresponding to the different orbit properties. Then, capturing the degeneracies in the Fermi surface orbits should be a more accurate estimation of quantum transport effects, with respect to the Berry curvature formalism, capturing pairwise intersections of bands due to the topological connectivity. The comparison of the Berry curvature based approach and the local Fermi surface geometry approach will be shown with the example of the AHE and SHE. The local geometry concept can then be extended and used similarly to the bandstructure, which leads to the complete classification of not just metals, having the Fermi surface, but also insulators and semiconductors. This classification is known as the parametrization conjecture, whose proof famously resulted in the solution of one of the millennium problems. The possibility to use this mathematical theory for bandstructures as 3D manifolds, will also be briefly discussed as an application of geometrical methods.

The results, presented in this work, are based on an interplay between semiclassical quantum transport theory for electrons in a periodic potential and the framework of topology and differential geometry. The basic concepts from quantum material science will be recalled in the

first chapter. The goal of this chapter is to introduce the notation and classification of semimetals and their degeneracies in the bandstructure as a common language used in topological quantum physics. In the second chapter, computational methods of quantum material science will be presented starting with DFT calculations for the electronic eigenstates. Then, a semiclassical approach to quantum transport will be considered, focusing on different foundations to introduce the continuous connection between the eigenstates (e.g. non-equilibrium temperature effect or quasiparticles formation), which naturally brings up a discussion of the Green functions as a possible mathematical tool to handle it. Continuity of disconnected objects is a main subject of topology and will be introduced in chapter three. It gives a mathematical formalism to build differential calculus needed for semiclassical transport using the construction of a tangent bundle on a manifold. When the electronic eigenstates in the crystal are treated as a manifold, their study can be carried out using special quantities, such as the Berry phase, the Berry curvature, Chern numbers etc., which will be discussed in the fourth chapter. These quantities have been used to analyze the connectivity of the eigenstates, however a direct full derivation of an alternative to the semiclassical approach to the electron transport, based on calculus on the eigenstates' manifold, using the tangent bundle, hasn't been done yet. Instead, the semiclassical transport equation was modified by the additional Berry curvature term, which leads to the possibility to calculate AHC and SHC, using Green's function, which is known as the Kubo formalism.

The fifth chapter discusses the use of geometrical features in the bandstructures to predict transport properties. First, as an example, the SHC the A15 family of superconductors calculated from the Berry curvature based formalism, will be related to the geometrical flag feature in the semimetallic bandstructure: the gapped anti-crossings. These geometrical features are related to the crystallographic symmetries and thus can be analyzed algorithmically on the databases. However, calculations of SHC are still needed, since location of the flag feature with respect to the Fermi level is significant for the total SHC. The Berry curvature based calculations cannot be carried out automatically, therefore the flag feature based symmetry analysis is just a preliminary step in the SHE materials search. On the other hand, this geometrical feature is related to the shape of the FS, as will be shown in chapter six, however, it's not a one-to-one correspondence. The shape of the Fermi surface around a point, i.e. the Fermi surface local geometry, can be studied using the tangent planes, and classified into three types: elliptic, hyperbolic and Euclidean. The hyperbolic case is related to the SHE and AHE and it shows a striking correlation with the 15 experimentally observed AHE compounds. The \mathbb{H}_F index will be introduced as a

Introduction

numerical quantifier of hyperbolicity of the FS and based on the \mathbb{H}_F predictions will be compared with the experimentally obtained values of AHC as well as with numerical predictions of AHC and SHC based on the Berry curvature. In the seventh chapter, the idea to use tangent bundle for transport properties analysis will be extended to the whole bandstructure.

Chapter 1

Electronic eigenstates in semimetals

Bandstructure or electronic structure is one of the most powerful tools to analyze quantum transport in crystalline solids. Such a way to represent eigenvalues of a many-body crystalline Hamiltonian as "pseudofunctions" will be the main focus of this chapter. The chapter will introduce the consistent notation of the electronic structure properties (like anti-crossing, Weyl/Dirac points etc.) for semimetallic crystalline solids, that will be used later in this work.

The formal construction of the bandstructure and definitions related to the quantum transport, including a construction of the Fermi surface, will be recalled in the first section. Particularly, the discussion on the dimensionality of the crystals and the corresponding bandstructure's properties will be elaborated. In the second section, the effect of the electrons' spin on the bandstructure and time reversal symmetry will be discussed. In the third section degeneracies in the bandstructure will be introduced and classified for different dimensionalities of the bandstructures. In the end, there will be an illustration of a connection between degeneracies in the bandstructure and the Fermi surface degeneracies. Details and ramifications of this connection are the main subject of this work and will be discussed in the later chapters.

1.1 Bandstructure

The dynamics of an electron with the wavefunction $\psi(x)$ is defined by the time-dependent Schrödinger equation:

$$i\hbar \frac{d\psi(x,t)}{dt} = H\psi(x,t), \quad (1.1)$$

where H is the Hamiltonian and consists of all possible physical interactions (ideally) that the particle can be involved in. The wavefunction can be determined by solving this equation. If ε is an eigenvalue of the Hamiltonian, then the solution of the equation (1.1) is the following

$$\psi(t, x) = e^{-\frac{i}{\hbar} \int_0^t dt' \varepsilon(t')} \psi(0, x). \quad (1.2)$$

For a free electron, H consists only of the kinetic energy term $-\frac{\hbar^2}{2m} \nabla^2$. If the electron is moving in a crystal, an external periodic potential V , formed by the average potential of all of the other electrons and nuclei on the lattice, must be included, i.e.

$$H = -\frac{\hbar^2}{2m} \nabla^2 + V. \quad (1.3)$$

In this case, due to Bloch theorem [13] the eigenfunctions of the Hamiltonian can be written as,

$$\psi(0, x) = \varphi_k(x) = e^{ikx} u_k(x), \quad u_k(x + R) = u_k(x). \quad (1.4)$$

The parameter k represents the crystal momentum and is associated with an electron in the lattice.

If the lattice consists of N atoms and every atom has n electrons, and the eigenvalue problem is solving for every electron in the lattice, then the equation 1.1 transforms to the system of Nn , or equivalently an equation with a $Nn \times Nn$ Hamiltonian matrix, linearized, as the following

$$H = \begin{pmatrix} \varepsilon_1(k_1) & 0 & \dots & 0 \\ 0 & \varepsilon_1(k_2) & \dots & 0 \\ \dots & & & \\ 0 & \dots & \varepsilon_2(k_1) \dots & 0 \\ \dots & & & \\ 0 & 0 & \dots & \varepsilon_n(k_N) \end{pmatrix} \quad (1.5)$$

applied to the many-electron wavevector $\phi^T = (\varphi_1^{k_1}(x), \dots, \varphi_{Nn}(x))$ instead of a one-electron wavefunction. Then the space $\Phi^{crystal}$ can be introduced

$$\Phi^{crystal} = span(\varphi_1(x), \dots, \varphi_{Nn}(x)) \quad (1.6)$$

as the domain of the total Hamiltonian.

Working with such high dimensional objects is not convenient. Therefore, the wavefunctions are categorized into bands $\{\varphi_i(k)\}_{k=1..N}$ according to the local symmetry of the wavefunction, which is described by the orbital momentum quantum number. After Fourier transformation, ψ_i becomes a function represented in a new basis of functions, depending on crystal momentum (schematically it is shown in figure 1.1 (a)).

Definition 1. *All together $\{\varepsilon_i(k)\}_{i=1..n}$, considered as functions of momentum k , comprise the electronic structure of the material, a.k.a. bandstructure.*

The bandstructure is a convenient representation of the total lattice Hamiltonian, compared with matrix notation. The band in reciprocal space, however, is not really a function; it consists of discrete points and is neither smooth nor continuous as it is shown in figure 1.1 (b). However, this band structure contains the information about the original function $\psi(x)$: if the momentum is fixed in the value k_0 , the function $\varphi_i(k_0)$ is an eigenfunction of the localized Hamiltonian in form 1.4 known as a Bloch wavefunction for the corresponding eigenvalue $\varepsilon_i(k)$ 1.1

Overall energies in the bandstructure there is a special value known as the Fermi level. It is a hypothetical energy level of an electron in given crystal potential, such that at thermodynamic equilibrium this energy level would have a 50 % probability of being occupied at any given time. The location of bands with respect to the Fermi level dictates the transport properties of the compound. All the parts of the bandstructure laying above the Fermi level are referred to, as the *conduction bands* and laying below as the *valence bands*, and electrons and holes as are the carrier types respectively. If the Fermi level crosses a band then the compound is metallic. If the Fermi level does not cross any band, then then compound is either semiconductor or insulator.

Definition 2. *All the momentum k in the bandstructure, where the Fermi level crosses any band, comprise the Fermi surface.*

However in the case of 1D bandstructure it's not a truly surface, but just few points (schematically shown in figure 1.2 (a)). A 1-D bandstructure can be thought of as the cross-section of a higher dimensional picture. In the 2D case the Fermi surface is a line (green ring in figure 1.2 (b)) and in the 3D case the Fermi surface can be thought as a surface and plotted already in momentum rather than energy-momentum space (like in figure 1.2 (c)). This surface separates momentum space into two zones: Fermi sea, which is a volume enclosed by the Fermi

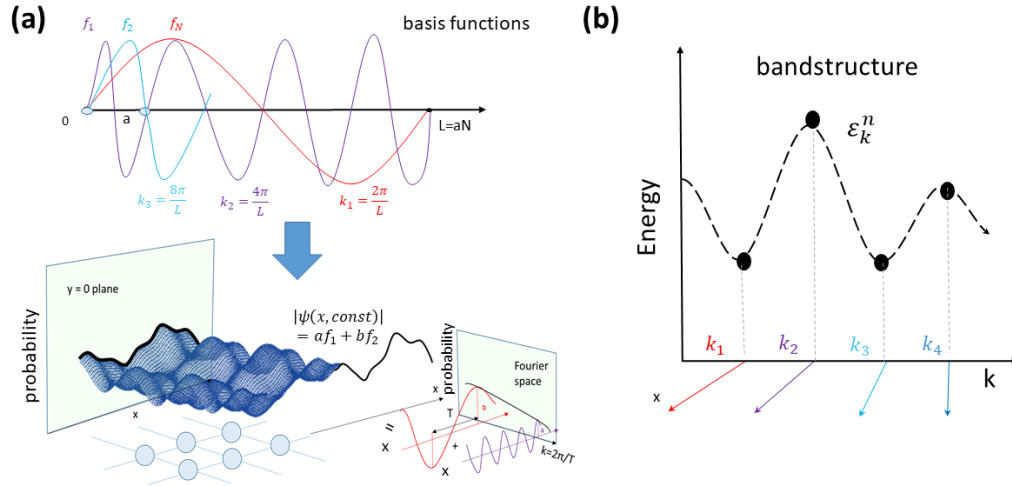


Figure 1.1: Representation of a function in the Fourier space. (a) Duality between momentum coordinates k and spatial coordinates x : at every fixed x a value of the wavefunction $\psi(x)$ can be expressed as a sum of the basic functions (harmonics), depending on k and drawn in the top panel in different colors. (b) Distribution of the Hamiltonian's eigenvalues in the momentum space. The vertical colored lines represents the hidden x axis for the different harmonics shown in (a).

surface, where the electrons affected by the crystal potential V are tied to the ion cores and its complimentary, where electrons behave like a free electron gas.

Definition 3. *If the Fermi surface consists of sheets from both the conduction and the valence bands then the compound is referred to as a semi-metal, and the sheets are called electron and hole pockets correspondingly.*

For semimetals, due to the presence of both types of pockets, the Fermi sea can have a non-trivial structure. This is illustrated on an example in figure 1.2 (c). For the electron pocket the Fermi sea is located outside of the Fermi surface (the right green "sphere" in the figure), but for the hole pocket (the left green "sphere" in the figure), the Fermi sea is inside. Thus, at the point where these two pockets are connected to each other, the Fermi sea should make a twist to get from the outside to inside. This twist relates to the topological connection between eigenstates,

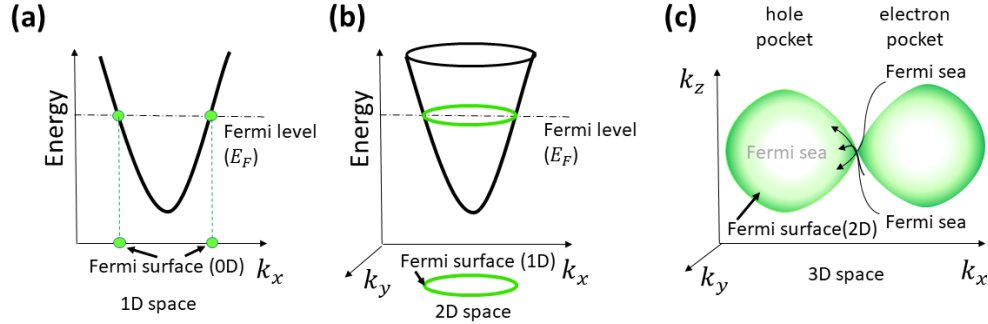


Figure 1.2: Dimensionality of the momentum space and corresponding FS. (a) 1D momentum space shown as a horizontal line demands 0D FS, shown as green points. (b) 2D momentum space shown as a horizontal plane demands 1D FS, shown as green circle. (c) 3D momentum space demands the FS to be a 2D surface, which is a boundary of the Fermi sea formed by occupied states. Two components of the Fermi surface represents electron pocket, where the Fermi sea remains outside of the pocket, and hole pocket, where the Fermi sea is inside. Thus, to smoothly pass from outside to inside through the FS, the Fermi sea makes a particular geometrical feature at the passing point on the FS.

that will be discussed in detail during chapter 4, which results in non-trivial transport properties of the compound. As one can see from the example in figure1.2 (c), the twist of the Fermi sea affects the shape of the Fermi surface locally around the point of the twist, and therefore the connection between two green spheres in figure1.2 (c) would be spiky, if it was a continuous surface. Study of the connection between such local geometrical properties of the Fermi surface and transport effects will be the main focus of this work.

1.2 Spin-orbit coupling

In the simple case, relativistic motion of the electrons is not taken into account in the equation 1.1. However, as the number of protons in the ion cores increases, the electrons can move with a speed that is close to the speed of light. For these cases, the Hamiltonian H can be modified in the following way:

$$H^{Dirac} = c\alpha\frac{\hbar^2}{2m}\nabla^2 + \beta mc^2 + V, \quad (1.7)$$

where V is the potential, α and β are the following matrices

$$\beta = \begin{pmatrix} I & 0 \\ 0 & -I \end{pmatrix}, \alpha^i = \begin{pmatrix} 0 & \sigma^i \\ \sigma^i & 0 \end{pmatrix}, \quad (1.8)$$

where σ are the Pauli matrices:

$$\sigma_x = \begin{pmatrix} 0 & 1 \\ 1 & 0 \end{pmatrix}, \sigma_y = \begin{pmatrix} 0 & -i \\ i & 0 \end{pmatrix}, \sigma_z = \begin{pmatrix} 1 & 0 \\ 0 & -1 \end{pmatrix}. \quad (1.9)$$

The Pauli matrices together with $I_{2 \times 2}$ form a basis for the real vector space of 2×2 Hermitian matrices. σ can be considered as an additional variable for $\psi = \psi(x, \sigma)$. For a $\frac{1}{2}$ spin particle, the Pauli matrices σ are related to the spin operator in the following way:

$$S = \frac{1}{2}\sigma. \quad (1.10)$$

The two-component wavefunction $\psi(x) = \begin{pmatrix} \psi_1(x) \\ \psi_2(x) \end{pmatrix}$ in this case can be interpreted as $\psi = \begin{pmatrix} \psi_1 = \psi(x, \frac{1}{2}) \\ \psi_2 = \psi(x, -\frac{1}{2}) \end{pmatrix}$. One of the components can be turned to zero by the choice of coordinate system (assume then it's ψ_2). Then the equation 1.7 implies:

$$\left(\frac{p^2}{2m} + V - \frac{p^4}{8m^3c^2} + \frac{\hbar}{4im^2c^2}(\nabla V \cdot p) + \frac{\hbar}{4m^2c^2}(\nabla V \times p) \cdot \sigma\right)\psi_1 = (E - mc^2)\psi_1, \quad (1.11)$$

where $p = \hbar\nabla$ is the momentum operator. The third term gives first order relativistic correction and can be neglected[14]. The fourth terms give a small correction to the energy of states, whose eigenfunctions are non-zero at singularities of V . It has the same symmetry properties as V and does not change the form of the Hamiltonian and can therefore be neglected [14]. Then then the remaining equation is known as the Schrodinger form of Dirac equation :

$$\left(\frac{p^2}{2m} + V + \frac{\hbar}{4m^2c^2}(\nabla V \times p) \cdot \sigma\right)\psi_1 = E_k\psi_1. \quad (1.12)$$

The additional term here includes momentum of the electron together with its spin represented by the Pauli matrices σ and therefore it's known as spin-orbit coupling (SOC).

The spin in the system is closely related to time reversal symmetry, i.e. invariance of the equation 1.1 with respect to the transformation $t \rightarrow -t$. According to Kramer's theorem [15], in the presence of time reversal symmetry (i.e. without magnetic field), both components $\psi_1(x), \psi_2(x)$ of a spin $\frac{1}{2}$ wavefunction corresponds the same energy eigenvalue ε . The eigenstates and corresponding bands in this case are called degenerate. In the absence of time reversal symmetry, the SOC term in the Hamiltonian makes the band corresponding to the eigenstates $\psi(k)$ split.

The breaking of time reversal symmetry and splitting of the bands can happen not only due to SOC, but for other physical phenomena in the system related to the spin degree of freedom, like ferromagnetic or antiferromagnetic spin splitting. When the wavefunction for every electron on the lattice is assumed to have two components, then the corresponding bandstructure is called spinful.

1.3 Semimetal classification

SOC is not the only addition to the potential V , that can be included in Hamiltonian. Other terms will be discussed later in chapter 3. For now, let's consider a general form of the Hamiltonian:

$$H = -\frac{\hbar^2}{2m}\nabla^2 + (\text{terms representing interactions}). \quad (1.13)$$

It is reasonable to assume that eigenstates of the electrons in the lattice do not differ strongly from the eigenstates of the free electron Hamiltonian $-\frac{\hbar^2}{2}\nabla^2$ which are known as the s, p, d,

f, etc orbitals. Thus we can represent the full lattice Hamiltonian as linear combinations of atomic orbitals (LCAO) according to the space group symmetry, which is the basic logic of molecular orbital theory [16]. If the space group for instance is nonsymmorphic then there is also translation by a fraction of a lattice vector that generates additional eigenstates which, in combination with other symmetries, giving rise to degeneracies in the bandstructure, i.e. such points where $\varepsilon_n(k) = \varepsilon_m(k)$. These degeneracies in the bandstructure are schematically shown in the figure 1.3. A similar situation may happen due to other symmetries like rotation, inversion, or mirror. Note that every point in the spinless band is always doubly degenerate due to Kramer's theorem. For now this degeneracy won't be taken into account and the degeneracies are discussed in the context of intersections of two bands with different symmetry characters. The presence of such degeneracy at the Fermi level is a signature that the Fermi surface has both valence and conduction components and thus the compound is a semimetal.

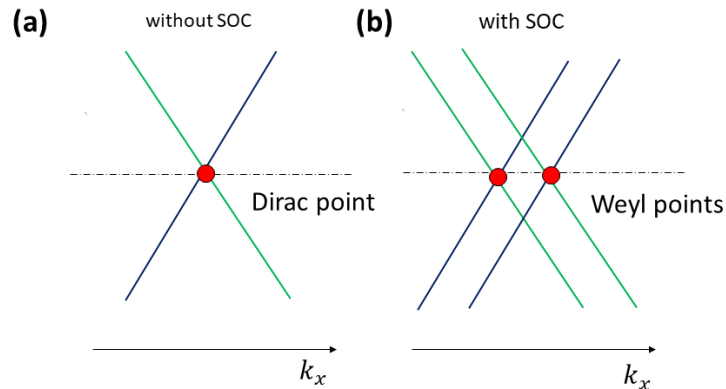


Figure 1.3: Degeneracies in the bandstructure of topological semimetals in one dimensional case. The Dirac point type of degeneracy shown on the left is made off two double degenerate (with Kramer's degeneracy) bands crossing each other, whereas the Weyl point shown on the left is made off non degenerate bands, e.g. spin-split by turning on SOC.

Definition 4. *If the degenerate point in the bandstructure is made of an intersection of dou-*

bly degenerate bands, then it's called a Dirac point and the corresponding compound is called Dirac semimetal (DSM). If additional SOC removes the degeneracy the degenerate point can be also called a Dirac anti-crossing or just anti-crossing. If the degenerate point is made of non-degenerate, in Kramer's sense, bands, it's called a Weyl point and the corresponding compound is called Weyl semimetal (WSM). This is schematically shown in figure 1.3 .

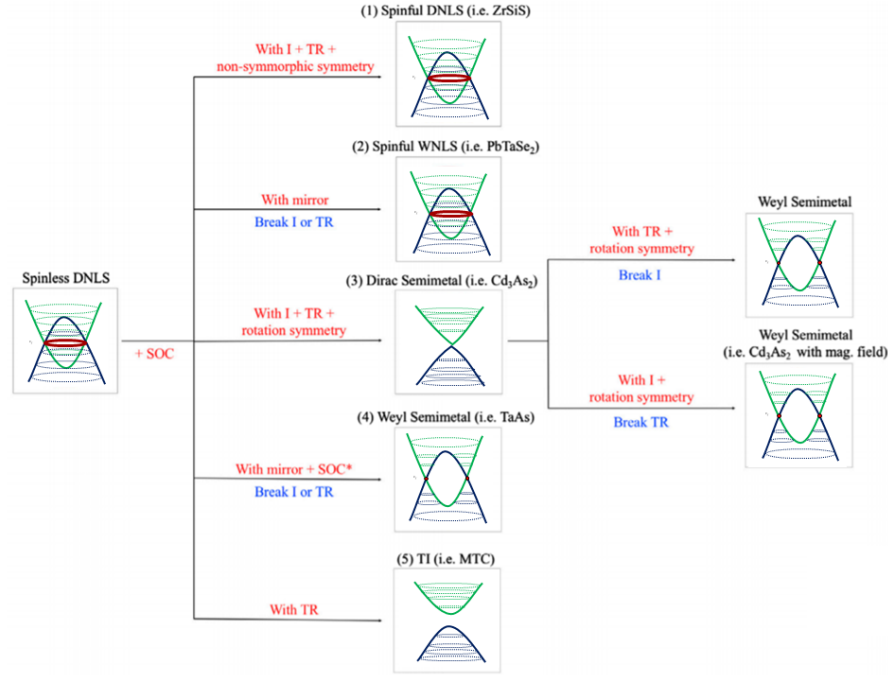


Figure 1.4: Classification of topological semimetals in two dimensional case.

The degenerate point can remain a point in higher dimensions, but may also be a line or even surface in a 3-D space. In this case, the compound will be called Dirac nodal line semimetal(DNLS) or Weyl nodal line semimetal(DNLS), depending on the symmetry of the system. Finer detailed classification [17] for 2D semimetallic bandstructures is given in figure 1.4. The DNLS can be considered as a starting point for realizing many other topological states. Starting from a spinless DNLS, SOC may lift the degeneracy along the crossing line, leading to [17]

1. a spinful DNLS when the line of degeneracy is protected by a combination of time-reversal, inversion, and nonsymmorphic symmetry (e.g. $ZrSiS$);

2. a spinful WNLS (e.g. $PbTaSe_2$) when mirror reflection within high-symmetry plane protects the nodal lines, but broken inversion symmetry (or broken time-reversal symmetry) splits the spin component at the nodal line, giving rise to two Weyl lines;
3. a 3D DSM (e.g. Cd_3As_2) if, for example, certain symmetry-invariant points are protected by rotation symmetry as well;
4. a WSM (e.g. $TaAs$) when, for example, the system has mirror reflection symmetry, orthogonal orbital component making up the electronic states, and proper strength of SOC;
5. a TI (e.g. Mackay-Terrones crystal) if, for example, the material has only inversion and time-reversal symmetry. This would give rise to a gapped bulk state but linearly dispersed projected surface states.

Starting from DSMs, breaking either inversion or time-reversal symmetry will lead to WSMs. The symmetry of a crystal structure and the atomic orbitals making up the electronic states at band crossings determine which topological state is realized under consideration of SOC: the electronic states must be orthogonal to each other in order to not get hybridized with each other and open a gap.

While for the 2D case we can still plot a 2D bandstructure and distinguish degenerate points from a line just visually, in 3D it becomes quite complicated. The typical procedure is to project full 3D bandstructure on various surfaces and analyze the series of projections. Another way to analyze a 3D case is to consider constant energy isosurfaces and particularly isosurface at the Fermi level, i.e. the Fermi surface. All the information about bandstructure in the energy range $(E_F - \delta, E_F + \delta)$ is kept in the Fermi surface. Thus a point in the 1D bandstructure, if it remains a point in the 2D bandstructure, can be either a degenerate point on the Fermi surface or a degenerate line on the surface. If a nodal line appeared in the 2D bandstructure, it can remain a degenerate line on the Fermi surface or even become a full degenerate Fermi surface sheet. All these possible degeneracies at the Fermi surface can be distinguished into two types: isolated and irregular. Schematically this is shown in figure 1.5.

Definition 5. *A degenerate point belonging to a bulk Fermi surface sheet of dimensionality less than 3 will be referred as isolated. A degenerate point belonging a three dimensional Fermi surface sheet will be referred as irregular.*

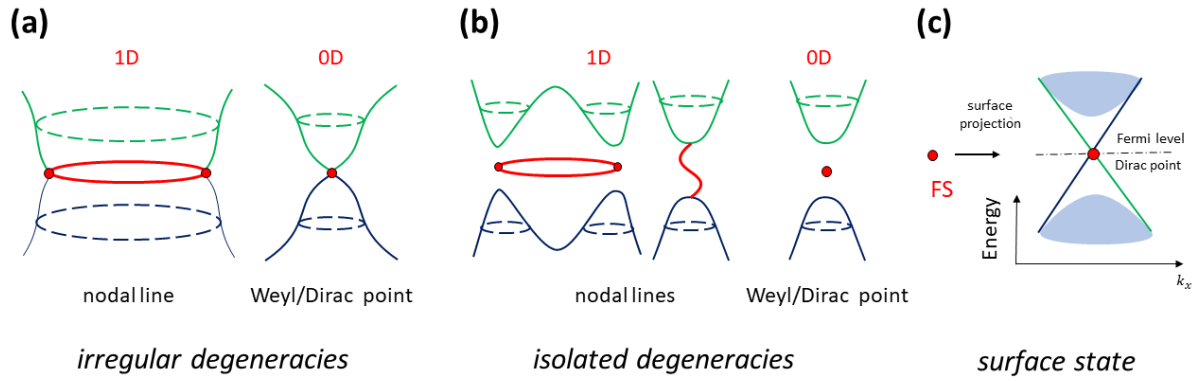


Figure 1.5: Degeneracy in three dimensional case appearing on the Fermi surface. The red color represents degenerate points, blue points from the valence band, green points from the conduction band.

The different types of degeneracies in the bandstructure and their effect on the Fermi surface result into non-trivial transport properties of the electrons in the corresponding crystal potential. Examples of the FS degeneracies in real semimetallic compounds [18, 19] are shown in figure 1.6.

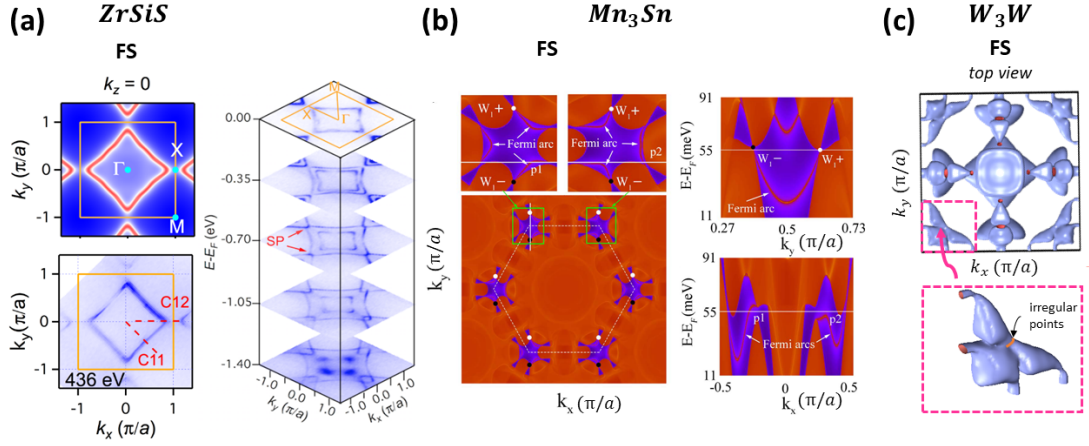


Figure 1.6: Degeneracies on the Fermi surface for $ZrSiS$, Mn_3Sn , W_3W . (a) Isolated degeneracies in $ZrSiS$ FS. Calculated FS slice is top left, measured FS slice is bottom left. At the right side the measured bulk bandstructure confirming isolated type of degeneracy: the bulk bandstructure remains 2D up to -1.4 eV and thus its slice at the Fermi level is 1D. (b) Isolated and irregular degeneracies in Mn_3Sn . The slice of the bandstructure is shown: the orange color represents filled states, purple not filled and red color between them represents FS. The irregular degeneracies are marked as WP (Weyl point) and isolated are marked as "Fermi arc". (c) Irregular degeneracies in W_3W .

Chapter 2

Computational transport theory

The following chapter is a review of numerical methods used to calculate bandstructures and predict transport properties of materials. The content of this chapter presents a theoretical base for the main results of this work.

In the first section, the formalism of density functional theory (DFT), used to perform all the bandstructure calculations in this work, will be introduced. In the following section, the semiclassical approach to electrons' transport will be shown. This approach gives a background to study geometrical properties of the Fermi surface in relation to quantum transport. In the final section of this chapter, a discussion on necessary for semiclassical calculation continuity of the eigenvalues within a band will begin with the Green functions as a method to introduce continuity of the bands.

2.1 Density functional theory

For the electrons in the crystal lattice the Hamiltonian H in the equation 1.1 can be split into the following parts:

$$H = T_N + T_e + V_{NN} + V_{ee} + V_{Ne}, \quad (2.1)$$

where T_N is the kinetic energy of nuclei, T_e is the kinetic energy of electrons, V_{NN} , V_{ee} , V_{Ne} represents nuclear-nuclear interactions, electron-electron interactions and electron-nuclear interactions, respectively. If the $\{\bar{x}_i\}$ electronic coordinates and the $\{\bar{R}_j\}$ are nuclear coordinates

plus m_i and M_i are masses of electrons and nuclei respectively, then the Hamiltonian can be written as following:

$$H = - \sum_i \frac{\hbar^2}{2M_i} \nabla_i^2 - \sum_i \frac{\hbar^2}{2m_i} \nabla_i^2 + \frac{e^2}{2} \sum_I \sum_{I \neq J} \frac{Z_I Z_J}{|R_I - R_J|} + \frac{e^2}{2} \sum_i \sum_{j \neq i} \frac{1}{|x_i - x_j|} - \frac{e^2}{2} \sum_I \sum_j \frac{Z_I}{|R_I - x_j|}. \quad (2.2)$$

To reduce dimensionality of the equation the Bohn-Oppenheimer (BO), approximation can be used to split the electron and nuclei coordinates:

$$H_{BO} \psi_R^{BO}(x) = E_{BO} \psi_R^{BO}(x). \quad (2.3)$$

So the total wavefunction $\psi(R, x) = \theta(R) \psi_R^{BO}(x)$ can be obtained by minimizing the BO potential $E_{BO}(R)$. Even in the BO approximation, the Schrodinger equation still requires massive calculations to be solved.

In density functional theory instead of using the wavefunction, the ground-state electron density can be used as the basic variable for the corresponding energy functional [20]:

$$E(n) = \int v(x)n(x)dx + \frac{1}{2} \int \int \frac{n(x)n(x')}{|x - x'|} dx dx' + G(n), \quad (2.4)$$

where $v(x)$ is the external potential from the nuclei and $G(n)$ is a universal function of the density.

It's been proved by Hohenberg and Kohn [21] that: there's one to one correspondence between the external potential and the electron density and the ground state energy and density in a given external potential can be simply determined by the minimization of a universal energy functional of density.

The universal function of the density $G(n)$ is not given in any particular form. For the practical computational issues, the energy functional can be separated as the sum of the kinetic energy of a non-interacting electron $T_s(n)$, the classical static Coulomb repulsion energy of the density, and the exchange and correlation (xc) energy of the interacting system $E_{xc}(n)$.

$$E(n) = \int v(x)n(x)dx + \frac{1}{2} \int \int \frac{n(x)n(x')}{|x - x'|} dx dx' + T_s(n) + E_{xc}(n). \quad (2.5)$$

The $E_{xc}(n)$ varies relatively slow and can be considered in the following simple form

$$E_{xc}(n) = \int n(x)\varepsilon_{xc}dx, \quad (2.6)$$

where ε_{xc} is the xc energy density for a uniform electron gas. Taking into account the stationary condition $\int \delta n(x) = 0$ the variation of the energy functional will take the following form, known as Kohn-Sham equation :

$$\left(-\frac{1}{2}\nabla^2 + (v(x) + \frac{1}{2} \int \frac{n(x')}{|x-x'|} dx' + u_{xc}(n(x)))\right)\psi_i(x) = \varepsilon_i\psi_i(x), \quad (2.7)$$

where $u_{xc} = \frac{d(n(x)\varepsilon_{xc})}{dn}$ is the xc potential of a uniform gas with density $n(x)$. For the system with N electron the density can be expressed as following:

$$n(x) = \sum_i^N |\psi_i(x)|^2. \quad (2.8)$$

Equation 2.7 can be used to find ε_i and obtain the bandstructure, however the xc potential doesn't have an exact explicit expression and needs to be approximated. In the limit of homogeneous electron gas with the xc energy density ε_{xc}^{hom} , the Local Density Approximation (LDA) can be used:

$$E_{xc}^{LDA}(n) = \int n(x)\varepsilon_{xc}^{hom} dx. \quad (2.9)$$

The exchange and correlation part can be considered separately. Then the spin degree of freedom can be taken into account considering the exchange part in the following form known as Local Spin Density Approximation(LSDA):

$$E_x^{LSDA}(n_{up}, n_{down}) = \sum_{\sigma=up,down} \int \varepsilon_x(n_\sigma)n_\sigma(x)dx, \quad (2.10)$$

where, the exchange energy density is the following:

$$\varepsilon_x(n_\sigma) = -\frac{3}{2}\left(\frac{3}{4\pi}\right)^{\frac{1}{3}}n_\sigma^{\frac{1}{3}}(x). \quad (2.11)$$

The correlation part in 2.9 can be calculated using Monte-Carlo methods. All of the electronic structure calculations used in this work later are done using DFT calculations with LDA(LSDA).

To generalize this method to magnetic systems, besides the knowledge of $n(x)$, the determination of another ground-state variable, namely the magnetization density $m(x)$.

Assuming that the external magnetic potential only couples to the spin degrees of freedom [22, 23], one has to regard in a non-relativistic theory a set of Kohn-Sham equation for two-component spinors $\psi = (\psi^{up}, \psi^{down})$, which have the form of Pauli equations. This treatment leads to an additional contribution of the external potential

$$V_{ext}(n, m) = \int (n(x)V_{ext}(x) - B(x)m(x))dx, \quad (2.12)$$

which is a functional of $n(x)$ and $m(x)$. The second term describes the coupling of a magnetic field to the electron spins,

$$\sum_n B_n m_n = \sum_i \langle \psi_i | \mu_0 B \sigma | \psi_i \rangle, \quad (2.13)$$

where $n = \{x, y, z\}$ represents the expectation values of the spin-operators. Since coupling is assumed to be exclusively between the external magnetic field and the electron spins orbital magnetism is not included within the spin-density-functional theory.

2.2 Semiclassical transport

When the bandstructure for a given crystal potential is obtained by any computational methods, the dynamics of an independent (with no interaction to other electrons) electron belonging to the n -th band traveling in the crystal potential (for a crystal with lattice constants a, b, c) in applied fields is described by the following equations [24]:

$$\hbar \frac{dk_a}{dt} = eE(x) + eH_{ab}(k) \frac{dx^b}{dt}, \quad (2.14)$$

$$\frac{dx^a}{dt} = \frac{1}{\hbar} \nabla_a \epsilon(k), \quad (2.15)$$

where $E(x)$ is an applied electric field, $H(x)$ is an applied magnetic field, and $\nabla_a = \frac{\partial}{\partial k_a}$. This equations approximate the dynamics only in relatively low fields, satisfying the conditions:

$$eEa \ll \frac{E_{gap}^2(k)}{E_F}, \quad (2.16)$$

$$\hbar\omega_c \ll \frac{E_{gap}^2(k)}{E_F}, \quad (2.17)$$

where $E_{gap}(k) = \min_m |\epsilon_n(k) - \epsilon_m(k)|$, a is the length on the order of the lattice constant and $\omega_c = \frac{eH}{mc}$ is known as angular cyclotron frequency.

It follows from the equation 2.14 that an applied magnetic field changes electron's momentum along the Fermi surface cross-section with the plane perpendicular to the direction of the applied field. This curve is known as cyclotron orbit or just orbit. Schematically all type of orbits are shown in the figure 2.1. The orbits, which cross the first BZ boundary, are called open, otherwise, they are called closed. For the closed orbits, the momentum really makes cycles (similar to the cosmological orbits) and stays within the first BZ. For open orbits, this is not the case. It can also happen that orbits are overlapping and this situation is known as a magnetic breakdown. At the point of breakdown a field-induced quantum tunneling happens. If the intersection is made off two different bands, then the point of breakdown is a Dirac or Weyl point [25]. Tunneling then can be described in terms of the Berry phase for the corresponding eigenstates, as will be explained in later chapters.

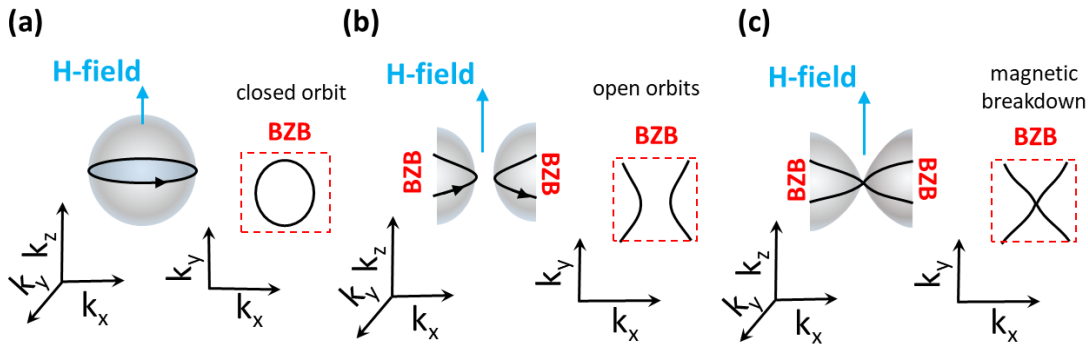


Figure 2.1: Orbits on the FS in the magnetic field. (a) Closed orbits. (b) Open orbits. (c) Magnetic breakdown, when the orbits intersect.

Similarly from the equation 2.14 it follows that in an electric field the electron's momentum changes within the band along the direction of the applied field. This is schematically shown in

the figure 2.2.

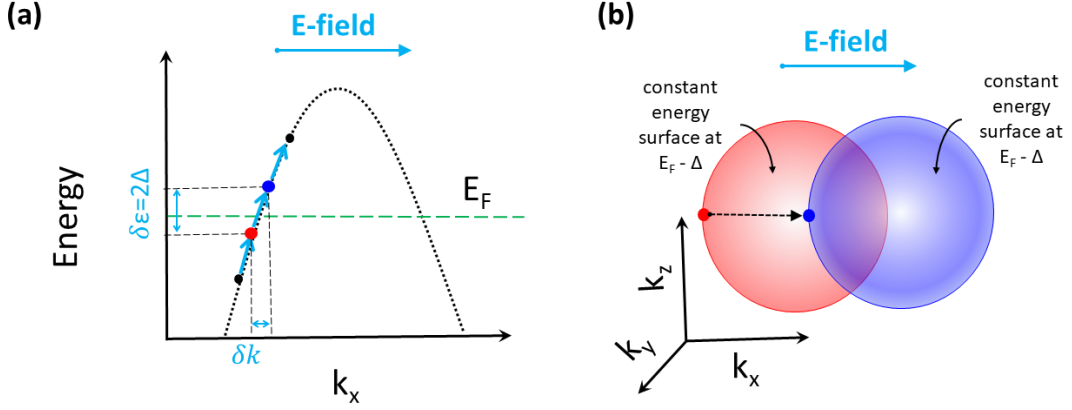


Figure 2.2: Dynamics in momentum space induced by the electric field. (a) change of momentum within a band along the field direction. (b) Transformation of the FS as a shift along the field direction.

This δk induced by the external fields results in the electron's motion with velocity according to the equation 2.15. The electrical current in the a -direction then can be found by averaging the velocity of the electron $v_n(k) = \frac{dx^a}{dt}$ in the following way:

$$j = (-e) \int_{occupied} \frac{dk}{4\pi^3} v_n(k). \quad (2.18)$$

However, the band consists of discrete disconnected eigenvalues $\epsilon_n(k)$ and formally the derivative $\nabla_a \epsilon(k)$ and thus velocity are not well defined. This can be resolved by the temperature effect and non-equilibrium function g of occupation of the eigenstates based on the Fermi distribution $f(\epsilon)$:

$$g_n(x, k, t) \equiv f(\epsilon_n(k)), \quad (2.19)$$

$$f(\epsilon(k)) = \frac{1}{e^{(\epsilon - \mu)/k_B T} + 1}.$$

where μ is the chemical potential, i.e. the Fermi level, corresponding to the equilibrium state. For a non-equilibrium state the relaxation time $\tau(x, k)$ for collisions between two electron leads to:

$$\begin{aligned} dg_n(x, k, t) &= \frac{dt}{\tau(x, k)} g_n^0(x, k), \\ g_n^0(x, k) &= \frac{1}{e^{\varepsilon_n(k) - \mu(x)/k_B T(x)} + 1}. \end{aligned} \quad (2.20)$$

In this case $\varepsilon(k)$ can be considered to be quasicontinuous and the expression of the electrical current transforms to:

$$j = (-e) \int_{BZ} \frac{dk}{4\pi^3} v_n(k) g. \quad (2.21)$$

Then since $j = \sigma E$ the conductivity σ can be expressed as the following:

$$\sigma = e^2 \tau(\varepsilon_F) \int_{BZ} \frac{dk}{4\pi^3 \hbar} v_n(k) f \varepsilon(k). \quad (2.22)$$

For the case of AC current, when $E(t) = \text{Re}(E(\omega e^{-i\omega t}))$, the conductivity expression transforms to the following:

$$\sigma_n(\omega) = e^2 \int_{BZ} \frac{dk}{4\pi^3 \hbar} \frac{v_n(k) v_n(k) (-\partial f / \partial \varepsilon)|_{\varepsilon=\varepsilon_n(k)}}{1/\tau_n(\varepsilon_n(k)) - i\omega}. \quad (2.23)$$

Assume E-field is applied in the x-direction, then only $v_x(k)$ component of the velocity $v_n(k)$ is non zero. Then the equation 2.22 can be represented also as the Fermi surface integral:

$$\sigma_x = e^2 \int_{FS} \frac{dk v_x^2(k)}{8\pi^3 \hbar} v_n(k) \tau(k) df(\varepsilon). \quad (2.24)$$

For the independent electron approximation $\partial^2 v_x(k) = m^*/\partial k$ called the effective mass. Thus the conduction depends only on relaxation time $\tau(\varepsilon_F)$ and velocity $v(\varepsilon_F)$ at the Fermi surface. The function $\varepsilon(k)$ should be quadratic and differentiable up to 2nd order.

Assumption of connection of the points in the bands is based on the finite temperature non-equilibrium effect and is not valid for the temperatures very close to the absolute zero. For

extremely low temperatures a similar approach can be used, but the continuity of the points in the band relies upon a non-equilibrium state due to interactions between electrons, i.e. the low temperature theory can be constructed without the non-interacting approximation. The above equations were derived for a single electron dynamics in the assumption it does not interact with other electrons within the relaxation time. However, the interaction between electrons can have a strong effect (like in case of superconductivity) on the electron transport and can't be neglected. One way to deal with it is the Fermi Liquid Theory. In this case, the many-electron dynamics in the crystal potential can be described by the same equations, but applied to "quasi-particles" with re-normalized dynamical properties as compared to fermions in a Fermi gas. [24]. In this case a quasi-particle consists of few interacting electrons with the momentum k_1, k_2, \dots, k_n , such that the energies $\varepsilon_i = \varepsilon(k_i)$ of these electrons satisfy the following conditions:

$$\varepsilon_1 < E_F, \dots, \varepsilon_m < E_F, \varepsilon_{m_1} > E_F, \dots, \varepsilon_n > E_F, \quad (2.25)$$

$$\varepsilon_1 + \dots + \varepsilon_m = \varepsilon_{m_1} + \dots + \varepsilon_n. \quad (2.26)$$

Those energies can be an arbitrary function of electron's momentum (unlike in the independent electron approximation with quadratic functions), however the energy as a function of quasiparticle position remains quadratic. As it follows from the condition 2.26 the quasiparticle occupied zero volume in momentum space and thus an electron in the quasi-particle exists at the Fermi surface for an infinitely long time at $T=0$. This fact as will be shown later in the work is important for the explanation of the intrinsic electron quantum transport phenomena, i.e. effects occurring in between scattering events.

2.3 Green's functions

Whilst the temperature effect or quasiparticles formation "smooths" the k axis in the band-structure and gives physical meaning to the ∂k of the ∇ -operator the equation 2.15, the $\partial\varepsilon$ as infinitesimal quantity still needs additional clarifications. All the eigenvalues $\{\varepsilon_n(k)\}_{n,k}$ form a spectrum of the Hamiltonian [26]. it remains discrete for the total crystalline Hamiltonian, since it consists of a finite number of eigenvalues.

For the general Hamiltonian $H_{general}$, i.e. $H_{general}$ is defined on whole space $L_2(\mathbb{R}^3, \mathbb{C})$, this is not the case and the spectrum is continuous since $L_2(\mathbb{R}^3, \mathbb{C})$ is an infinite-dimensional space

[26]. For this case, the discrete spectrum of the crystalline Hamiltonian H can be "smoothed up" using the Green's functions as eigenfunctions of general Hamiltonian.

The equation 1.1 for the stationary case can be represented in the operator form:

$$[\varepsilon - H]\psi = 0. \quad (2.27)$$

Then a function $G(x, x', \varepsilon)$ is called the Green's function if it satisfies the following condition [27]:

$$[\varepsilon - H]G(x, x', \varepsilon) = \delta(x, x'). \quad (2.28)$$

For $\varepsilon \neq \varepsilon_n$ the Green's function can be calculated in the following way:

$$G(x, x', \varepsilon) = \frac{\delta(x, x')}{\varepsilon - H} = \sum_n \frac{\phi_n^*(x) \phi_n(x')}{\varepsilon - \varepsilon_n}, \quad (2.29)$$

where ϕ_n is an orthonormalized basis such that $\sum_i \phi_i = \psi_n$. When $\varepsilon = \varepsilon_n$, however, the representation 2.29 is not well defined by the expression 2.29. In this case the following limits of the expression 2.29 can be considered to obtain that value:

$$G^\mp(x, x', \varepsilon) = \lim_{\delta \rightarrow 0} G(x, x', \varepsilon \pm \delta) = \sum_n \frac{\phi_n^*(x) \phi_n(x')}{\varepsilon - \varepsilon_n \mp \delta}. \quad (2.30)$$

The function $G^+(x, x', \varepsilon)$ is called advanced Green's function and the function $G^-(x, x', \varepsilon)$ is called retarded Green's functions. They can be used to find the local density of state, $D(\varepsilon) = \varepsilon^{-1}(k)$, in the following way:

$$D(\varepsilon) = \frac{1}{\pi} \text{Tr}(\text{Im}(G^-(x, x', \varepsilon))). \quad (2.31)$$

This way the $\delta\varepsilon$ used in the equation 2.15 can be calculated and the operator $\nabla\varepsilon$ can be formally applied. This approach will be used in chapter 4 for the calculation of orthogonal

Chapter 2. *Computational transport theory*

components of the velocity operator and AHC or SHC.

Chapter 3

Introduction into topology

Referring to the previous chapter's discussion, on continuity of the eigenvalues and momentum within a band, more details will be explored, by recalling basic concepts of topology and differential geometry. These mathematical theories have been developed to study internally made continuity and build a differential calculus on the set of discrete objects, by grouping objects into subsets introducing open neighborhoods. This process can be applied to the wavefunctions as an alternative to Green's functions approach to semiclassical transport.

The first section will focus on a formal way to introduce continuity of the eigenvalues in bands (called topology), by dividing bands into subsets, and then build a differential calculus by mapping these subsets to linear spaces, i.e. constructing a manifold. In the second section of the chapter, a tangent bundle is used as the main tool to define the derivative on the manifold.

3.1 Topological spaces and manifolds

As was shown in the previous section, semiclassical transport is implicitly based on the assumption, that the energy vs momentum relation can be described as a differentiable function $\varepsilon(k)$. At the same time, it was shown in chapter 1, that momentum is actually a discrete quantity. Thermal, or other perturbations, in the formalism of Green's functions, can be considered to create the continuity between discrete eigenvalue, but these methods are in some sense artificial. Another approach, based on a pure unperturbed state, can be applied as well.

This can be resolved, by the fact that the argument k in the contexts of electronic bandstruc-

ture is not just momentum, but also the corresponding eigenfunction $\psi_k(x)$. The wavefunction is an element of an abstract Hilbert space, so in order to build differential calculus on an abstract space, the subdivision into subsets, i.e. topology, needs to be introduced first.

Definition 6. *Topology on a space A is a set of subsets $\{U_i \subset A\}_{i=1}^{\infty}$, called open, such that [28]:*

- *Union of infinite number of subsets are in the set, i.e. $\cup_{i=1}^{\infty} U_i \subset A$*
- *Intersection of finite number of subsets are in the set, i.e. $\cap_{i=1}^N U_i \subset A$*
- *Empty set belongs to $\{U_i \subset A\}_{i=1}^{\infty}$ and is open*

Then a function on A is continuous if it maps any open set A_i into the open interval.

Lets apply this idea to the Hilbert space $\Phi_{crystal} \subset L_2(\mathbb{R}, \mathbb{C})$, corresponding to the energy spectrum $\{\epsilon_i\}_{i=1}^n$ of a Hamiltonian for crystalline material $H : \Phi_{crystal} \rightarrow \Phi_{crystal}$.

$$\Phi_{crystal} = span(\phi_1(x, k), \phi_2(x, k) \dots \phi_n(x, k)), \quad (3.1)$$

where $\phi_n(x, k)$ are the Bloch wavefunctions. The subspaces $\phi_i(x, k)$ play the role of coordinate axes for the Hilbert space $\Phi_{crystal}$. We can define open subsets as

$$U_i^{\Phi}(k_0) = span\{\phi_i(x, k), \text{ such that } \langle \varphi(k_0), \varphi(k) \rangle < \delta\}. \quad (3.2)$$

The above topology introduced on $\Phi_{crystal}$ is induced from the adiabatic theorem [29]: Bloch electrons will remain in the eigenstate $\phi_i(x, k_0)$ up to "slow" perturbation. Topological effects in electron transport are a consequence of the above topology on $\Phi_{crystal}$. Then $\varepsilon(k)$ is contentious if every set U_i defined by 3.2 is mapped to an open interval $(\varepsilon_1, \varepsilon_2)$

The next step to build a differential calculus on the abstract space is to map every open set to a linear vector space. For practical reasons, it's convenient to set up a map f to \mathbb{R}^n . Importantly the map f can vary from one set to another. Taken together maps covering all the open sets form an atlas f_i . Then the differential calculus can be traced back to the calculus on \mathbb{R}^n [30]. The advantage of such a construction of differential calculus for an abstract Hilbert space it that it has an observer-independent formulation.

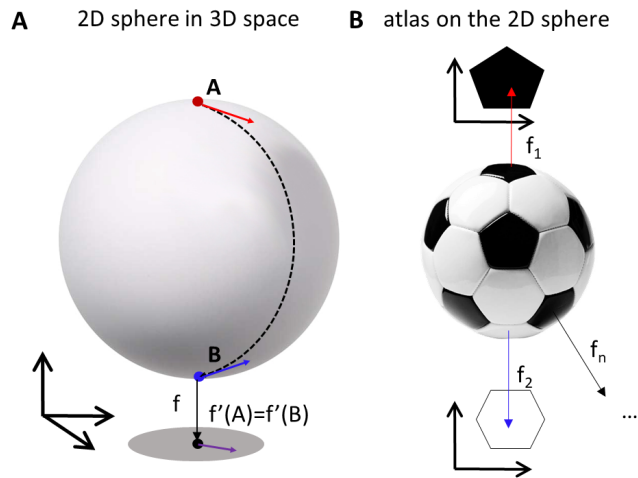


Figure 3.1: Sphere as 2D manifold: A degeneracy of the differentiation map for a sphere in 3D space, B: football as example of an atlas on the sphere that resolve degeneracy of differentiation map.

To illustrate this consider the Newtonian derivative (and correspondingly a velocity or momentum) as a local projection of a trajectory into a subspace of an ambient space is inconvenient for describing motion on a sphere in 3D space. As shown in figure 3.1, the projections of the North and South poles into the subspace are the same, and information is lost. Thus if a point moves on the surface according to equation $r(t) = r_0 + vt$, then without an implicit observer keeping information of the initial position, the North and South poles can't be defined with certainty. To resolve this, instead of considering a sphere as a map of the ambient space we can consider it as a union of separate maps from different copies of 2D planes, a.k.a. an atlas. This is shown in figure 3.1, illustrated using the example of a football where the sphere is tiled together from two maps made from curved hexagons and pentagons.

Here, the two maps and their tiling planes together with the map's corresponding transformations are known as a manifold. This mathematical construction does not require any coordinate system and all the properties of the sphere can be obtained from the tiled planes and corresponding maps, allowing differential calculus to be extended onto a set of abstract objects.

Definition 7. A manifold is a topological space, i.e. a set M of open subsets U_i , $M = \{U_i\}$, and for every subset there is a homeomorphism ϕ to a linear space from this subset.

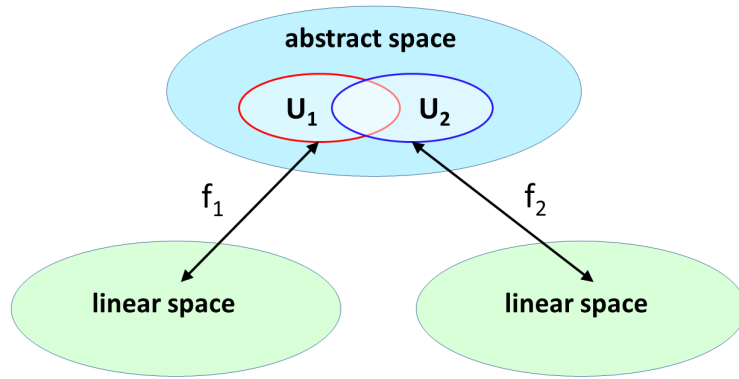


Figure 3.2: Schematic diagram of the construction of manifold on a topological space.

Schematically it's shown in figure 3.2 [31]. The dimensionality of the manifold is defined by the dimensionality of the linear space. If the atlas consists of maps to \mathbb{R}^n , then the manifold is respectively n -dimensional. In the earlier football example, all of the hexagons and pentagons are 2D and thus the overall sphere is a 2D manifold.

The differentiation on the manifold can be defined via derivative in the corresponding \mathbb{R}^n and this is known as exterior derivative [32, 33].

3.2 Tangent bundles

The derivative in \mathbb{R}^n , in fact, has different approaches. For the sake of building a differential calculus via external derivative on the manifold, the differential form approach is used. Differential forms generalize the concept of derivatives for multivariable functions [34]. There are two ways of such a generalization: either full differential or directional derivatives. As an example, consider a 2D band (in a sense of energy function of momentum) as shown in the figure 3.3. The surface of the 2D band in k -space can be represented as a family of 1D bands, which are intersections of the 2D band with planes $k_x = const$ and $k_y = const$ respectively. In this case Gâteaux derivatives at point (k_{x_0}, k_{y_0}) are defined as the tangent vectors to the corresponding 1D bands, which is an intersection of the 2D band with the planes $k_x = k_{x_0}$ for the derivative in the k_y direction and $k_y = k_{y_0}$ for the derivative in the k_x direction. In this way the 2D band sets two vector fields on the (k_x, k_y) plane.

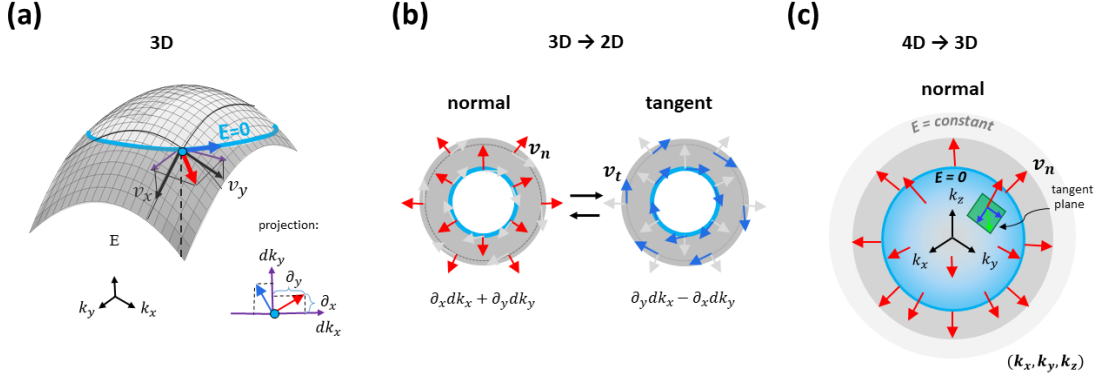


Figure 3.3: Construction of the tangent space. (a) Tangent vectors for a 2D band as projected into (k_x, k_y) plane (purple arrows) :the tangent vector to the FS in this coordinate system has coordinates $(\partial_x = \partial\varepsilon/\partial k_x, \partial_y = \partial\varepsilon/\partial k_y)$. (b) Equivalence between normal and tangent vectors for the 1D FS: one transforms to another by rotating 90° . (3) Normal vectors distribution on the 2D FS can be similarly replaced by the distribution of tangent plane, a.k.a. tangent bundle.

We can also construct a plane spanned by these tangent vectors, called a tangent plane or tangent space, denoted by $T_k M_{band}^{2-dim}$. Thus we obtain a distribution of tangent planes in 2D k -space, which is called Cartan distribution. Let us call the basis vectors in this plane dk_x, dk_y . We also can define the product of vectors from the tangent space, \wedge , as the wedge product. This is assumed to be antisymmetric, that means $dk_x \wedge dk_y = -(dk_y \wedge dk_x)$, which causes $dk_x \wedge dk_x = 0$. Geometrically the result of such multiplication of vectors in tangent space can be roughly understood as an "oriented area", which has the value of the area of the spanned parallelogram and its sign corresponds to the orientation of the vectors. Now since we can sum and multiply these vectors, we can write polynomial functions with those vectors. For example, the wedge square of the vector $(a, b) = adk_x + bdk_y \in T_k M_{band}^{2-dim}$ is :

$$(adk_x + bdk_y) \wedge (adk_x + bdk_y) = (ab - ba) \cdot dk_x \wedge dk_y. \quad (3.3)$$

These polynomial functions are called differential forms, or n-forms, where n is the number

of factors in the product. This is a geometrical analog of high order derivatives.

We can also define a product of n-form, called the "inner" product, as the multiplication of polynomials. The space of all n-form with this "inner" product generates an algebra called , exterior or Grassmann algebra of the \mathbb{R}^n space, denoted by $\Lambda(\mathbb{R}^n)$. For the \mathbb{R}^2 space it is an algebra made of 1- and 2-forms. Since we can also consider any n-form as a linear functional on the tangent space, the n-forms can be also understood as space of functions $L(T_k M_{band}^{n-dim}, \mathbb{R})$. This space is called a cotangent space at point k and denoted by $T_k^* M_{band}^{n-dim}$.

Definition 8. *The set of all $\{T_k M_{band}^{n-dim}\}_k$ and $\{T_k^* M_{band}^{n-dim}\}_k$ at every point of k-space are called tangent and cotangent bundle respectively.*

And thus any n-form on $T_k \mathbb{R}^n$ defines a function over \mathbb{R}^n according to the following diagram:

$$\mathbb{R}^n \xrightarrow{\text{partial derivatives}} T_k M_{band}^{n-dim} \xrightarrow{\text{n-from}} T_k^* M_{band}^{n-dim} \xrightarrow{\text{value of n-from}} \mathbb{R}. \quad (3.4)$$

This defines distributions on k-space like the wavefunctions define a distribution on real space. And, as it will be shown later, the properties of spinful real-space wavefunctions are connected with these functions on the k-space.

Chapter 4

Topological properties of the eigenstates

In the previous chapter, the electronic eigenstates within a band have been considered as a manifold. In this chapter, this approach to the bands will be applied to electron quantum transport in crystals resulting in observable anomalous phenomena.

The chapter starts with the physical motivation (from gauge invariance), for introducing topology on the eigenstates. As a consequence of it, the geometrical phases (and particularly the Berry phase) will be introduced in section two. The indexes describing eigenstate properties related to the geometrical phases, will be discussed in section three, inducing a brief overview of the topological quantum chemistry approach. And in the fourth and final section, the computational formalism for semiclassical quantum transport for the topologically non-trivial structure of the eigenstates will be discussed, with a focus on intrinsic anomalous and spin Hall effects.

4.1 Gauge invariance

Considering all possible transformations of the function, which preserve it as an eigenfunction of the Hamiltonian with the same eigenvalue. Assume Hamiltonian has just one eigenstate φ_n . For φ_n , the Hamiltonian acts as multiplication by the function $\varepsilon_n\varphi_n$, i.e.

$$H\varphi_n = \langle \varepsilon_n\varphi_n, \varphi_n \rangle = \varepsilon_n \langle \varphi_n, \varphi_n \rangle = \varepsilon_n \|\varphi_n\|^2. \quad (4.1)$$

Such a transformation will not change $\|\varphi_n\|^2$; if one wavefunction can be obtained from another via such a transformation, those wavefunctions are not distinguishable through observation.

The group of such transformations is called a gauge group [35, 36]. Since

$$\forall a \in \mathbb{C}, \quad \|a\varphi_n(x)\|^2 = |a|^2 \cdot \|\varphi_n(x)\|^2. \quad (4.2)$$

Multiplication by complex numbers with $|a| = 1$ form the group of such transformations. These numbers lie on a unit circle in the complex plane \mathbb{C} and the group of multiplications by such numbers is called $U(1)$, or the group of unitary transformations of the complex plane. The complex number $a = |a| (\cos(\alpha) + i \cdot \sin(\alpha))$ can be represented as an exponential function in the following way:

$$a = |a| e^{i\alpha}, \quad (4.3)$$

$$|a| = 1 \rightarrow a = e^{i\alpha}. \quad (4.4)$$

Thus the action of the $U(1)$ gauge is just a multiplication by the function $e^{i\alpha}$. If we represent the complex plane as the Riemann sphere, we can illustrate the $U(1)$ action as a rotation of the sphere [37]. Schematically it is shown in Figure 4.1.

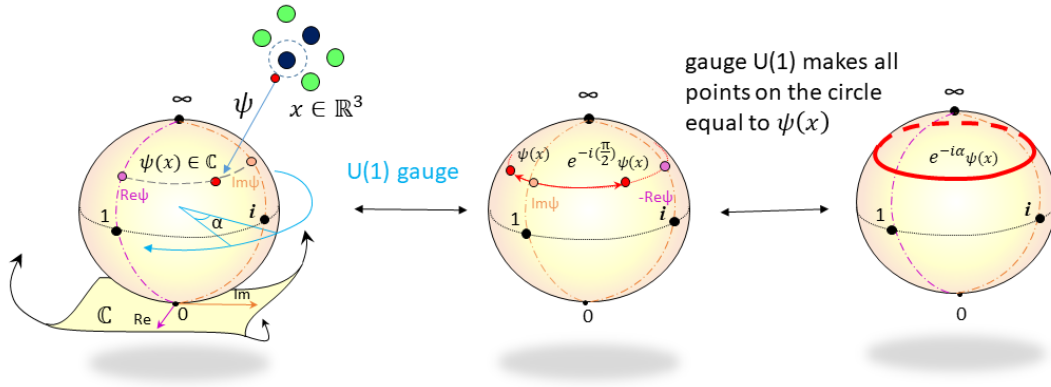


Figure 4.1: Action of the $U(1)$ gauge on complex space. The complex plane is represented as a sphere, by identifying poles on the sphere with zero and infinity on the complex plane. A point on the sphere represents value of the wavefunction $\psi(x)$. Multiplication by a complex number a $|a| = 1$ rotates the sphere and thus the point ψ moves along a circle parallel to equator of the sphere.

If the wavefunction corresponds to a fermion, according to the Pauli principle only 2 fermions with opposite sign spins can occupy the same energy state. So it is convenient to consider $\psi(x)$ as having two components $\psi = (\psi_{up}, \psi_{down})$, i.e. ψ is acting to $\mathbb{C}^2 = \mathbb{C} \times \mathbb{C}$. In this case the transformation of the vector (ψ_{up}, ψ_{down}) in the two-dimensional complex space \mathbb{C}^2 is described by a 2×2 complex matrix. For the same reasons as above, this matrix should be unitary, i.e it has determinant 1. All such matrices form a group $U(2)$. The eigenvalues of such matrices lie on the unit circle that implies any matrix A from $U(2)$ can be represented in the following form:

$$A = \begin{pmatrix} e^{i\alpha_1} & 0 \\ 0 & e^{i\alpha_2} \end{pmatrix}, \quad (4.5)$$

$$A\psi = \begin{pmatrix} e^{i\alpha_1} & 0 \\ 0 & e^{i\alpha_2} \end{pmatrix} \begin{pmatrix} \psi_{up} \\ \psi_{down} \end{pmatrix} = \begin{pmatrix} e^{i\alpha_1}\psi_{up} \\ e^{i\alpha_2}\psi_{down} \end{pmatrix}. \quad (4.6)$$

Thus if we represent (ψ_{up}, ψ_{down}) as two different points on the Riemann sphere then the action $U(2)$ is a simultaneous rotation of the point ψ_{up} , by angle α_1 and the point ψ_{down} , by angle α_2 . After the full circle rotation we arrive at the initial point making the space of parameters (α_1, α_2) a torus. This is shown schematically Figure 4.2.

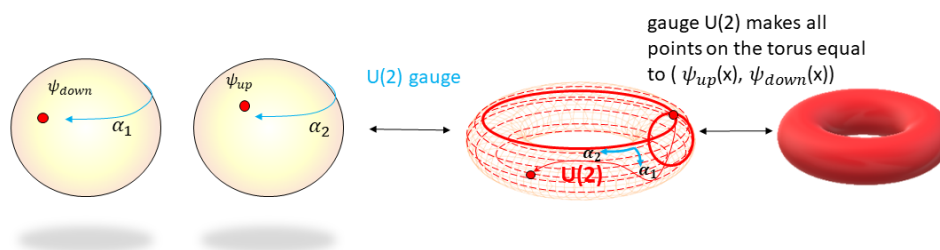


Figure 4.2: Action of the $U(2)$ gauge on the complex space. The two components of spinfull band (ψ_{up}, ψ_{down}) are the points on two spheres. Then if each sphere rotates, the total parameter space of angles of rotation is a torus.

4.2 Gauge induced topology and Berry curvature

First consider a one dimensional case. As it was shown before, the $U(1)$ gauge action can be represented as multiplication by the factor $e^{i\alpha}$. For an electron in a crystal it has the following form:

$$e^{i\alpha}\varphi(x) = e^{i\alpha}e^{ikx}u_k(x) = e^{i(kx+\alpha)}u_k(x). \quad (4.7)$$

Thus the action of the gauge can be considered as an additional phase factor or shift by α in reciprocal space. So the gauge allows the change of parameter k in time and all geometrical phases described above can be considered a result of the gauge symmetry. Schematically this is shown in Figure 4.3

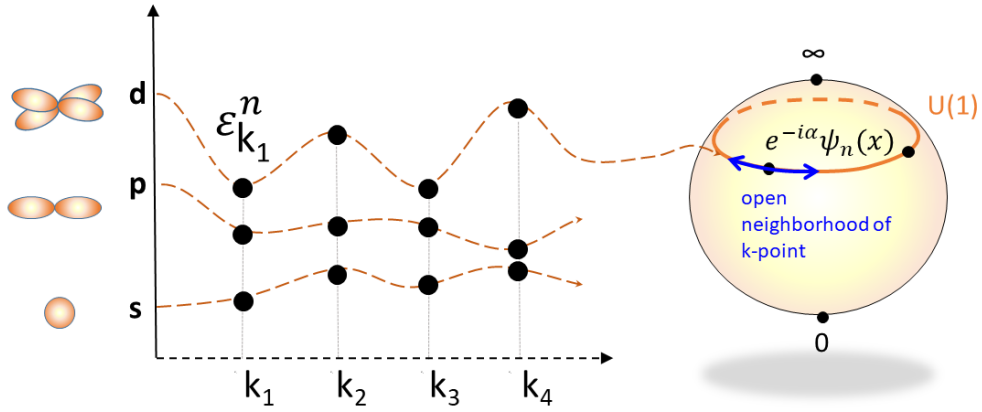


Figure 4.3: Gauge connection on the bandstructure. Disconnection between momentum is resolved due to geometrical phase represented as segment on the circle on the right.

If we consider k as a parameter changing in time then

$$\frac{d\varphi(k(t), x)}{dt} = -\frac{i}{\hbar}\varepsilon u(x)\frac{dk}{dt} + \partial_k u(x)\frac{dk}{dt}. \quad (4.8)$$

That gives rise to an additional phase factor to the solution of Schrodinger equation [38]:

$$\varphi_n(t) = e^{i\gamma_n(t)}e^{-\frac{i}{\hbar}\int_0^t dt'\varepsilon_n(k(t'))}\varphi_n(k(0)), \quad (4.9)$$

$$\gamma_n(t) = i \int_{\text{path } C} dk \langle \varphi_n(k) | \frac{\partial}{\partial k} | \varphi_n(k) \rangle . \quad (4.10)$$

If the path C is closed then $\gamma_n(t)$ is called the Berry phase. The expression

$$A_n(k) = \langle \varphi_n(k) | \frac{\partial}{\partial k} | \varphi_n(k) \rangle \quad (4.11)$$

is called the Berry connection and it is the vector field over all reciprocal space. We also can define a curl of this vector field which is called the Berry curvature:

$$\Omega_{i,j}^n(k) = \partial k_i A_j^n(k) - \partial k_j A_i^n(k). \quad (4.12)$$

It can be rewritten in terms of the periodic part if the Bloch wavefunction in the following way:

$$\Omega_n(k) = i \langle \nabla_k u_n(k) | \times | \nabla_k u_n(k) \rangle . \quad (4.13)$$

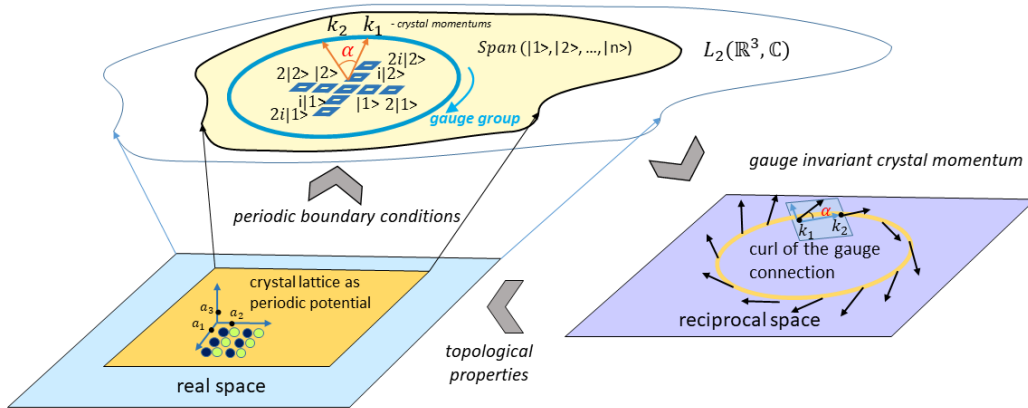


Figure 4.4: Gauge action on the reciprocal space.

Notice that if we change the direction of time $t = -t$, we change the route from counterclockwise to clockwise in the path integrals. If time reversal symmetry is broken and the clockwise integral is *not* equal to the counterclockwise integral, it requires the Berry connection to have a non-zero curl, i.e. non-zero Berry curvature.

If time reversal symmetry is not broken the Berry curvature still can be non-zero due to spacial symmetries. In this case, analysis can be done using topological indices resulting from the band structure, as is typical, when analyzing anti-crossings. This numerical method can be the basis for the algorithmic analysis of space group symmetry and its possibilities of yielding varying topologically non-trivial bandstructures.

4.3 Topological indexes, EBR, and connectivity of the eigenstates

It turns out that the existence of non-ordinary Hall conductance is an intrinsic property of the bands. The indicator that physicists use to identify this topological property of the bandstructure is called the Chern number, which is the integral of the Berry curvature of the band over the entire Brillouin zone [39].

$$C_{ij}^n = \frac{1}{2\pi} \int_{BZ} \Omega_{i,j}^n(k) d_{k_i} d_{k_j}. \quad (4.14)$$

In this case the Hall conductance of the n^{th} band is proportional to the Chern number, quantized in units of $\frac{e^2}{h}$ and can be calculated by the formula:

$$\sigma_{ij}^n = \frac{e^2}{h} \cdot C_{ij}^n. \quad (4.15)$$

The Chern number is a very powerful tool, it can be used not only for calculation of the Hall conductance but also to indicate a surface state. For example, the Chern number described above is the "first" Chern number and this non-zero number indicates surface conductance for a 2-D bulk insulator. For a 3-D bulk insulator, higher Chern numbers can be used to indicate surface states [39].

Another way to obtain a topological index is using the Wilson loop [40]:

$$W(l) = e^{i \int A(k) dl}, \quad (4.16)$$

where l is a loop in k -space and $A_{ij}(k) = \langle u_{i,k}, \nabla_k u_{j,k} \rangle$ is a Berry-Wilczek-Zee connection [39]. Note for this connection we need at least a two-band system, like (ψ_{up}, ψ_{down}) . The Wilson loop describes a parallel transport of the gauge field along the closed loop.

Mathematically a path between 2 points k_1, k_2 in k-space can be parametrized by an argument t in the following way: $k_t = tk_1 + (1-t)k_2, t \in [0, 1]$, when loop $k_1 = k_2$. The Wilson loop shows how the gauge varies with crystal momentum along a closed path in k-space; the final gauge phase should be the same as the initial. For example the parameter space of the U(1) gauge is a circle, thus moving along a loop in k-space the gauge phase can be either unchanged or equal to an integer number of full circles ($2\pi n$). We can consider also the class of equivalent loops: loops that give one circle of phase, two circles, etc. These classes of equivalent loops form a group, called a fundamental group [28]. As it was shown before, the parameter space of the U(2) gauge is a torus. The torus has two types of loops: one which shrinks into a point, and one which does not. Basically, it distinguishes the loops surrounding the hole in the torus, which cannot shrink, from the others. This is known as the fundamental group of the torus. The Wilson loop distinguishes those cases and yields a \mathbb{Z}^2 topological classification.

The gauge symmetry is the conservation of the eigenvalues and eigenstates of the momentum operator. The eigenstates of the momentum operator in a crystal are assumed to also be eigenstates of the operator of translation by a lattice vector. Orthogonality of the eigenstates implies that bands in the bandstructure should not intersect, i.e. not have identical E and k values. If two bands intersect that means the corresponding eigenstates $|\varphi_n\rangle, |\varphi_{n+1}\rangle$ are not orthogonal and the corresponding matrix representing the action of the Hamiltonian in the basis of eigenfunctions of the translational operator has off-diagonal terms. This is contradictory to the Hermitian rules of the Hamiltonian, i.e. its eigenstates should be orthogonal. This can happen when the eigenstates of the translation operator are not a suitable set of functions to form a basis. But how can this occur?

To understand this we can introduce Wannier functions as basis for representation of the eigenstates of the Hamiltonian, instead of eigenstates of a translation operator. The Wannier functions can be obtained from the Bloch eigenstates in the following way [41]:

$$\phi_R^n(x) = \frac{V}{2\pi^3} \int_{\text{BZ}} dk e^{-ikR} \psi_k^n(x), \quad (4.17)$$

where V is the real space primitive cell volume, R is the mass-center position vector. The Wannier functions essentially let one transform the band structure back from reciprocal space to real space and calculate $u_n(x)T$ in the following way:

$$u_{n,k}(x) = \frac{1}{\sqrt{N}} \sum_{l=1}^N e^{-ik(R_l-x)} \phi_n(x - R_l) \quad (4.18)$$

This allows relatively easy application of symmetry and the calculation of real space properties like the quantum spin Hall effect.

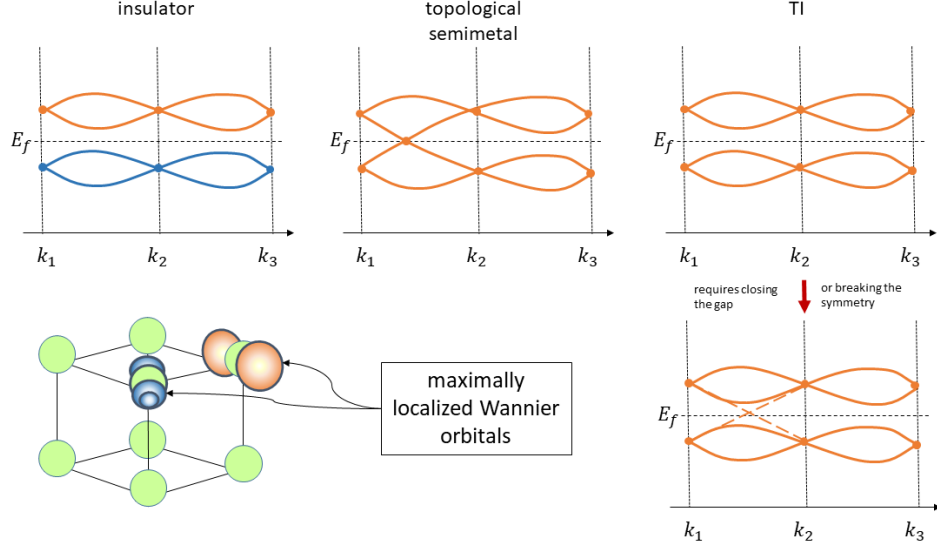


Figure 4.5: Connectivity of bands. Different colors of the bands represent different EBR corresponding to the atomic positions schematically shown in the same color. The difference between different topological materials is in the amount and location of the one EBR group of bands at the Fermi level.

Recently, a monumental work of this field was carried out where topological analysis and classification was done for all 230 crystallographic space groups that describe all possible arrangements of atoms in space[12]. In their work, Bradlyn et al use the fact that bands can form a connected group of bands in the bandstructure corresponding to Wannier functions centered at maximal Wyckoff positions, those whose site-symmetry groups are not a proper subgroup of any other site-symmetry group. This group of bands has the same elementary band representation or EBR. If a real compound's one EBR bands is connected but filled by only a fraction of the number of electrons required to fully occupy the set of bands, the compound is a symmetry enforced semimetal. If the bands have the same EBR, they should be connected and the set

splits into a gaped state with the Fermi level inside the gap, the compound must be a topological insulator and the bands become connected through surface states. Schematically this is shown in figure 4.5.

4.4 Berry curvature and anomalous transport effects

In the topological semimetal defined above there must be points, where locally linearly dispersive bands from one EBR intersect, i.e. topological semimetal must have Dirac or Weyl points (depending on degeneracy). In these cases, $\epsilon(k)$ is non-smooth, meaning the derivative $\partial\epsilon/\partial k_a$ is not well defined. Thus equation 2.14 cannot be applied and the Fermi liquid quasi-particle approximation is no longer valid. A plethora of work in the last decade has dealt with the ramifications of this, with Dirac/Weyl points resulting in the creation of "Dirac/Weyl quasi-particles" and the AHE/SHE due to uncompensated Berry curvature arising around a Dirac type degeneracy in the bulk band structure [42]. The Berry curvature then is involved in the semiclassical equation of motion of the particle in the following way: [43]

$$\frac{dx_i}{dt} = \frac{\partial\epsilon_n(k)}{\hbar \cdot \partial k^i} - \frac{dk_j}{dt} \cdot \Omega_n^{i,j}(k). \quad (4.19)$$

The way the Berry curvature is involved into this equation makes it fundamental to various Hall effects, i.e. quantum (integer and fractional) Hall effects (QHE), the anomalous Hall effect (AHE) and the spin Hall effect (SHE) [44], [45], [46]. The AHE is the current of conduction electrons, which is created perpendicularly to an applied electrical current without application of an external magnetic field in ferromagnetic metals due to the spins of the localized electrons [45]. It's schematically shown in figure 4.6. The AHE exists due to the magnetic interaction of localized and conduction electrons. The SHE is a transport phenomenon predicted by Mikhail I. Dyakonov and Vladimir I. Perel, consisting of the appearance of spin accumulation on the lateral surfaces of an electric current-carrying sample, the signs of the spin directions being opposite on the opposing boundaries [47]. It's schematically shown in figure 4.6.

There are ways to avoid degeneracy, however. If we consider the spinful case with U(2) gauge and include spin-orbit coupling(SOC) in the Hamiltonian, the 2 degenerate states become one connected state in terms of the two-component wavefunction. In this case the Dirac point becomes a source of Berry curvature and thus gives nontrivial spin dependent transport properties like AHE and SHE.

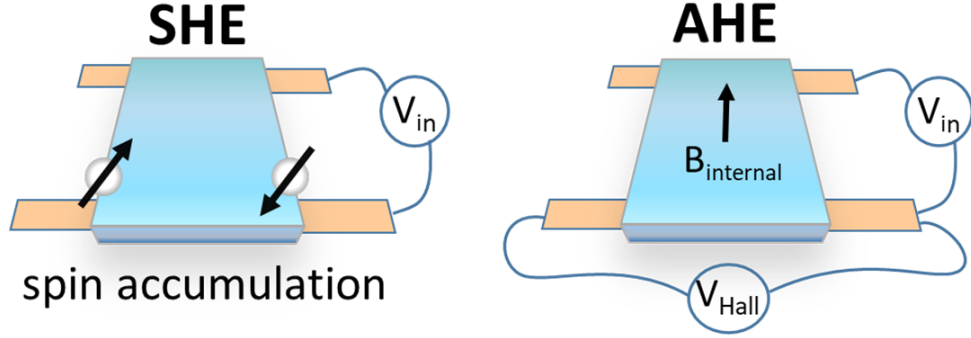


Figure 4.6: Spin and anomalous Hall effects. The applied voltage V_{in} results into spin accumulation on the sides of the sample for SHE or into perpendicular volatage V_{Hall} .

In the modern theory of Hall effects (SHE, AHE) there are several different mechanisms by which the AHE/SHE can be achieved but they can be generally grouped into two camps: extrinsic mechanisms and intrinsic mechanisms [48],[49]. Extrinsic mechanisms refer to the methods by which a spin acquires a transverse velocity from the scattering of electrons due to spin-orbit coupling. Impurity and defect scattering are the most common causes. Specifically, two important mechanisms are closely looked at today; skew scattering (where the electron's momentum is tied to its spin after a scattering event) and side-jump (where an electron's displacement from a scattering event was dependent on its spin)[44]. Thus the total SHC can be split in the following way.

$$\sigma_{xy}^H = \sigma_{xy}^{H-int} + \sigma_{xy}^{H-skew} + \sigma_{xy}^{H-sj}. \quad (4.20)$$

Only the intrinsic mechanism depends mostly on the electronic structure and so is more easily understood from the symmetry and material perspective. In the intrinsic mechanism the spin current is created in between scattering events rather than during them[50, 49]. The intrinsic contribution is directly proportional to the integration, over the Fermi sea, of the Berry curvature of each occupied band.

First let's consider AHE. The Berry curvature of the band, having degeneracy, is related to the antisymmetric behavior of the changing energy around the degenerate point and, particularly, demands the rotational component of the group velocity vector field over reciprocal space. The effect of the Berry curvature $\Omega_{xy,n}$ on the $AHC\sigma_{xy}^z$ can be expressed in the following way [46], [51]:

$$\sigma_{xy}^z = e^2 \hbar \int_{BZ} \frac{1}{2\pi} \Omega_{xy,n}^z f_n(k) dk^3. \quad (4.21)$$

The calculation of Berry curvature is carried out in practice using the Kubo formalism based on inter-band exchange [42]:

$$\Omega_{xy,n}^z(k) = -\hbar^2 \sum_{m \neq n} \frac{\text{Im}[\langle \psi_{nk} | v_x | \psi_{mk} \rangle \times \langle \psi_{mk} | v_y | \psi_{nk} \rangle]}{(\varepsilon_{nk} - \varepsilon_{mk})^2}, \quad (4.22)$$

where $\Omega_{xy,n}^z(k)$ was defined earlier in and v is the velocity operator and can be defined in the following way via Green's functions:

$$v = -\frac{1}{i\hbar} (x, (G^\pm(x, \epsilon)^{-1}). \quad (4.23)$$

This approach for calculation of the AHC has been applied to a variety of known AHE compounds and has shown good estimations of the experimentally measured intrinsic component of AHC. The calculated and experimental values are summarized in the table 4.1 [52, 53, 54, 55, 56, 57, 58, 59, 60].

Table 4.1: Calculated and measured AHC

Compound	Predicted AHC, $S/cm - 1$	Meausred AHCS/ $cm - 1$
Mn_3Ge	330	500
Fe	751	1000
Co	480	500
Mn_5Ge_3	964	860
$SrRuO_3$	100	200
Ni	2073	550
$Co_3Sn_2S_2$	1050	1200
Mn_3Sn	133	100
Co_2MnGa	1242	870
Co_2MnAl	1200	1800
KV_3Sb_5	450	350

Similar to how normal conductance was expressed as the FS integral instead of the integration over occupied states, the AHC is derived to be the FS property. According to the work [43],

the main contributor in AHE is the adiabatic motion of quasiparticles on FS. For the following parametrization of intrinsic Hall conductivity

$$\sigma_0^{ab} = (e^2/\hbar)\epsilon^{abc}(K_c/(2\pi)^2), \quad (4.24)$$

$$\epsilon^{abc}K_c = \frac{1}{2\pi} \sum_{n\text{-occupied}} \int d^3k \Omega_n^{ab} P_{BZ}(k) n_n^0(k, E_F), \quad (4.25)$$

where the function $P_{BZ}(k)$ is defined as 1 inside the BZ, 0 outside it and $n_n^0(k, E_F)$ is the ground state occupation at the Fermi level. Using the Fermi distribution function $f_n(k)$ the AHC can be expressed as the following integral:

$$\sigma_{xy}^z = e^2 \hbar \int_{BZ} \frac{1}{2\pi} \Omega_{xy,n}^z f_n(k) dk^3. \quad (4.26)$$

This formula 4.24 can be rewritten as an expression depending only on Fermi-surface integrals K_α instead of K_c

$$K_\alpha = \frac{1}{2\pi} \int_{S_\alpha} d^2\Omega_{k_F} + \frac{1}{4\pi} \sum_i G_{\alpha i} \int_{\partial S_\alpha^i} dA, \quad (4.27)$$

where $d^2\Omega_{k_F} = \Omega_{\mu\nu}(s) ds^\mu \wedge ds^\nu$ is the Berry curvature 2-form, $dA = A_\mu(s) ds^\mu$ is the connection 1-form for some surface parametrization $k_F(s)$ of corresponding sheet K_α and ∂S_α^i are the 1-manifolds where S_α intersects the Brillouin zone boundary, across which $k_F(s)$ jumps by $G_{\alpha i}$. The second term includes gauge dependent quantities, but for non-chiral S_α the BZ can be chosen so that all S_α are closed paths and then the the integrals in the second term contribute to the quantum Hall effect.

The first term in the 4.27 is an integer Chern number C_α . If some sheet of the Fermi surface has non-zero Chern number it must enclose a Dirac point, which is in this case is a source of Berry curvature. Since the total sum of the Chern numbers of all Fermi surface sheets must vanish due to gauge invariance, there must be another sheet with the opposite sign non-zero Chern number and a "spectral flow" mixing the eigenstates within the corresponding two bands.

Similarly the SHC can be calculated also using a linear-response approach in the Streda formalism [61]. In this case, the SHC is split into two parts:[62, 63]

$$\sigma_{xy}^{zI} = \frac{1}{2\pi N} \sum_k Tr[\hat{J}_x^S \hat{G}^R \hat{J}_y^C \hat{G}^A]_{\omega=0}, \quad (4.28)$$

$$\sigma_{xy}^{zII} = \frac{-1}{4\pi N} \sum_k \int_{-\infty}^0 \text{Tr}[\hat{J}_x^S \frac{\partial \hat{G}^R}{\partial \omega} \hat{J}_y^C \hat{G}^R - \hat{J}_x^S \partial \hat{G}^R \hat{J}_y^C \frac{\partial \hat{G}^R}{\partial \omega} - \langle R \leftrightarrow A \rangle], \quad (4.29)$$

where \hat{J}_x^S is a s_z -spin current operator ($J_j^i = \frac{1}{2}(S_i, v_j)$), \hat{J}_y^C is a charge current operator, \hat{G}^R, \hat{G}^A are retarded and advanced Green functions. In presence of anti-crossing bands (i.e. Dirac crossings) $\sigma_{xy}^{zI} = 0$ and the main contribution to the SHC comes from the σ_{xy}^{zII} . When the quasiparticle damping rate is equal to 0 (i.e. pure intrinsic regime), the σ_{xy}^{zII} can be reduced to the following expression:

$$\sigma_{xy}^{zIIb} = \frac{1}{N} \sum_{k,l} f(E_k^l) \Omega^l(k), \quad (4.30)$$

where $f(E_k^l)$ is a Fermi distribution function and $\Omega^l(k)$ is called spin Berry curvature defined by the expression:

$$\Omega^l(k) = \sum_{m \neq l} \frac{2 \text{Im}\{(J_x^S)^{ml} (J_y^C)^{lm}\}}{(E_k^l - E_k^m)^2}. \quad (4.31)$$

The spin Berry curvature, $\Omega^l(k)$, is modulated by the SOC magnitude and diverges around Dirac/Weyl points appearing in the (k_i, k_j) plane in the 3D bandstructure of the unperturbed electron state [64]. This divergence for degenerate bands is numerically simulated with a finite broadening, γ^2 [65]. However, the ingredients to this finite broadening do not fully represent a physical picture at finite temperature.

Chapter 5

Prediction of topologically driven spin Hall effect from first principles calculation

Chapter 5 is related to the search of high SHC compounds using the earlier described computational formalism for SHE. In the opening section a crystalline symmetry based mechanism of generation anti-crossing in the bandstructure will be considered. In the following section, the symmetry demanded anti-crossing will be considered as generators of the Berry curvature hotspots around the crossing points.

Section 3 will look at the A15 superconductors, having the required symmetries for anti-crossings, which will be analyzed for high SHE. The anti-crossings in W_3W , a compound with the highest SHC in the family (around $1900 \frac{\hbar}{e}(\Omega cm)^{-1}$), will be analyzed in comparison with calculated SHC as a function of energy. The spin Berry distribution around anti-crossing points will be also shown. The discussion on the orbital symmetry will be brought in and analysis of the band characters contributing in the anti-crossings for W_3W will be done. A possibility that crossings result into surface states as well as SHE will be shown on the example of Ta_3Sb . Other superconductors from the family (W_3Si , Ta_3Sn , Cr_3Os , Ta_3Os) will be also shown to have peaks of SHC aligned with the gaped anti-crossings in the bandstructure, however, these peaks are located away from the Fermi level. Therefore in section 4, the Fermi level adjustment discussion will be brought in as a strategy to maximize SHC. As an application of such an approach a novel compound W_3Ta , as chemical adjustment of W_3W with maximal SHC, will be suggested and shown to have experimental confirmation. Finally, a discussion on anti-crossings in

the bandstructures as a flag feature for a preliminary algorithmic search of high SHC candidates will be the conclusion of this chapter.

5.1 Crystal symmetries and gapped anti-crossings

Assume we have a point $x \in \mathbb{R}^3$ and we have a group $G_x = \{g_1, g_2 \dots g_m\}$, where g_i is a linear transformation of space that leaves x fixed. The group G_x is called a point group. Now if we act on the point x by translating by a lattice vector R

$$T_R(x) = x + R, \quad x \in \mathbb{R}^3,$$

we obtain the set of points

$$O_{T_R}(x) = \{y \in \mathbb{R}^3 : y = gx, \quad \forall g \in T_R\},$$

which is called the orbit of the action of the group of translations T_R on the element x .

If then we act by every element g_i on the point $y \in O_{T_R}$ we obtain a crystal lattice, i.e. the set of points in space that remain unchanged under the action of the group $G = G_x \times T_R$. In this case G is called a symmorphic space group. It means the quotient space

$$R \backslash T_R = \{x \in \mathbb{R}^3 : y = gx, \forall g \in T_R, \forall y \in \mathbb{R}^3\}$$

has a point, x , with site group symmetry that is isomorphic to the original point group G_x [66].

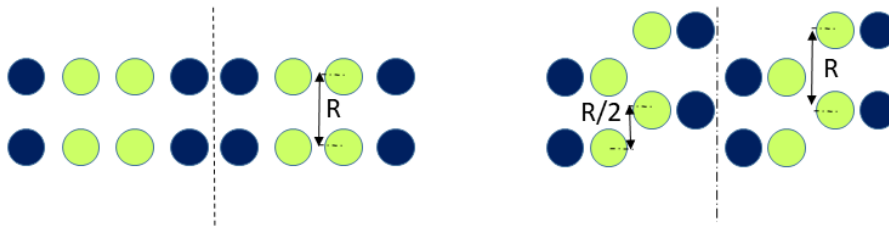


Figure 5.1: Symmorphic and nonsymmorphic symmetry.

Otherwise, if the lattice is invariant under the action of the group of linear transformations of a space that cannot be decomposed into $G = G_x \times T_R$ at least for one point x inside the unit

cell, G is called nonsymmorphic. In this case, some operations of the group G are not separable into a combination of rotation and translation by lattice vectors, i.e. they should be complex operations such as glide or skew operations. Examples of nonsymmorphic symmetry are shown in figure 5.1. The converse, in general, is not true, because some particular combinations of glides or screws can leave one point inside the unit cell fixed.

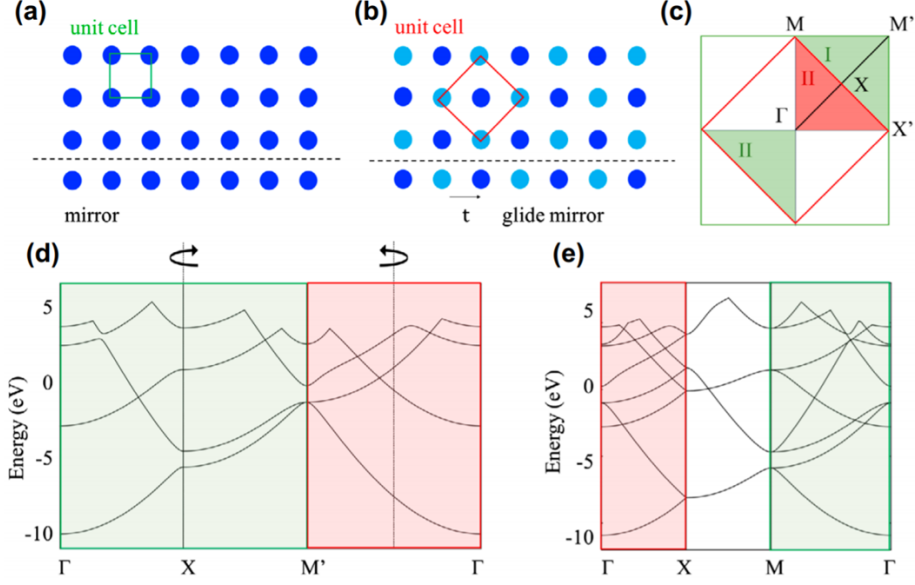


Figure 5.2: Bandstructure folding mechanism for non-symmorphic symmetry.

The band structures of nonsymmorphic symmetric crystals can be simply generated by the folding back procedure. Given the two unit cells in figure 5.2(a,b), one can construct the corresponding BZ as shown in figure 5.2(c), where the BZ of the symmorphic square lattice is shown in green and that of non-symmorphic square lattice is shown in red. The green shaded area I can be translated back to the green shaded area II, which is equal to the red shaded area by TRS because TRS implies $E_n(k) = E_n(-k)$. Since X lies exactly at the midpoint of Γ - M' and M - X' , when folding the Γ - X' - M' - M square in half across the M - X' diagonal like a sheet of paper, X - M' folds directly onto Γ - X . Similarly, $X'-M'$ folds onto $X'-\Gamma$. In addition, Γ - X' is equivalent to Γ - M , thus explaining the band structure in figure 5.2(e) as a simple folding of figure 5.2(d) [67]. In particular, Γ - X of the non-symmorphic square can be constructed by folding Γ - M' of the symmorphic square lattice in half, and Γ - M (which is equivalent to Γ - X') of the nonsymmorphic square can be constructed by the superposition of Γ - X' and $X'-M'$ of the symmorphic square

lattice [67].

5.2 Topologically driven spin Hall Effect

The spin Hall effect has become an important topic in recent years not just from a fundamental physics aspect, but also in regards to near future technological application. This is due to a combination of Moore's law limits on traditional Si-based devices and the concurrent rise of spintronics; creating logic and storage devices based on manipulating both spin and current [4]. Spintronics has become the next evolution in computing technology and is already seeing wide-spread technological adoption. In particular, the study of spin transfer phenomena, where the magnetization of a ferromagnet is manipulated through the transfer of spin angular momentum from a spin current, is considered a promising direction[5]. However, the creation of large spin currents, ideally at low power, room temperature, and using materials amenable to facile device fabrication, is still a challenge. The three major routes to achieving these criteria are a.) using heterostructures of ferromagnetic metals and nonmagnetic semiconductors, b.) using ferromagnetic semiconductors, or c.) using non-magnetic metals and the spin Hall effect. The direct conversion of charge current to spin current via the spin Hall effect is highly appealing for device design since it simplifies device heterostructures and reduces fabrication steps. However, the magnitude of the SHE in non-magnetic metals has been low; simple 3d, 4d, and 5d, elements have SHCs calculated to be less than a few hundred $\frac{\hbar}{e}(\Omega cm)^{-1}$ with the notable exceptions of Ta (BCC), W (BCC), and Pt (FCC) [68, 62, 69]. However, only Pt and recently β -W are known to host very large spin Hall angle's (SHA), which is the ratio of spin current generated to the charge current passed through a material, at room temperature, and larger SHE's could help result in the larger SHA's needed for applications[70, 71, 72].

The wavefunction, $\psi_n(k)$ is heavily influenced by the crystalline symmetries, which drive orbital hybridization and thus directly influence the Berry curvature and, correspondingly, the intrinsic SHC. Bands that create anti-crossings and then also form a hybridization gap with the inclusion of SOC will give rise to a large Berry curvature. This is because the Berry curvature is opposite for bands on either side of the hybridization gap, but when the E_F lies inside the gap, the oppositely signed contributions are not compensated[49]. This is well known as the cause of the large intrinsic SHE in Pt, where the Fermi level lies inside gaped anticrossings near the L and X points in the Brillouin zone (Figure 5.3) [62, 50, 63] When the Berry curvature of all occupied

bands is integrated over the entire BZ, Pt naturally has a peak in its SHC vs energy spectrum. Importantly, the magnitude of the SHE is inversely proportional to the size of the SOC-induced band gap; too large of a gap results in a low SHE but also a narrow peak in the SHC. In order to create a large SHA for use in spintronics, large SHE's are desired, and both extrinsic and intrinsic effects can contribute significantly to the overall magnitude of the generated spin current. Ideally, maximizing the SHE will be a combined effort of first picking a material with a large intrinsic effect and then maximizing extrinsic effects through interfaces, doping, defect control, etc. Few materials are known with large intrinsic effects, especially materials, that are amenable to large scale thin film fabrication through sputtering. However, if considering a strategy to search for or design new SHE materials, we propose the following approach: maximize intrinsic SHE by maximizing Berry curvature by having E_F inside as many small-gaped anti-crossings as possible.

The recent search for topological insulators (TIs), Dirac semimetals, Weyl semimetals, and now Dirac/Weyl Nodal Line semimetals has relied on an understanding of the effects of crystal symmetry on the electronic structure. The symmetry of a crystal structure and the orbitals making up the electronic states when bands are crossed determine which topological state is realized under consideration of SOC: the electronic states must be orthogonal to each other in order to not hybridize with each other and open a gap. The various symmetry operations (time reversal, inversion, mirror, rotation, screw, and glide) all can create degeneracies in the band structure at the special points or along the special directions. Some of these symmetries, or combinations of them, can create and protect a degeneracy from being gapped by the inclusion of SOC. For example, the C_{2v} point group (without spin) has four irreducible representations, but the C_{2v} double group (including spins) only has one irreducible representation. Since two bands with the same irreducible representation hybridize (meaning they are not orthogonal), spinful bands with only C_{2v} symmetry gap in the presence of SOC[73]. However a glide mirror G , for example, has a translation operation t which is a fraction of a primitive unit vector meaning that for spinless systems $G^2 = e^{-i\mathbf{k}\cdot\mathbf{t}}$ for Bloch states at k , and therefore the glide eigenvalues are $\pm e^{-i\mathbf{k}\cdot\mathbf{t}}$. In spinful systems, the glide eigenvalues are $\pm i e^{-i\mathbf{k}\cdot\mathbf{t}}$. Either with or without SOC, the glide mirror, which is a nonsymmorphic symmetry operation, yields two distinct eigenvalues, therefore the bands are protected from being hybridized and opening up a gap.

If one analyzes the crystallographic symmetry, it is possible to determine if a system must have unprotected and protected crossings and even along which k -paths they lay. Recently, there

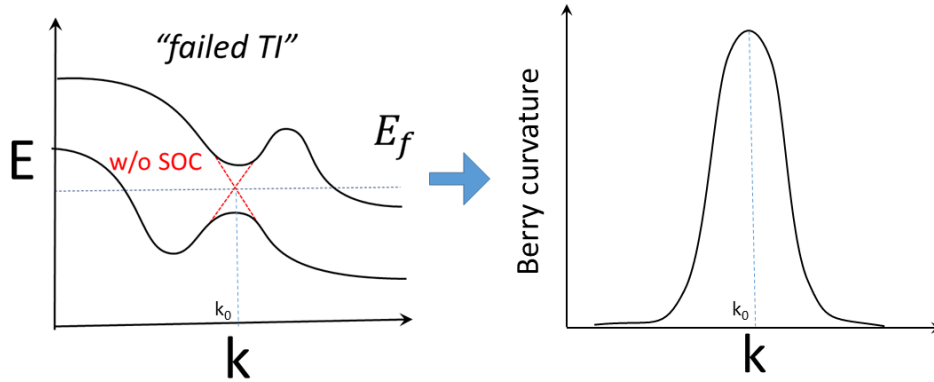


Figure 5.3: Schematic of the "Failed TI" bandstructure for the spin Hall purposes.

has been an intense effort to use symmetry and group theory to create a complete analysis of all topological classes possible in the 230 space groups[12, 74]. It turns out protected crossings are *not* extremely rare and unprotected crossings are actually commonplace. The possibility for SOC-driven gap openings is extremely frequent since even single, low symmetry rotation operations like C2 can demand a degeneracy without SOC. However, unlike the usual aim of material scientists working in the topological field, where the goal has been typically to put the *protected* crossings at the Fermi level, here the material scientist's goal, for spin and anomalous Hall effect (in the case of time-reversal symmetry breaking) purposes, is to put the *unprotected* crossings at the Fermi level. Good SHE and AHE materials (from a SOC perspective and not using the recent work in non-collinear magnetism[75, 76]) will have enough symmetry to demand crossings, but not the right symmetries to protect those crossings against SOC, at the E_F . This means that many of the materials which were once investigated as potential Dirac/Weyl semimetals but had SOC driven gap openings, or were investigated as potential topological insulators but had additional metallic bands, are worth re-examining for their spin and anomalous hall effects. Figure 1a shows a simple schematic of a "failed" TI band structure which, like Pt, results in a peak in the intrinsic SHC.

5.3 Symmetries demanded anti-crossing and spin Hall conductivity in the A15 superconductors family

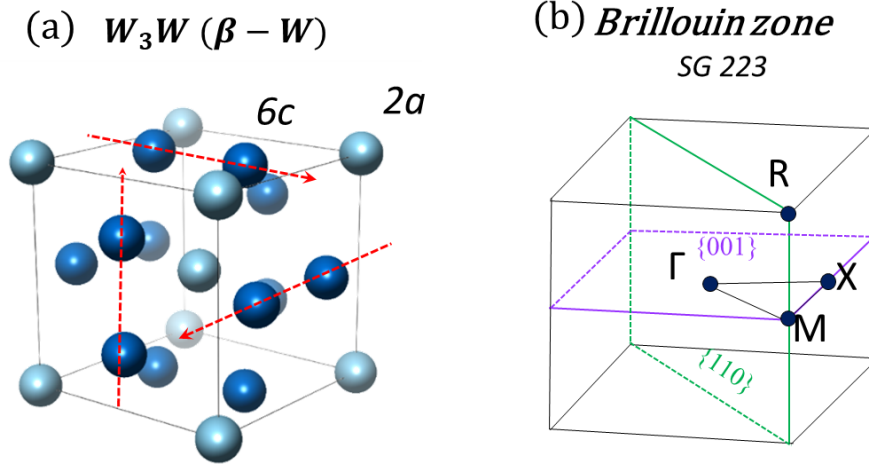


Figure 5.4: Crystal structure (a) and Brillouin zone(BZ) (b) for W_3W and A15 family (SG 223).

β -W, particularly when doped with small amounts of oxygen (few percent), is also known to have an enormous SHA as large as 0.45 which has been successfully used in spin transfer torque devices[77, 71]. To the best of our knowledge, no explanation has been given for its large SHC and correspondingly large SHA. However, it can be understood with the concepts outlined above; β -W has a large *intrinsic* SHE due to several unprotected crossings near the Fermi level resulting in a net large spin Berry curvature. Figure 5.4 (a) shows the crystal structure of β -W, a.k.a W_3W , the prototype of the A15 structure type (A_3X) in space group 223 (Pm-3n), which is famous for hosting high critical current superconductors like Nb_3Sn which are still the most widely used superconductors in technological applications today [78]. This is a Frank-Kasper phase where the metal center is in a high coordination environment (CN = 12). The structure has two distinct crystallographic sites (6a and 2c) and can be thought of as a BCC lattice made by the X atom with 2 A atoms in each face of the cube (evidenced by the different colored atoms) as shown in figure 5.4. This results in orthogonal infinite chains (denoted by the red arrows)

being formed by the A atoms. The BZ for this system is shown in figure 5.4 (b) with several key high symmetry points listed.

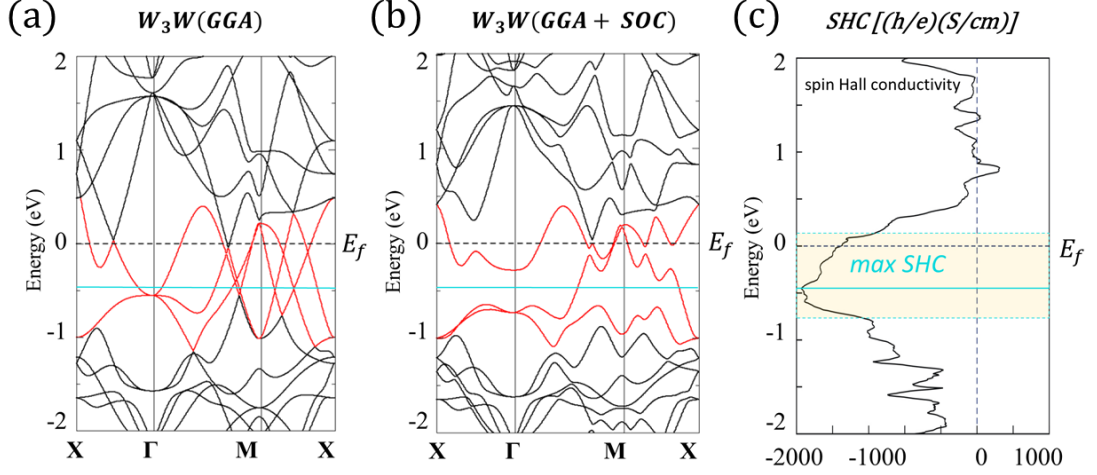


Figure 5.5: Electronic structures of W_3W without (a) and with (b) SOC, respectively. Dirac crossings are visible (without SOC) along the Γ -X-M lines, both at and below the E_F . Panel (c): spin Hall conductivity versus energy plot of W_3W .

The electronic structures of β -W, both with and without SOC, are shown in figure 5.5, respectively. Shown in red are bands that, without SOC, create several Dirac crossings very close to the Fermi level along the Γ - X - M lines, as well as below the E_F . These crossings are created by C2-rotation and inversion symmetries: for example, the crossing along Γ -X at the E_F , is protected by C2 rotations along (010) and (001) x inversion. However, the symmetries protecting these crossings all belong to the C2v point group, which, as described earlier, can create degeneracies without SOC but gap due to SOC. As expected, with the inclusion of SOC in figure 5.5, these bands gap out and the Fermi level lies almost within those gaps. Correspondingly a broad peak in the Energy vs SHC calculation (figure 5.5) straddles the energies where the gapped anti-crossings lie, but the maximum SHC actually lies approximately 0.5 eV below the E_F at the intersection of several more gapped crossings.

This creates "hotspots" of spin Berry curvature, indicated by the intense red and blue areas,

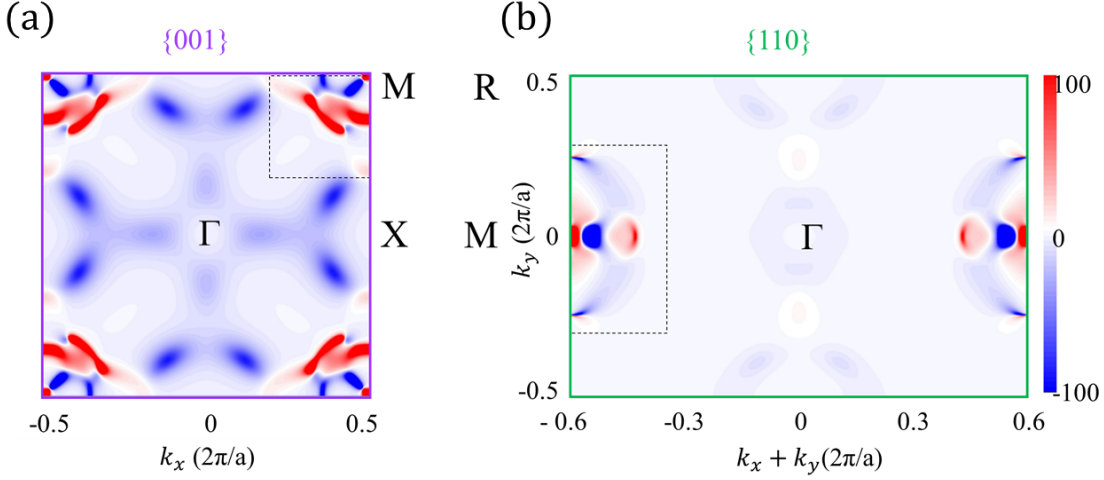


Figure 5.6: spin Berry curvature distribution in the the 001 and 110 planes of the BZ of W_3W where red and blue areas represent positive and negative regions.

in figure 5.6 in the BZ precisely where the anti-crossings were. If the E_F were lowered by hole doping without significantly altering the band dispersion characteristics, it is expected that the SHC could be maximized.

Figure 5.7 shows the electronic structure without SOC of β -W broken apart by the site and orbital contributions to the bands. The $2a$ site contributes almost exclusively to the degeneracy at Γ via the t_{2g} orbitals while the $6c$ site mixes with orbitals from the $2a$ site to create the crossings along Γ -X-M both near the E_F and below it. Without SOC, β -W has highly dispersive linear bands and Dirac crossings akin to a Dirac semimetal. Figures 5.7 (b) and (c) illustrate the extent of the orbital hybridization when SOC is included which gaps the Dirac crossings. The changing of color of the bands, particularly along the M-X direction below E_F , indicates the change of character from $d_{x^2-y^2}$ to the e_g and d_{z^2} orbitals, respectively. This is similar to what occurs in Pt, where strongly hybridized bands gap its Dirac crossing and result in mixed orbital character as well.

Another A15 compound, Ta_3Sb , also has an intriguing electronic structure, as shown in figure 5.8. The stoichiometric compound has a maximum SHC at E_F of $-1400 \frac{\hbar}{e} (\Omega cm)^{-1}$ as well as an

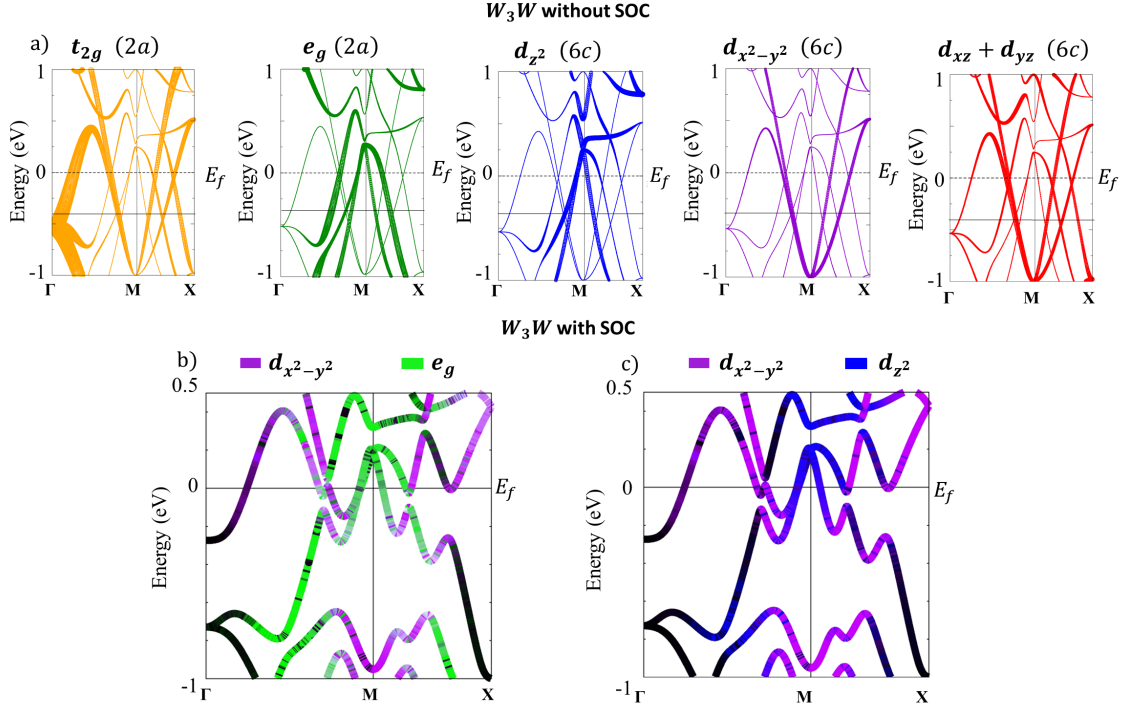


Figure 5.7: Panel a) The electronic structure of W_3W near the Dirac crossings decomposed into the various orbital and crystallographic site ($2a$ and $6c$) contributions. Thickness of the bands indicates the extent of the orbital or orbital group contribution to a band. By symmetry, the $2a$ site's orbitals group into the t_{2g} and e_g sets. The $6c$ site has lower degeneracy. The d_{xy} is not shown as it does contribute to the relevant bands. Panel b,c) The electronic structures with SOC included, illustrating the orbital hybridization driven by SOC, opening gaps and generating spin Berry curvature.

8-fold degenerate Dirac point at nearly at E_F at the R-point [79]. When projected to the 001 face, Ta_3Sb houses topologically non-trivial surface states, shown as the orange bands in figure 5.8 connecting the conduction bands and valence bands at X and M. Since this compound is also known to superconduct at 0.7 K [80], future experimental studies on both the spin Hall effect in this material as well the interplay of its topological surface states and superconductivity will be of great interest. To explore non-trivial topological surface state the \mathbb{Z}_2 topological index has been calculated. The result of calculations is shown in figure 5.8.

The calculations of SHC have been performed for other compounds in the A15 family. Due to the appropriate combination of orbital and space group symmetries, many of them show large

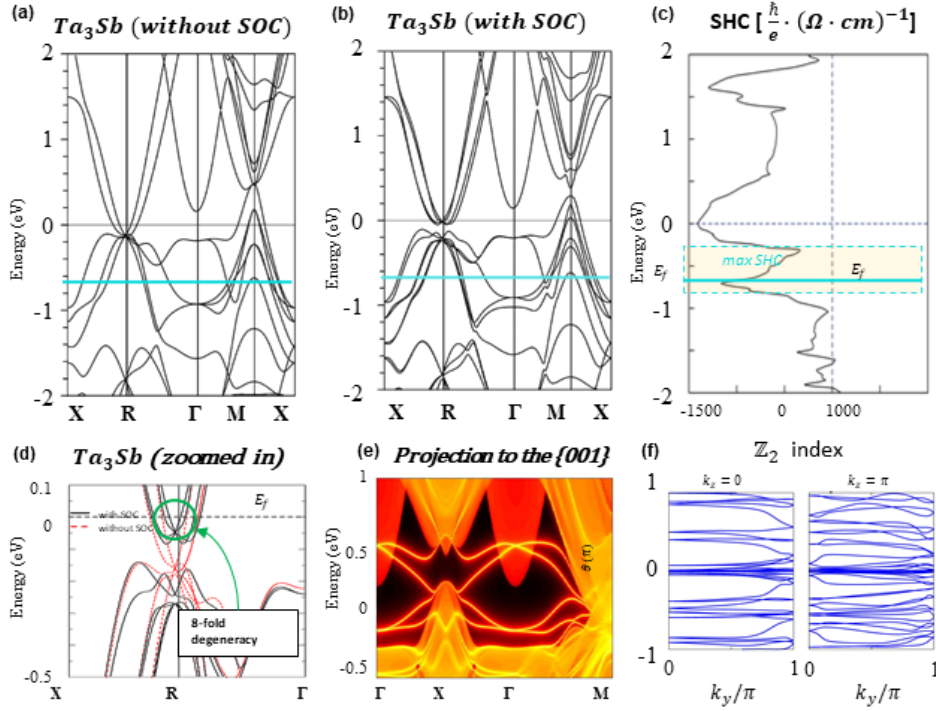


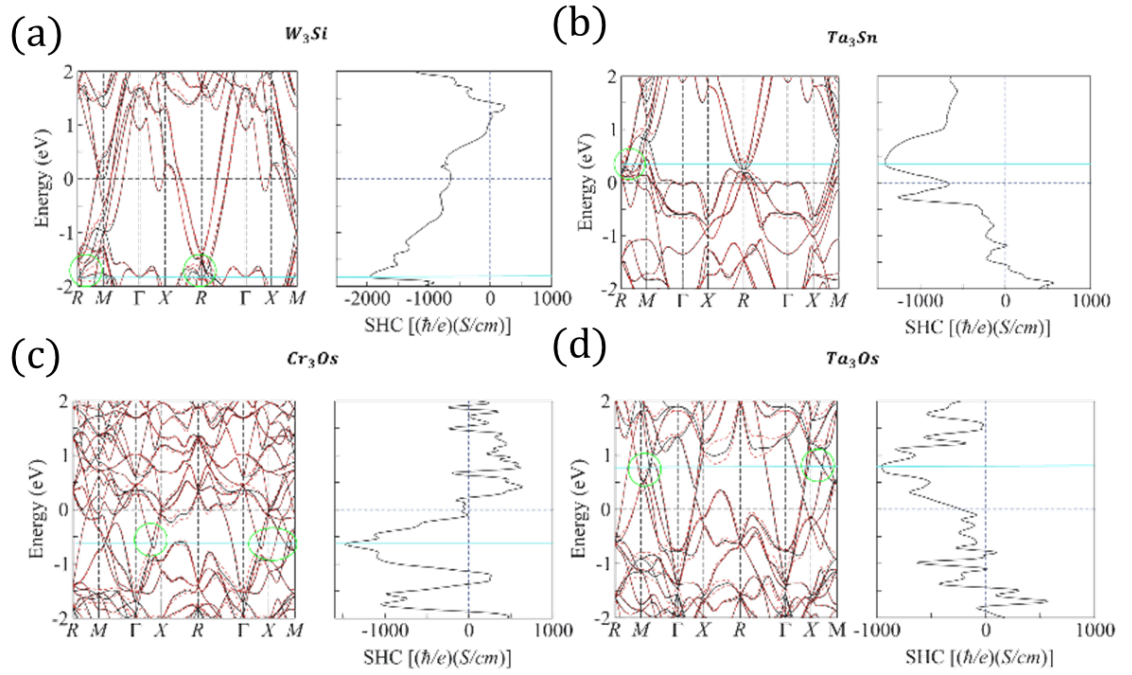
Figure 5.8: Panel **a,b,c**) Electronic structure of Ta_3Sb without and with SOC as well as its SHC versus energy plot. Ta_3Sb 's has a peak in its SHC at its E_F . Panel **d**) Zoomed in band structure highlighting the 8-fold degeneracy near the E_F . Panel **d**) Topological protected surface states (projected to the 001 face) in Ta_3Sb connecting the conduction and valence bands along X- Γ -M.

SHE. The highest values of SHC are summarized in the table 5.1, the corresponding bandstructures and SHC vs energy plots can be found in the supplementary information.

The bandstructures of medium SHC W_3Si and Ta_3Sn are shown in figure 5.9. As it's seen from the SHC vs energy graph the SHC is not maximized for these compounds because either unlike W_3W the Fermi level lies too far away from the SHC maximum (W_3Si) or even if SHC maximum is close to the Fermi level the SHC is changing too fast as a function of energy (Ta_3Sn). Figures 5.9 (c) and (d) show bandstructure and SHC vs energy relation for low SHC compounds Cr_3Os and Ta_3Os . Even in case of low SHC at the Fermi level the peak of SHC is located close enough to the Fermi level and comparable with W_3W in magnitude. Thus these compounds can still be considered as good SHC candidates, taking into account

Table 5.1: Calculated SHC for A15 compounds.

Compounds (Chemical formula)	SHC, S/cm^{-1}
W_3Ta	-2070
Ta_3Sb	-1400
Cr_3Ir	1209
Nb_3Au	-1060
Ta_3Au	-870
W_3Re	-780
Nb_3Bi	-670
W_3Si	-640
Ta_3Sn	-620
Nb_3Os	-460


 Figure 5.9: Bandstructures and SHC of (a) W_3Si (b) Ta_3Sn (c) Cr_3Os (d) Ta_3Os . The red line is without SOC and the black line is with.

- The computational error of DFT calculation of the Fermi level.
- The Fermi level can be chemically adjusted.

Since computational error can't be controlled, the chemical adjustment for a SHC material design strategy will be considered closely in the next section.

5.4 Chemical doping and design strategy to maximize spin Hall conductivity

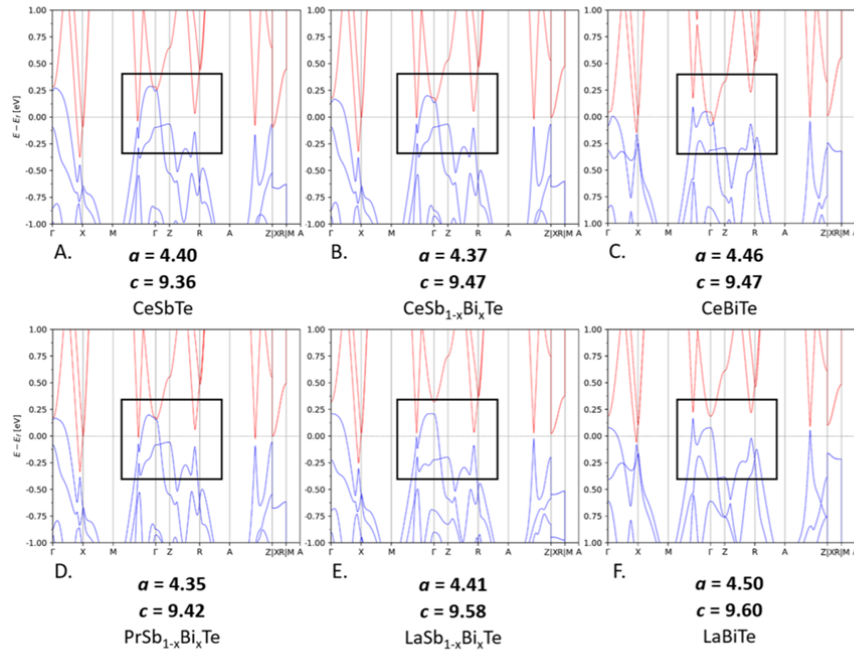


Figure 5.10: Adjustment of the Fermi level in the square net compounds $CeBiTe$.

The Fermi level separates occupied and unoccupied states, thus adding or extracting an electron per unit cell can move the Fermi level up or down respectively. Figure ?? shows this mechanism on the example of the square net compounds $CeBiTe$. By controlling the chemical composition, the unit cell size can be tuned without changing the symmetry and the band structure is engineered toward the topologically ideal case. Specifically, we find that $CeBiTe$,

with a larger square net, has dramatically reduced the size of the trivial pocket while keeping the Dirac crossing at X near the Fermi level. In addition, a heavily doped as close to as possible, is expected to completely gap the trivial pocket and be an ideal nonsymmorphic topological semimetal.

A similar doping strategy can be applied for β -W. Figure 5.11 shows the band structure of Ta_3Ta ; a hypothetical A15 version of Ta where both crystallographic sites are occupied by Ta instead of W. Due to the similarity of Ta and W, this can be thought of as β -W with 4 electrons removed. Figures 5.11 (b) and (c) show the band structures for Ta_3W and W_3Ta , respectively, also in the A15 structure type. In Ta_3W only the $6c$ site has been replaced with Ta while in the W_3Ta calculation only the $2a$ site was replaced. As can be seen from the band structures, the major features, including the Dirac crossings seen in β -W w/o SOC, are preserved although they have shifted with respect to the E_F by as much as 1.1 eV. This implies that Ta/W site ordering is not critical to the manifestation of the Dirac crossings and that even in a disordered thin film, as is expected from sputtered growth, the gapped crossings will persist. W_3Ta has shifted the Dirac crossings nearly exactly to the Fermi level and has a maximum calculated SHC of $2250 \frac{\hbar}{e} (\Omega\text{cm})^{-1}$; one of the highest values for any known compound. Thin films of this material, with interfacial spin transparency and conductivities similar to β -W, are expected to have very large spin Hall angles when coupled in heterostructures with Co/CoFeB/Permalloy. This confirms in the experimental realization and study of the spin Hall angle of this compound [81]

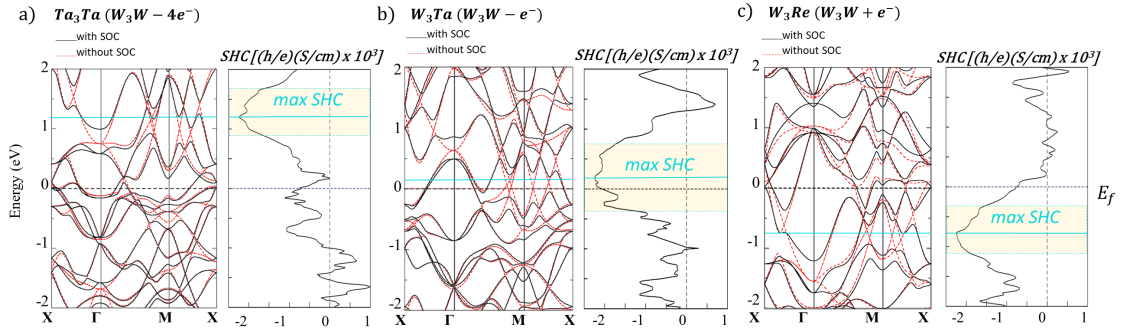


Figure 5.11: Electronic structures of Ta_3Ta , W_3Re and W_3Ta , without and with SOC included, as well as their spin Hall conductivity versus energy plots.

The state of the art in searching for large spin Hall effect materials has been limited by a

lack of a rational design strategy and a difficult candidate screening process. Materials are experimentally investigated in a combinatorial, serendipity driven approach or from a computation driven approach as follows:

- Material candidates are chosen based on containing heavy elements, Weyl points, or by the ease of fabrication,
- Electronic structures are calculated,
- Wannier functions are calculated,
- SHC vs energy calculations using the Kubo formalism,
- Adjustment of the Fermi level.

If the final SHC calculation showed a large conductivity, the material is experimentally investigated. This method of screening materials using computation is, however, very time and resource intensive primarily due to the requirement of finding good Wannier projections. Depending on the complexity of the crystal and electronic structures hundreds of projections need to be attempted before a reasonable one is found and the SHC can be calculated, which is why the search for large SHE materials has been largely dominated only by theoretical physicists. However, since we know the "flag" feature to look for (gapped Dirac crossings near the E_F) and given that Dirac crossings can be generated by crystallographic and orbital symmetries, it is possible to dramatically cut the screening time of SHC materials by

- choosing material candidates with high symmetry and heavy elements to generate gapped Dirac crossings;
- simply calculating the electronic structures with and without SOC and comparing them to look for the relevant feature.

Only for candidates with the right features near E_F does the Wannier projection and SHC need to be calculated. With this simple search strategy, materials scientists, chemists, and experimental physicists who don't have expertise in the details of transport theory can make significant contributions to the field. The calculations of SHC in the A15 family illustrate this strategy. Fitting the pattern, these compounds have maxima in their SHC at energies commensurate with their gapped anti-crossings.

Chapter 6

Fermi surface local geometry and Hall effects

Even if flag features in the bandstructure for a good SHE candidate, described in the previous chapter, reduce searching time, the key calculations of SHC remain time consuming, and, more importantly, they can hardly be automatized, unlike the flag feature search. A similar problem takes place for the prediction of other types of anomalous quantum transport, e.g. the AHE. The roots of it, as was explained in sections 2.2 and 2.3, is that the operations of differentiation and integration for semiclassical approach are handled externally via the use of Green's functions. Not only complexity of calculations is increased by this procedure, but accuracy as well, as can be seen from the comparison of the predictions of AHE and measured values in the table 5.1. The topological treatment began to solve this problem by including the Berry curvature term in the semiclassical equations of motions, however, even for improved basic transport equation the calculation of the conductivity has been approached similarly as before, i.e. via the Green's functions.

The Fermi Surface (FS) can be a good starting point to develop a novel approach as it determines electron transport properties in metals, in the assumption that it is a differentiable surface. Here, similar to how topology was introduced for Hamiltonian eigenstates, continuity can be introduced for the points at the FS to make it differentiable. The FS of a topological semimetal, however, has degenerate points, where either differentiability fails (irregular degeneracies), or dimensionality fails (isolated degeneracies), this makes the semiclassical approach

inapplicable, even with Green’s functions formalism. Whilst for the isolated degeneracies, the theory has been developed well and they were related to the different surface states (famously on the example of TI), the effect of the irregular degeneracies on the quantum transport hasn’t been derived explicitly. Whereas some studies were connecting irregular points with the topological properties of the eigenstates via Berry curvature monopoles, which will be illustrated in the first section; other studies were focused on the geometrical properties caused by irregular points, connecting them with the global dynamics of electrons in the momentum space.

The important step towards local surface geometry effect on the electron transport has been done by Ong [82], by moving consideration of the electron dynamics from the momentum space to the space of the ”scattered path lengths”, which is $\{v_k\tau_k\}$. This construction is similar to the construction of tangent space to the $\varepsilon(k)$, however, the Fermi surface orbits were projected only to one tangent plane T_0E_F and thus the tangent plane was used just for a different point of view on the global dynamics. The difference between global dynamics in the momentum space and local dynamics in the tangent space will be discussed in the second section. The tangent bundle construction and Riemannian metrics will be introduced to study local dynamics. Then the Fermi surface can be understood as a composition of local regions of these different types: elliptic, hyperbolic and Euclidean.

The main result of this approach, which is the investigation of locally hyperbolic regions of the Fermi surface and its relationship to the intrinsic anomalous and spin Hall effects, will be presented in section three. The metric, \mathbb{H}_F , is used for measuring the hyperbolicity of the Fermi surface and correlates extremely well with experimentally measured values of intrinsic anomalous Hall conductivity (AHC) ($R^2 = 0.97$). This is shown for 16 different real materials that broadly range from conventional ferromagnets to Weyl semimetals, including cases like Ni and Co_2MnAl , where the Berry phase approach (via the Kubo formalism) does not represent a complete picture of the transport. This Fermi Surface local geometry effect also works consistently with the recent formulation of topological quantum chemistry [12]: 13 of the compounds have FSs generated from bands with a single elementary band representation (EBR) and that the limit of the AHC for a single EBR FS is $\approx 1570 \frac{\hbar}{e}(\Omega\text{cm})^{-1}$. Two of the materials examined here, CrPt_3 and Co_2MnAl , have cooperative multi-EBR Fermi surfaces and subsequently break the apparent AHC limit, which will be discussed in section four. The \mathbb{H}_F index enables an inexpensive and rapid computational prediction of AHE/SHE materials and can be implemented with existing density functional theory (DFT) methods and databases.

6.1 Anti-crossings and non-differentiable Fermi surface orbits

As was defined earlier, Dirac points at the Fermi level in the 3D bandstructure of topological semimetals form irregular degeneracy at the FS. At this point the band $\varepsilon(k)$ is not differentiable in the direction where the Dirac anticrossing appeared. Since, as it was shown in chapter 3, the directional derivatives define the tangent vectors of the Fermi surface at this point, the tangent vectors in the corresponding directions of the FS are also not well defined.

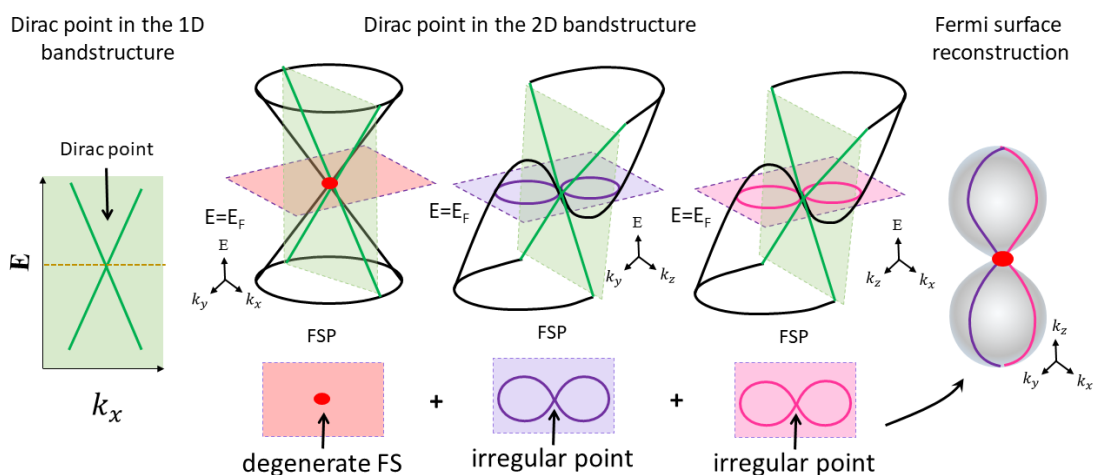


Figure 6.1: Connection of a Dirac point to an irregular Fermi surface orbit.

Assume the Dirac point, appeared in the k_x direction, stays a Dirac point in the (k_x, k_y) plane (see fig. 6.1). Then the tangent vectors to the FS cross-section (i.e. FS orbit) at the $k_z = 0$, are not well defined. Indeed, the Fermi surface in this case just a point, and thus the tangent vectors can't be defined. In order to obtain the total 2D Fermi surface for 3D bandstructure two other cross-sections (at $k_y = 0$ and $k_x = 0$) should be lines and tangent vectors, that then can be defined at the Dirac point. Then the bandstructure at these planes should look like in fig. [?]. However, passing through the Dirac point tangent vector turns back, and thus the $\partial_k \varepsilon(k)$ is discontinuous function at the Dirac point. This means the effective mass cannot be defined at the Dirac point. This can be resolved by introducing a quasiparticle at this point, then the $\varepsilon(k)$ doesn't have to be a smooth function. These quasiparticles are referred to as massless Dirac

fermions, since around the Dirac point the bands are linear and thus the effective mass is zero. The tangent vector to the FS can be represented via $\partial_k \varepsilon(k)$, therefore the turn of the $\partial_k \varepsilon(k)$ must correspond to the turn of the tangent vector to the Fermi surface orbit (i.e. cross-section). If we look at the corresponding FS orbits (purple and pink lines in the figure) then at the Dirac point they are self-intersected and the tangent vector, in fact, does the turn at the point of self-intersection. This type of orbit is called irregular.

The shown above example raise up the question: what is causing the anomalous transport phenomena (like SHE or AHE) - the irregularity of the orbits or degeneracy in the bandstructure? Of course, as is shown in figure 6.1 the Dirac points can generate irregular orbits if they appear as irregular degeneracy at the Fermi surface. However, is there a scenario when the irregular orbits appear independently from Dirac points and will they still result in anomalous intrinsic transport? To answer this question the tangent bundle will be considered closely in the next section.

6.2 Local properties of the Fermi surface

The Fermi surface orbits discussed before only as a line enclosing the whole surface (or an isolated sheet of the surface). These types of orbits will be referred to later in the text as global orbits. However, there's another type of the orbits: the local orbits, i.e. orbits defined as cross-sections of the FS with the tangent plane at point $T_k E_F$. Notice that locality means that they depend on the choice of the point k . Schematically it's shown in figure 6.2.

The local orbit can be also classified as open and close, but for local orbits open means prolongation into the next tangent plane, whereas for global it's a prolongation into the next reciprocal unit cell. Then the global orbits (both open and close) can be made out of the locally open orbits. This way the semiclassical dynamic along the global orbits (e.g. in case of magnetic field) can be rewritten as dynamics along the locally open orbits: the dynamics in the external field defines the transition of a particle from one k point to another and thus it also generates a map between corresponding tangent planes:

$$\begin{aligned} B^T &: T_k E_F \rightarrow T_{k+\delta k} E_F, \\ E^T &: T_k E_k \rightarrow T_{k+\delta k} E_{k+\delta k}. \end{aligned} \tag{6.1}$$

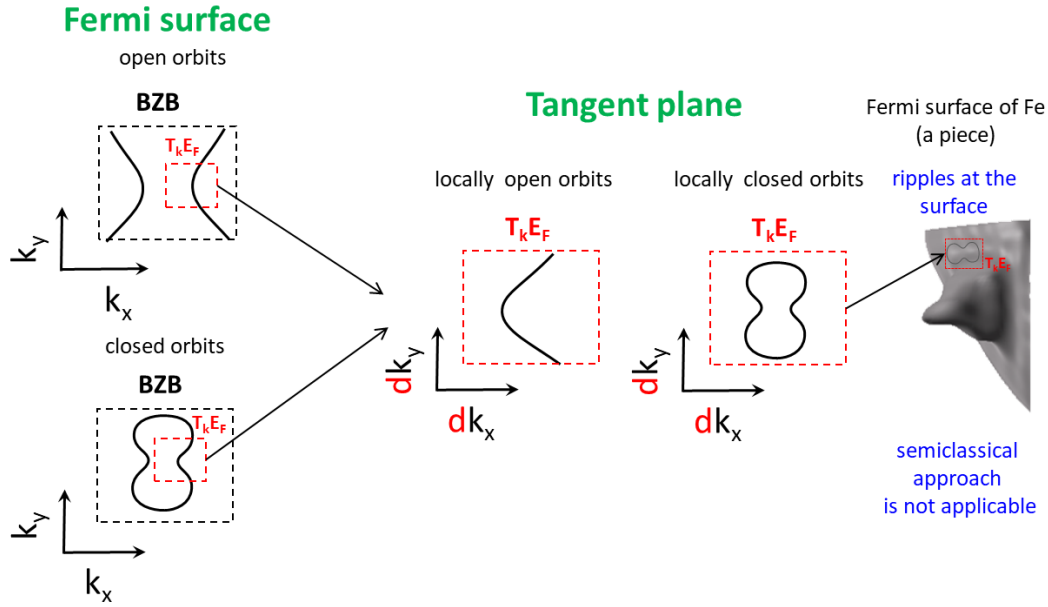


Figure 6.2: Relation between local and global Fermi surface paths.

The local orbits can be used to classify the local geometry of the Fermi surface. The First and the Second Fundamental Forms forms are used. In order to do this classification. [83]:

$$I = \begin{pmatrix} g_{11} & g_{12} \\ g_{21} & g_{22} \end{pmatrix}, g_{ij} = \langle dk_i, dk_j \rangle, \quad (6.2)$$

where δk_i is the tangent vector to the FS in the i direction. The scalar product, g_{ij} , in the tangent plane $T_K E_F$ at every point K defines a Riemannian metric on the Fermi surface. Hence the Fermi surface can be considered as a 2D Riemannian manifold [84].

$$II = \begin{pmatrix} L & M \\ M & N \end{pmatrix}, k_l = L \frac{dk_i^2}{2} + M dk_i dk_j + N \frac{dk_j^2}{2} + \dots, \quad (6.3)$$

where $k_l = f(k_i, k_j)$, a parametrization of surface.

The Gaussian curvature is then defined by the ratio $K = \det II / \det I$ and used as classifying invariant of the local geometry of the surface in the following way: $K > 0$ corresponds to elliptic; $K = 0$ to Euclidean, and $K < 0$ corresponds to hyperbolic (figure 6.3) [85, 86]. In fact, Euclidean geometry is particularly hard to distinguish from hyperbolic or elliptic since numerical simulation of the FS always gives a small computation error which results in a very

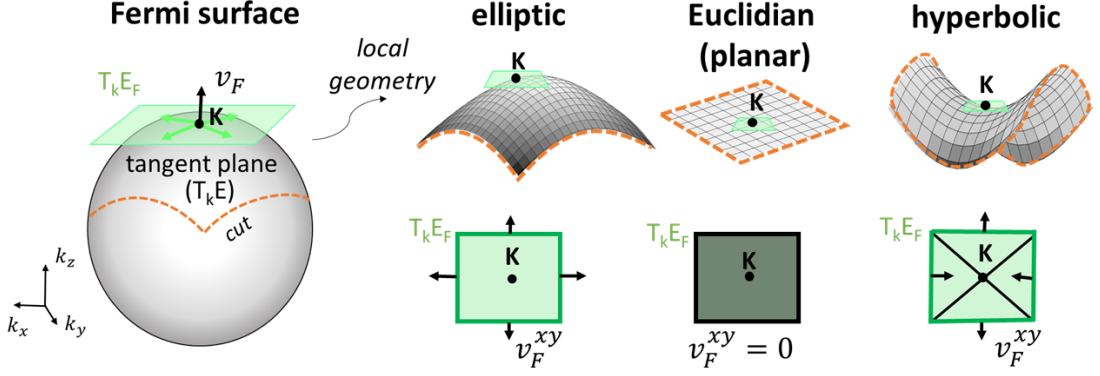


Figure 6.3: (a) Schematic representation of a typical Fermi surface where the green plane ($T_K E_F$) represents the tangent plane at point K on the Fermi surface and v_F is the group velocity. (b) A locally elliptic cut of a Fermi surface with tangent plane and velocity vectors drawn as green arrows. (c) A locally Euclidean cut and (d) A locally hyperbolic cut. E. Illustration of anomalous Hall (AHE) and spin Hall (SHE) measurement geometries.

small positive or negative K ; hence numerical determination of Euclidean regions are heavily dependent on practical tolerance factors.

Every type of geometry also results in dimensionality of the intersection between the FS and the tangent plane: a center and a point for elliptic, a saddle and lines for hyperbolic, as schematically shown in figure 6.3 in black color on the green square representing $T_K E_F$, and the solid line is the intersection of the FS and $T_K E_F$. Thus local orbit exists only in hyperbolic and Euclidean case.

The local orbits corresponds to the global orbits, if the magnetic is field applied in the direction of the normal vector to the tangent plane. In case of AHE or SHE there's no external magnetic field, however, there's an internal magnetic field related to the spins of electrons. Consider now a spinful system. For the spin - $\frac{1}{2}$ system it means the FS can fit two electrons. We can equip the k -space with a quadratic form.

$$Q_{m,n}(k) = \langle \psi_{m,k}; \psi_{n,k} \rangle. \quad (6.4)$$

If the band is degenerate like in case of Kramers degeneracy (with pure electric field E_x), then the form $Q_{m,m+1}$ is zero at every point in the \mathbb{R}^3 k-space. In this case the Grassman algebra of the \mathbb{R}^3 k-space is isomorphic to the Clifford algebra $Cl(\mathbb{R}^3, Q_{m,m+1})$, which is isomorphic to the algebra generated by Pauli matrices $\sigma_x, \sigma_y, \sigma_z$. Since the tangent space of the band $T_k M_{m,m+1}$ band is isomorphic to \mathbb{R}^3 , we have the following diagram of equivalence:

$$\Lambda(T_k M_{m,m+1} \text{ band}) \simeq \Lambda(\mathbb{R}^3) \simeq Cl(\mathbb{R}^3, Q_{m,m+1}) \simeq Alg(\sigma_x, \sigma_y, \sigma_z). \quad (6.5)$$

The algebra of Pauli matrices is used in the spin projection operator $S_i = \frac{\hbar}{2} \sigma_i$ and spin current operator $J_j^i = \frac{1}{2} (S_i, v_j)$ for the electric field in the i-direction and the spin Hall conductivity formula 4.31.

6.3 Hyperbolicity and anomalous orthogonal transport

Let us assume that the *tangent plane is parallel to the AHE plane*. The black arrows in the figure 6.3 b,c,d (bottom) then represent the in-plane component of the group velocity v_F^{xy} , i.e. the projection of v_F to the AHE plane. As one can see for the elliptic case, the electron can have a v_F^{xy} in any direction on $T_K E_F$ but for the Euclidean case there is no in-plane component of the v_F and thus dynamics may happen only out of plane. For the hyperbolic case, however, $T_K E_F$ is split into two regions; v_F^{xy} pointing towards K , where quasi-particle doesn't leave the tangent plane unless it moves into the other region, v_F^{xy} pointing away from K . Around an infinitesimal neighborhood of K , v_F^{xy} is demanded to be in a single direction, for example, the y direction.

Even if we consider a particle moving on the plane, the real particle is still moving in 3D space and we need to consider the 2D Fermi surface for the full analysis of the particle's dynamics. Assuming that the Fermi surface is parametrized as $k_F = (k_x, k_y, k_z(k_x, k_y))$, allows us to include the z-direction into the 2D model implicitly. In this case the equation (2.15) becomes the following:

$$v_n(k_F) = \frac{1}{\hbar} \left(\frac{\partial \varepsilon_n}{\partial k_x} + \frac{\partial \varepsilon_n}{\partial k_z} \frac{\partial k_z}{\partial k_x}, \frac{\partial \varepsilon_n}{\partial k_y} + \frac{\partial \varepsilon_n}{\partial k_z} \frac{\partial k_z}{\partial k_y} \right). \quad (6.6)$$

For the hyperbolic regions of the Fermi surface $\text{sign} \frac{\partial k_z}{\partial k_x} \neq \text{sign} \frac{\partial k_z}{\partial k_y}$, assume $\frac{\partial k_z}{\partial k_x} < 0, \frac{\partial k_z}{\partial k_y} > 0$. Then we can rewrite (6.6) as the following:

$$v_n(k_F) = \frac{1}{\hbar} (I_{2 \times 2} \nabla_k \varepsilon_n(k) + \frac{2}{\hbar} S_z v_z(k) \nabla_k |k_z|). \quad (6.7)$$

For a spinless system the second term vanishes, but for spin $\frac{1}{2}$ electron $S_z \neq 0$. As we can see from (6.6) v_x component of the velocity decreases and v_y increases by the term $\frac{2}{\hbar} S_z v_z(k) \nabla_k |k_z|$. This means around the hyperbolic point the electron gains velocity in the y-direction due to non-zero component S_z without any applied fields. However, as it can be seen from the figure 6.3, this velocity can be self-compensated due to the symmetry around the point. Thus, the condition of hyperbolicity of the FS is not enough to be manifested as SHE or AHE. The anomalous contribution to the Hall effect is related to discontinuity of the band and generation of quasiparticles to resolve it, which results into self-intersection of the FS orbit. The orbits passing the hyperbolic point are self-intersecting and can be:

- locally closed

- locally open and globally closed

- locally open and globally open.

The locally open and globally open class result in QHE. Locally open and globally closed orbits are a signature of AHE/SHE as they are related to the flag feature discussed in the previous chapter. The quasiparticles, however, are considered only around the Dirac point and thus the locally closed self-intersection orbits primarily contribute to the for AHE/SHE. However not only Dirac quasiparticles can be generated as it's illustrated in the figure 6.4. Around the singular point of a self-intersecting orbit, the deformation of this singular point can give information about form of the function $\varepsilon(k_i, k_j)$. If we consider k_j as a parameter then in the case of locally closed self-intersecting orbits the function $\varepsilon(k_i)$ is

- not continuous in case of Dirac degeneracy

- order of k_i^3 or more in other cases [87]

In the second case the independent electrons approximation is also not valid (the condition off constant effective mass fails) then this type of orbits also involves quasiparticle genesis and thus contribution to AHE/SHE.

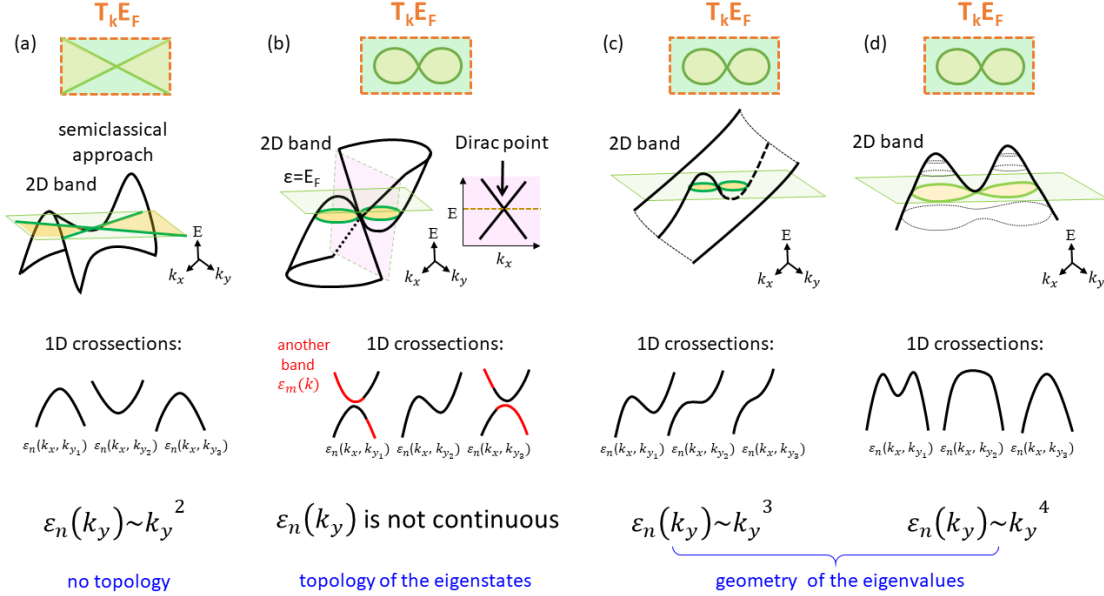


Figure 6.4: Deformation of singularity for a hyperbolic point on the Fermi surface.

To explore this further, we plot the distribution of hyperbolic regions on the FS for a few well known AHE/SHE compounds by carrying out the Gaussian curvature evaluation for every point on the k -mesh. The FS of Fe (figure 6.5), well known for its large intrinsic AHE of $1000 \frac{\hbar}{e}(\Omega cm)^{-1}$ (experimentally determined, [53]), clearly shows a preponderance of hyperbolic points compared with non-hyperbolic points comprising its FS. There is also a clear majority of negatively contributing hyperbolic points compared with positively contributing hyperbolic points (decided by the sign of the local curvature of the electronic band at the Brillouin zone boundary (BZB)). Co_2FeSi , another known AHE compound, but with a much lower experimentally measured intrinsic AHE ($200 \frac{\hbar}{e}(\Omega cm)^{-1}$) [58], also has many hyperbolic points comprising its FS, but is highly compensated: positive and negative contributions are nearly equal. In analogy to Berry curvature compensation, explained in the work [8], oppositely signed regions

contribute with opposite sign to the AHE, thus for Fe the large magnitude of AHE can be the result of an uncompensated hyperbolic FS. Also in figure 6.6, the FS of Pt, having SHC around $2000 \frac{\hbar}{e} (\Omega \cdot cm)^{-1}$, clearly shows a majority of hyperbolic points, whereas TaGa₃, with much lower SHC, has a much lower percentage of hyperbolic points comprising its FS.

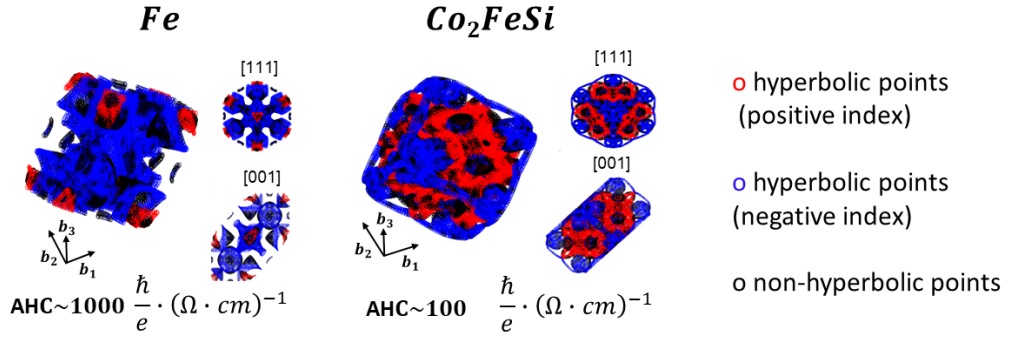


Figure 6.5: Schematic distribution of the hyperbolic and non-hyperbolic regions of the Fermi surface in the reciprocal unit cell for the AHE compounds of varying magnitude.

It is also important to consider the case where $T_K E_F$ is not exactly parallel but instead *tilted with respect to the AHE plane*; the tangent plane will still have similar behavior as described above, but the magnitude of the v_F^{xy} should now be proportional to the angle ϕ between $T_K E_F$ and AHE plane. Then to estimate the contribution of the hyperbolic points we need to consider the projection of the unit vector of the tangent plane (vector e in the plane $T_K E_F$, figure 6.3) in the direction of the expected AHE current in the AHE plane (F_{Hall}) as shown in figure 6.7.

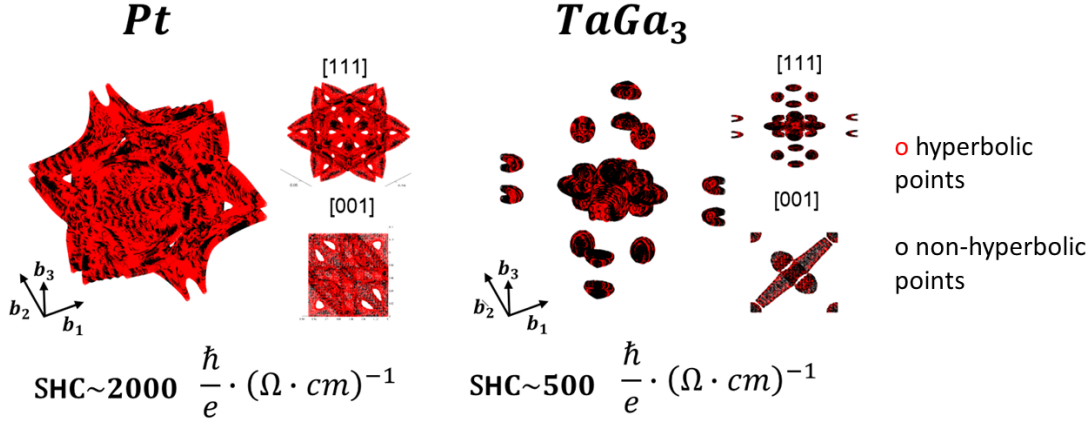


Figure 6.6: Schematic distribution of the hyperbolic and non-hyperbolic regions of the Fermi surface in the reciprocal unit cell for the SHE compounds of varying magnitude.

6.4 H-index for the Fermi surface showing fundamental correlations with AHC and SHC

To more rigorously quantify the correlation between hyperbolic points on the FS and AHE/SHE we introduce the index of “hyperbolicity” of the FS, which we denote by \mathbb{H}_F and define as the following:

$$\mathbb{H}_F = \frac{\sum_{FS} I_n |F_{Hall}(K \text{ is hyperbolic})|}{\sum_{FS} |F_{Hall}(K \text{ is arbitrary})|}, \quad (6.8)$$

where F_{Hall} , is orthogonal to the applied current, and I_n is the sign of the $\partial^2 \epsilon_n / \partial^2 k$ at the BZ boundary in the Hall current direction (see figure 7.16 in the supplementary information for the details). As defined, \mathbb{H}_F can have a maximum of “1” which means that the entire FS would be hyperbolic, except for the points where the tangent plane is orthogonal to the AHE plane.

We performed unperturbed DFT calculations of 16 compounds for which intrinsic AHC values were rigorously experimentally determined[52, 53, 54, 55, 56, 57, 58, 59, 60], covering a variety of structural families (perovskites, Heuslars, Kagome lattices, FCC lattices, etc.) and topological classes (Dirac/Weyl/Trivial metals and semimetals). We compared those experimental AHC

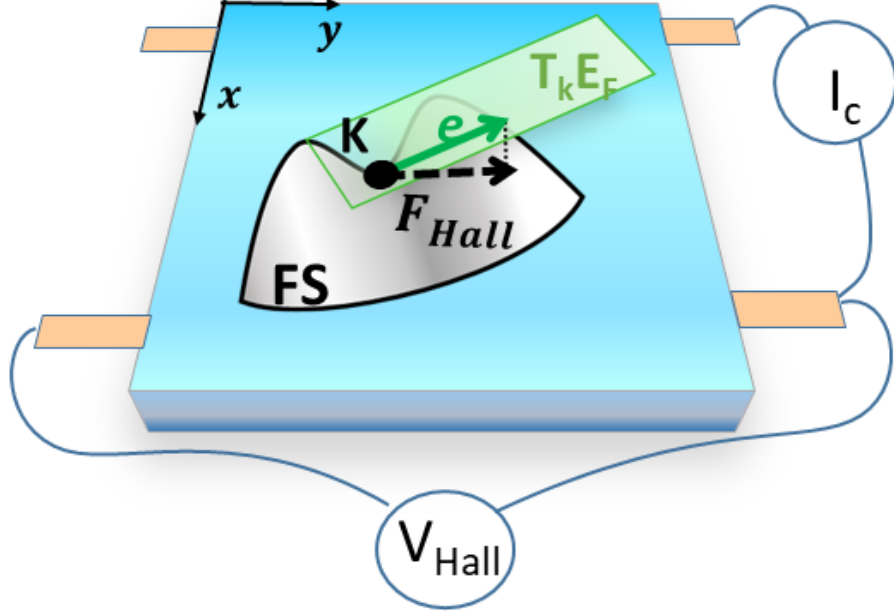


Figure 6.7: Definition of the vector F_{Hall} as a projection of unit vector from the FS tangent plane.

values to our calculated \mathbb{H}_F (taking care to align the directions of calculation with the directions of measurement for each material in the various experiments). Since, for now, the \mathbb{H}_F parameter is defined for a 2D conductance, we made a comparison of the calculated \mathbb{H}_F with the measured values for thin films or layered structures where the contribution of the third dimension to the total effect is relatively weak.

The result, shown in figure 6.8, shows an extraordinary linear correlation of the hyperbolicity of the FS with the experimentally measured AHC values with an R^2 value of 0.97, for the compounds, regardless of structural family or topological class. Importantly, we also plot the experimentally measured intrinsic AHC values versus the calculated AHC values using the Kubo formalism (based on Berry curvature [52, 56, 55, 57, 58, 9, 59]) for the same compounds (Figure 3d). The R^2 drops down to only 0.52, with a few exceptionally inaccurate cases like Co_2MnAl or Ni, where the error is large and the reason is still under investigation [88]. Even without

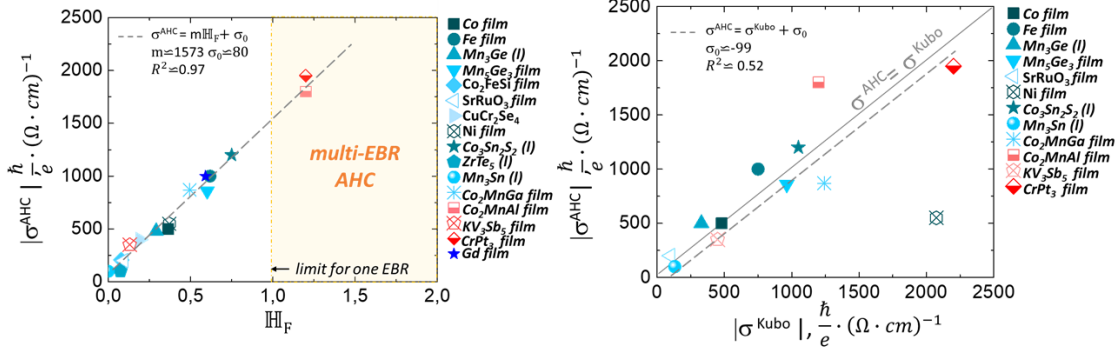


Figure 6.8: Correlation graph left: *experimentally* determined intrinsic AHC vs \mathbb{H}_F for various materials ((l) identifies layered structures). Right: *experimentally* determined intrinsic AHC vs predicted values of AHC via the Kubo formalism.

taking those two compounds into account, the R^2 from the Kubo calculated AHCs only rises to 0.87; significantly worse than the \mathbb{H}_F -dependence. We made a similar calculation for SHE compounds, but due to a paucity of experimental data, we are forced to plot the comparison of the Kubo predicted SHC values for Pt, W_3W [42, 64] and TaGa_3 at different E_F -levels against their corresponding \mathbb{H}_F -values in the figure 6.9. This graph also shows a strong correlation of the hyperbolicity with the Kubo calculated SHCs with an R^2 of about 0.95, implying that the Kubo approach and the hyperbolicity match well in the case of highly uncompensated FS's [49]; a direction of future investigation.

6.5 Geometrical treatment for breaking limit of anomalous Hall conductivity: example of CrPt_3

From the correlation in figure 6.8, it can be seen that in the limit of $\mathbb{H}_F = 1$, the intrinsic AHC is expected to reach a maximum value of $1570 \frac{\hbar}{e} (\Omega \text{cm})^{-1}$. However, there are two compounds (Co_2MnAl and CrPt_3) that have \mathbb{H}_F and intrinsic AHCs greater than this maximum. While

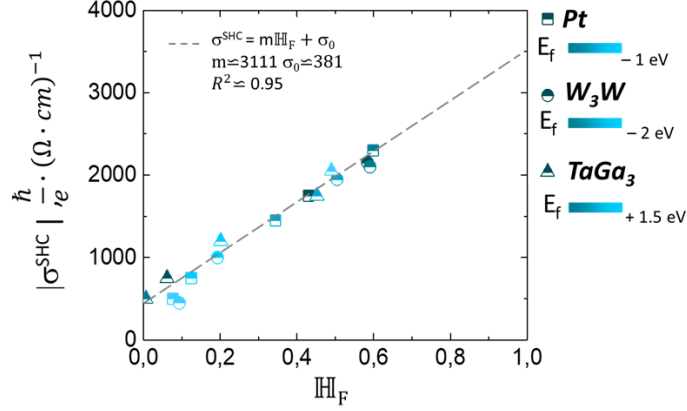


Figure 6.9: Correlation graph of the predicted SHC values via the Kubo formalism vs \mathbb{H}_F , as defined in the text.

at first this appears to be an inconsistency, the limit on \mathbb{H}_F can be broken if we take into account the EBR (elementary band representation) for the bands forming FS. Recently it was shown that all bands can be grouped into sets that correspond to distinct EBRs; topological semimetal behavior can be understood as a property of a partially occupied set of such bands (see supplement sections 1 and 2 for more on manifolds and EBRs). Also, the non-quantized contribution to AHE, as shown by Haldane et al[43], is expected to be a pure Fermi surface property. Combining these two ideas, a part of the FS that is comprised of multiple pockets created by the bands belonging to a single EBR, can be considered distinctly from *another part* of the FS similarly corresponding to the *bands from another EBR*.

In the common case where there is a continuous gap disconnecting sets of bands contributing to the FS, \mathbb{H}_F can be calculated separately using formula 6.8 for parts of the surfaces arising from distinct sets of bands (bands with differing EBRs), essentially dividing the manifold into submanifolds by EBR, and subsequently summed together in order to characterize the entire FS. This is exactly the case for Co_2MnAl , CrPt_3 and KV_3Sb_5 . For the case of KV_3Sb_5 , it can be seen that the contributions of the distinct EBRs are not cooperative, resulting in a relatively low \mathbb{H}_F of 0.14. However, for Co_2MnAl and CrPt_3 , both have cooperative contributions and

correspondingly have \mathbb{H}_F values larger than 1 as well as AHC values larger than $1570 \frac{\hbar}{e}(\Omega cm)^{-1}$; but they still correlate extremely well with the overall trend in Figure 6.8. Figure 6.10 showcases the detailed bandstructure for $CrPt_3$ with each distinct set of bands colored (blue and yellow) with the continuous gap shaded in gray. The insets clarify the almost-degeneracies near Gamma which are actually gapped. In the Berry curvature approach, the states from the different EBRs are mixed in the total calculation in the Kubo formula. Figure 6.10 shows the energy dependent AHC calculated from the Kubo formalism as well as the energy dependent AHC (using the AHC vs \mathbb{H}_F correlation $\sigma = m\mathbb{H}_F + \sigma_0$ to convert \mathbb{H}_F to a numerical AHC value). The results from the two methods are qualitatively similar, but the \mathbb{H}_F result has a slightly better quantitative match to experiment.

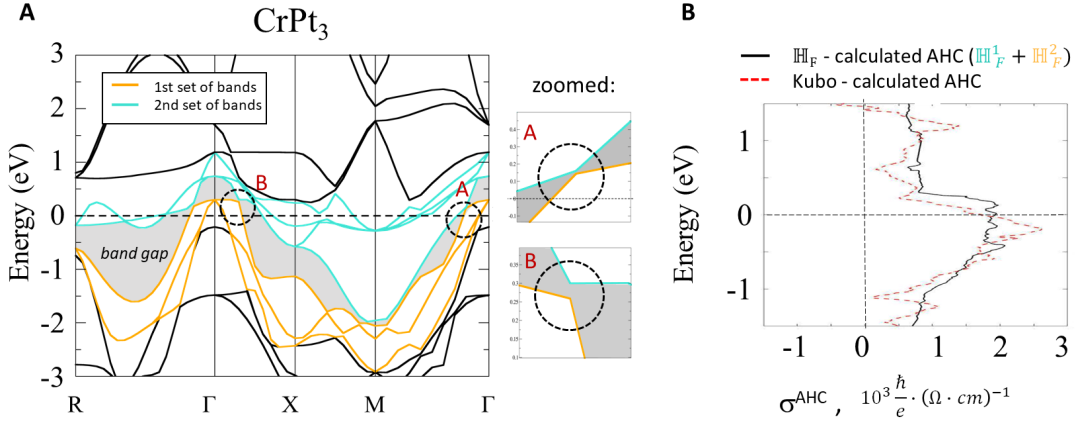


Figure 6.10: (a) Bandstructure of $CrPt_3$. Blue and yellow colors represent two topologically disconnected (having different EBRs) sets of bands crossing the Fermi level. These sets are disconnected by the continuous gap present between them; i.e. true semimetallic behavior. (b) Graph of energy resolved AHC predicted in two different ways: red dashed line is the Kubo based prediction, black dashed line stems from the linear correlation between H_F and AHC calculated separately for FS contributions from each set of bands, then summed together for total \mathbb{H}_F .

Why do the FSGE and \mathbb{H}_F method appear to fare better than the Kubo approach for these materials and properties? This is a wide area of future investigation, however, there are at least four important considerations we elaborate on here. Firstly, the Kubo formalism looks at the Berry curvature in a point-wise fashion without consideration of their connections to each other, and a fictitious broadening parameter that does not fully capture finite temperature effects to

the electronic structure. Looking at independent points in momentum space means that if a particular point of importance is missed (because of, for example, a very sharp feature or a too low resolution k-mesh grid), its entire contribution is missed and the calculation can become inaccurate. This is fundamentally different than the *path-wise* FSGE method which looks at points and their connection to each other because it is approximating trajectories. This is likely related to the \mathbb{H}_F plateaus (see figure 7.17 , supplementary information) at relatively sparse K-meshes of $\approx 30 \times 30 \times 30$, unlike the typical $>150 \times 150 \times 150$ k-mesh grids used in the Kubo analysis (where the k-mesh must also increase for tightening the broadening factor). Secondly, the \mathbb{H}_F calculations rely purely on the first principles calculation of the Fermi Surface and not an interpolated/tight-binding representation of the first principles calculation as in Kubo. This (i) eliminates the need for Wannier/tight-binding Hamiltonians which loses the gauge invariance in the convergence process, and (ii) \mathbb{H}_F calculations are not restrained by the quality of the Wannier fit which are localized functions that will always have trouble capturing the completely delocalized topological states present in some systems. Thirdly, a popular approach in the modern application of the Kubo method, particularly to deal with the irregular points that are often major sources of Berry curvature, as earlier explained, is to use an adaptive k-mesh. These are locally enlarged around irregular points which have to be identified *a priori*. Incomplete identification of all irregular points will again lead to missing contributions to the Berry curvature and make the final AHC calculation inaccurate. In the FSGE method, there is no *a priori* identification followed by piecewise treatment required, as it is similar to a conjugate gradient method, and doesn't require any such k-meshes. Finally, as mentioned previously, the Kubo formalism looks at two-band transitions, not multiband transitions, meaning it ignores higher order transitions that can also result in anomalous transport contribution. The FSGE method inherently looks at *n-band transitions* since it is a pure Fermi Surface analysis method and the Fermi Surface (and its features) is made up of any number of bands crossing E_F .

When compared with the current Berry curvature driven method for AHE/SHE prediction via the Kubo formalism, the \mathbb{H}_F index is also, computationally, a much simpler metric as it requires just basic DFT calculation without Wannier projection, and thus can be carried out at a significant reduction in time and cost. Importantly, this analysis method can easily be fully automated and implemented into material databases, and can enable artificial intelligence and machine learning based searches of large repositories of compounds for materials with desirable traits for technological applications. For now the \mathbb{H}_F index is still a relatively rough estimation;

it does not separate the effect of locally open orbits vs irregular orbits around hyperbolic points, shown in figure 6.4 and is limited to the cases of 2D AHE/SHEs. However, the numerical correlation of the AHE/SHE with \mathbb{H}_F of $R^2 = 0.97$ proves that the concept of using the geometric classification of electronic structure manifolds is not just a "blue-sky" theoretical research effort; it has immediate applications to outstanding questions in condensed matter physics. The results may extend to the anomalous Nernst effect and the non-linear Hall effect as well, due to their similarity in origin to the AHE/SHE.

Chapter 7

Towards geometrical classes of the bandstructures

As was shown in the previous chapter, the FS can be thought as a continuous set of points, and the operations of differentiation and integration on the FS in the semiclassical way, can be treated via the tangent bundle construction. In this chapter, extending this idea, a continuity between energies in the Hamiltonian's spectrum can be introduced. This can lead to geometrical re-understanding of the semiclassical transport equation, via re-interpretation of differentiation used in it.

Similar to the earlier division of $\Phi_{crystal}$ into open subsets, the energy spectrum can also be divided into open subsets in the following way:

$$U_i^\epsilon(\epsilon_0) = \{\epsilon_i(k) \text{ such that } |\epsilon_0 - \epsilon_i(k)| < k_b T\}. \quad (7.1)$$

Thus, a topology is introduced on $\epsilon_i(k)$ from the quasiparticle approach to the electron transport in crystals: as was shown in chapter 3, the interaction between electrons with different momenta allows the use of a collective quasiparticle, which is considered to behave like a single particle [24]. This can change the point of view on the bandstructure, as is schematically shown in figure 7.1.

This topological space can be turned into a manifold if we equip it with the following maps:

$$f_i^\epsilon(\epsilon_0(k)) = \langle \phi_i(x, k), \nabla_k H, \phi_i^\dagger(x, k) \rangle. \quad (7.2)$$

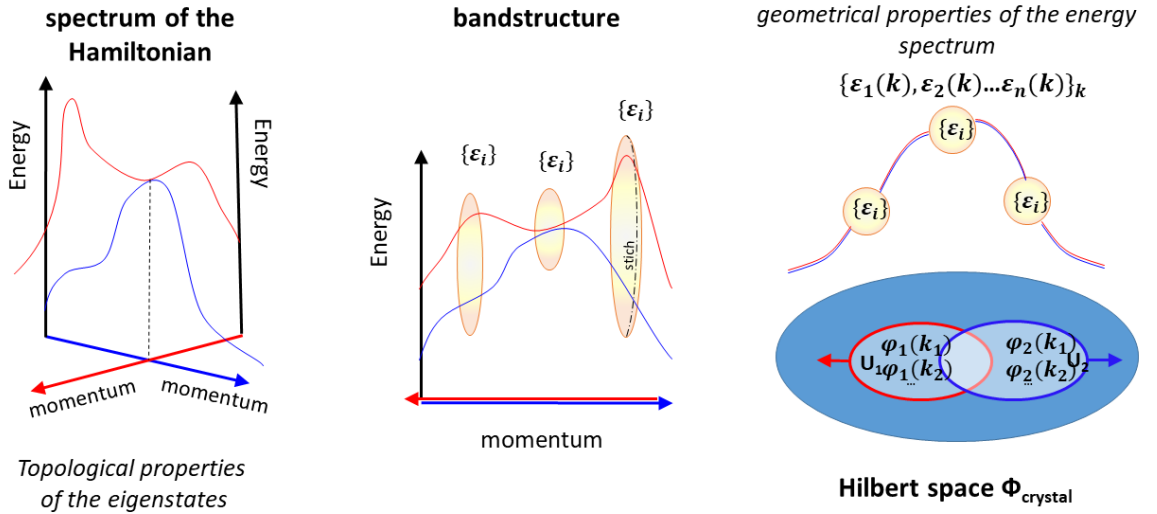


Figure 7.1: Schematic representation of topology on the Hamiltonian's domain and spectrum of the corresponding Hamiltonian.

Then the linear spaces, in this case, are \mathbb{R}^3 and the spectrum, ε , of the Hamiltonian can be thought of as a 3D energy manifold, E .

Since an electron can have two possible spin orientations, the energy manifold can naturally be oriented according to the spin orientation. However, this manifold is not compact; due to the Pauli exclusion principle, two electrons (spinless) from different bands $\varepsilon_i(k)$ and $\varepsilon_j(k)$ with the same momentum k cannot have the same energy. That implies that E does not satisfy conditions of the geometrization conjecture.

In order to overcome this, we can split the energy manifold, E , into compact submanifolds E_i of the i_{th} band. Then each submanifold is closed in the above topology and has no boundaries since the energy is defined, without restriction, for all possible momenta in a band. Thus an electronic band can be *re-thought of as a manifold (rather than a function, as has always be done) and the methods of modern geometry applied, including classification into one the 8 Thurston geometries.* [89]

Most real materials have more symmetries, in addition to translation, and thus the eigenstates of their Hamiltonians may differ from only the Bloch wavefunction $\phi_n(x, k)$. How-

ever, it was shown that these eigenstates can be obtained from the *group* of Bloch states $\phi_n(x, k), \phi_{n+1}(x, k) \dots \phi_{n+k}(x, k)$ (the details of this process and derivation can be found in the work of Bradlyn [12]). The collective eigenstate is known as the Elementary Band Representation (EBR). Now for $\Phi_{crystal}$, the EBRs are the subspaces that play the role of the coordinate axes for the Hilbert space, instead of $\phi_i(x, k)$ for the Bloch wavefunctions. Schematically this is shown in figure 7.2; in the top row, the individual Bloch wavefunctions of $\Phi_{crystal}$ result in individual bands in the E vs k spectrum. In the bottom row, due to symmetry demanded degeneracies, the Bloch wavefunctions can be grouped into different EBRs depending on those degeneracies.

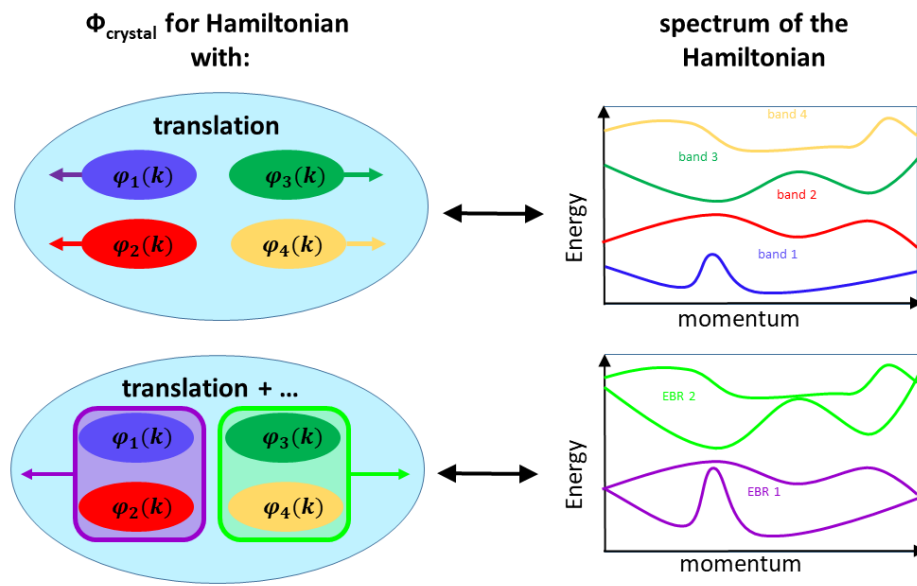


Figure 7.2: Relation between the structure of Hamiltonian's domain and the spectrum of Hamiltonian (a.k.a. bandstructure) and $\Phi_{crystal}$ for Bloch bands and EBR.

If the Fermi level lays within the energy window of one EBR, then the compound is defined to be a topological semimetal and will have nontrivial transport properties resulting from those bands (which may or may not be measurable depending on a variety of real-life factors). At the crossing point of the bands, the Fermi velocity is not well defined in the typical understanding of the derivative of $\epsilon(k)$ over reciprocal space. However this situation can be handled in the manifold construction (schematically shown in the figure 7.3).

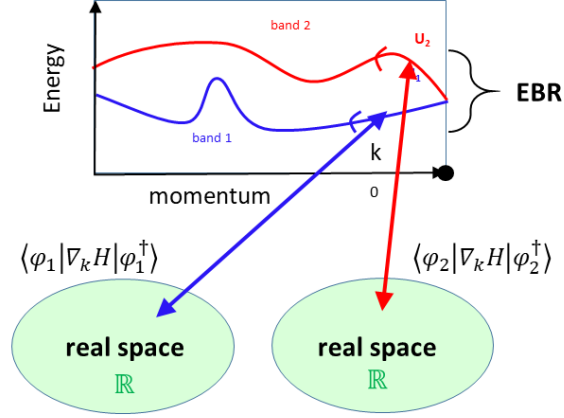


Figure 7.3: Construction of an atlas of maps f_i on the bandstructure (for 1D bandstructure).

An EBR must have at least one momentum k where different Bloch states are degenerate [12]. Assuming the EBR consists of two bands corresponding to the eigenstates $\phi_1(x, k)$ and $\phi_2(x, k)$, and that they intersect at point k_0 , then around k_0 the EBR can be split into two subsets, U_1 and U_2 corresponding two different bands containing the point $\epsilon(k_0)$. Then for U_1 we can define the homeomorphism similar as in the equation (4), but as the action of the Hamiltonian on $\phi_1(x, k)$ and for U_2 as the action on $\phi_2(x, k)$. This idea can be extended for any n-fold degenerate point within an EBR containing n-bands. Then a full analysis of the dynamics of an electron belonging to an EBR can be carried out using a variety of geometrical tools developed for manifolds (like geodesic or Ricci flow equations etc.) instead of the typical group velocity concept. However, a full investigation of these concepts and connections is beyond scope of this thesis and is a promising area of future work.

As it was shown an electronic energy band or bandset from one EBR is, fundamentally, a 3 dimensional orientable, closed manifold, over the reciprocal (k) space. For these types of manifolds, the geometrical structures which are possible to exist were first theorized by Thurston[89] and proved recently by Perelman[90]. This famously led to the proof of the Poincare Conjecture

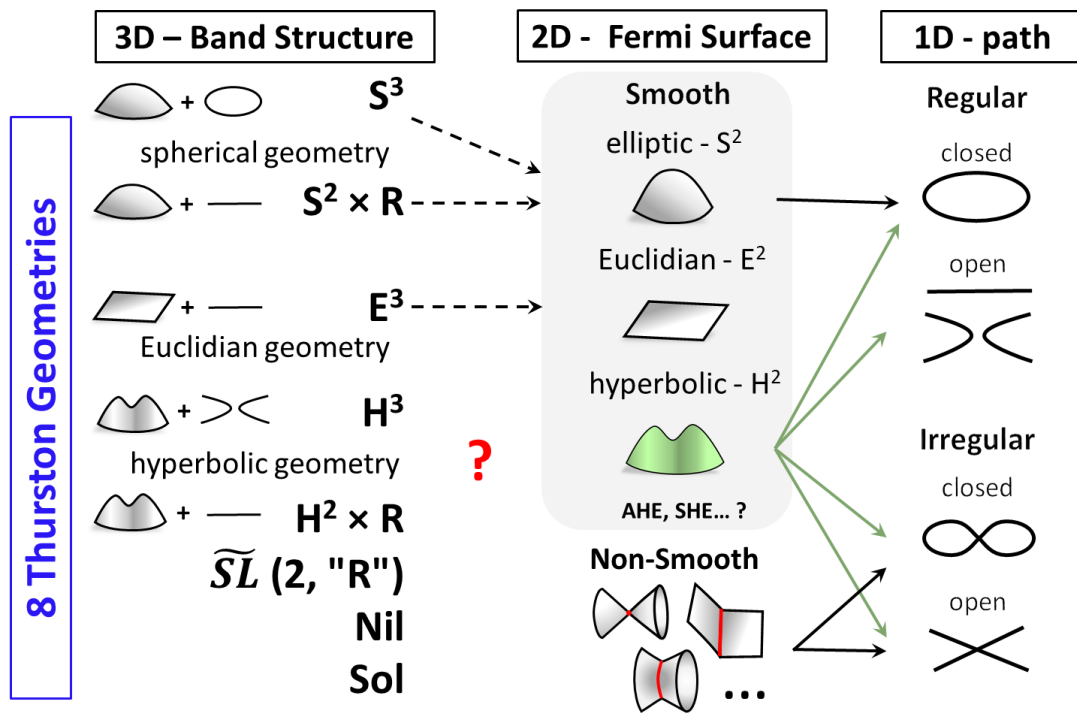


Figure 7.4: Diagram of the classes of local geometries in different dimensions. The left column shows the 8 Thurston geometries for 3D manifolds, like band structures, presented schematically and with their symbols of geometry. The middle column shows the three smooth (and non-smooth) classes for 2D manifolds like Fermi surfaces. The right hand column shows the classifications of 1D paths, like Fermi surface paths, resulting from further reduction of dimension. Arrows illustrate the connection between certain higher dimension geometrical classes and their lower dimensional counterparts; green arrows showcase how hyperbolic 2D manifolds can result in all types of 1D paths.

(one of Millennium Prize Problems and one of the most important questions in topology) where Perelman combined ideas from Hamilton and Thurston and used the entropy of the Ricci flow on 3D manifolds. According to his work, a 3D manifold, like an electronic energy band, can be split into regions, where each region can be classified into one of the 8 Thurston geometrical classes (schematically described in figure 7.4). Since the electronic structure fundamentally governs *intrinsic* (not scattering driven) electron transport phenomena in crystalline materials, the geometrical classes (or combinations of them as well as the boundaries between them) must also correspond to intrinsic transport phenomena. Similar to how topology has been used to

classify band structures and relate them to transport phenomena, a *geometrical* understanding of band structures, with classification and relation to transport, can be carried out. In doing so, one of the most fundamental results in modern mathematics may be found to have a direct practical application – not only to condensed matter physics and material science, but also to device technologies. However, developing the complete theory of Electronic Structure Geometry, with transport equations derived from geodesic flow analysis, is highly challenging and beyond the authors’ current abilities and the scope of this work.

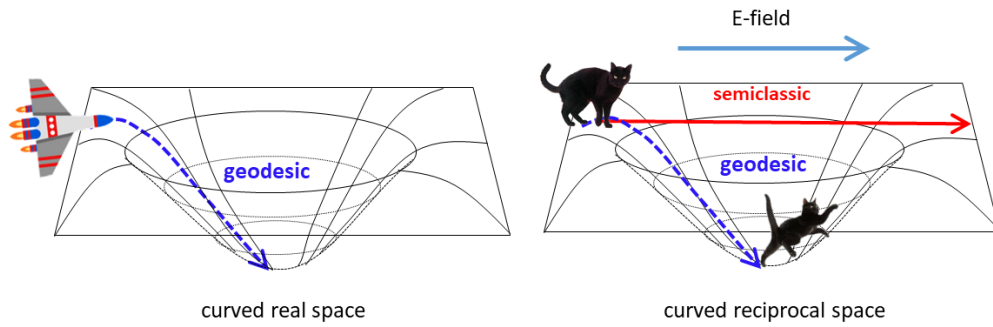


Figure 7.5: Visual analogy between curved by mass real space and curved by the crystal potential momentum space.

s

The concepts outlined here may alter the current paradigm of understanding the non-trivial transport regimes (like AHE/SHE) moving it to include geometrical properties of the band structure and FS, rather than just topological properties of the eigenstates of the Hamiltonian. This way semi-classical transport equations can be developed using the idea of a quasi-particle moving along a trajectory described by the geodesic equation of the curved energy-momentum manifold (a Riemannian manifold), rather than a free particle moving with group velocity v_F , *in direct analogy* to the theory of general relativity for a traveler moving along the geodesics of a

curved space-time manifold (also a Riemannian manifold where Ricci curvature is used to relate the space-time geometry to the stress-energy tensor). See figure 7.5 for a visual demonstration of this analogy. Describing the smooth deformation of the Riemannian metric for the manifold (e.g. geodesic flow) is one route to connecting the Thurston geometries to quasi-particle dynamics and transport phenomena. An immediate direction of future work is to attempt re-conceptualize a particle's spin as a geometrical construction of symplectic form on the energy-momentum manifold, which is a natural property of any odd dimensional manifolds. This may lead to the fundamental understanding of other exotic effects, but is beyond the scope of this work, which is introducing the use of modern geometrical methods to the electronic structure theory. Some of the important open questions stemming from these ideas are: can the other geometrical invariants aside from the Gaussian curvature be applied to identification of the transport properties in crystals? Can a full derivation of the FSGE on quasi-particles in reciprocal space be translated into real-space electron transport equations through the use of Born reciprocity relations? Are there other obvious correlations between geometrical classes of FS regions and other non-fermi liquid transport phenomena (e.g. Euclidean and, say, electron correlation)? How do boundaries between FS regions interact and do they result into effectively turbulent quasi-particle dynamics on an energy-momentum manifold, and in what limits? What are the consequences of this in real-space?

Summary

In summary, motivated by Perlman, Hamilton, and Thurston's works, we have introduced the general concept of using modern *geometry* of multi-dimensional manifolds to characterize electronic structures and predict non-trivial transport phenomena. Using the current Berry curvature based approach, the anti-crossings in bandstructure were shown to result in large SHE on the examples of A15 compounds. The anti-crossings at the Fermi level were analyzed in the context of the Fermi surface's degeneracies and non-smooth orbits leading to the Fermi Surface Geometry Effect, through the use of tangent bundles and Gaussian curvature, that relates the hyperbolicity of the Fermi surface with anomalous and spin Hall effects. This concept has been applied to develop an index, \mathbb{H}_F , for describing the "hyperbolicity" of the FS and showed a universal correlation ($R^2 = 0.97$) with experimentally measured intrinsic AHE values for 16 different compounds spanning a wide variety of crystal, chemical, and electronic structure families. An apparent maximum value, at $\mathbb{H}_F = 1$, of $1570 \frac{\hbar}{e}(\Omega cm)^{-1}$ was determined for materials with an FS created by bands belonging to a single EBR; materials with multi-EBR FS's can, and do, break this limit as evidenced by CrPt₃ and Co₂MnAl. Use of the \mathbb{H}_F index allows direct calculation of the AHE/SHE at a much lower computational cost, than current methods by eliminating the need for Wannier projection and can be implemented with existing DFT methods and databases. This work highlights the importance of, and opportunities laying ahead for, developing a complete theory of *geometrical understanding* of electronic structure manifolds beginning with Fermi surfaces. Also, these ideas can be extended to bosonic (e.g. magnonic) band structures as well. In analogy to the broad impact that topological understanding of these structures had, a theory of the Fermi Surface Geometry Effect and eventual extension to other dimensional manifolds, will lead to a deeper understanding of at least electron transport and have far reaching consequences in condensed matter physics.

Summary

Supplementary information

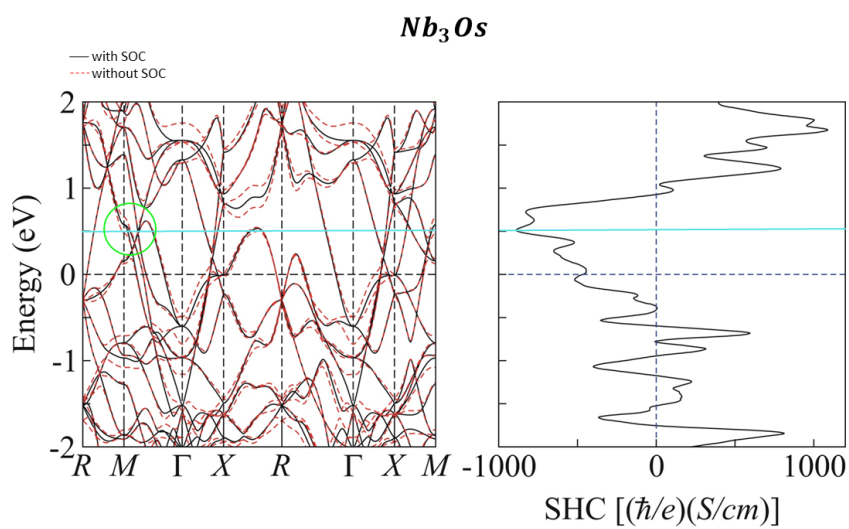


Figure 7.6: Electronic structure without and with SOC included as well as the SHC vs energy plot for Nb_3Os

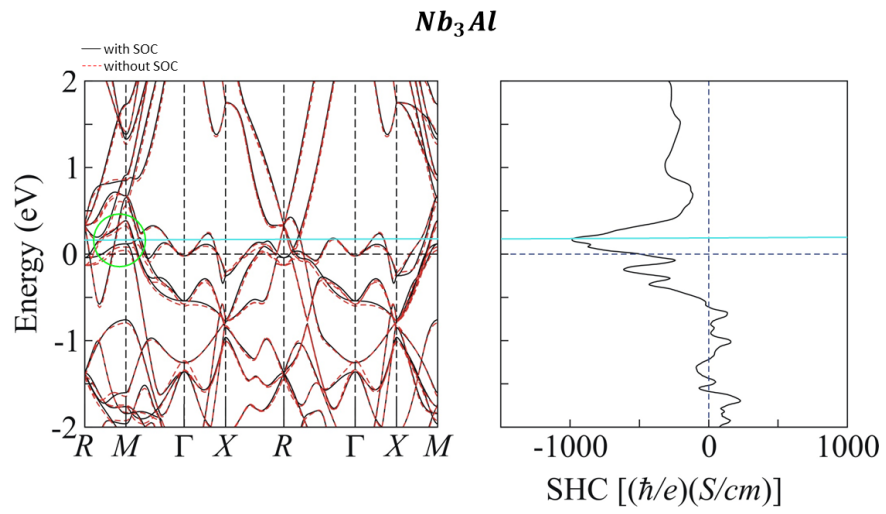


Figure 7.7: Electronic structure without and with SOC included as well as the SHC vs energy plot for Nb_3Al

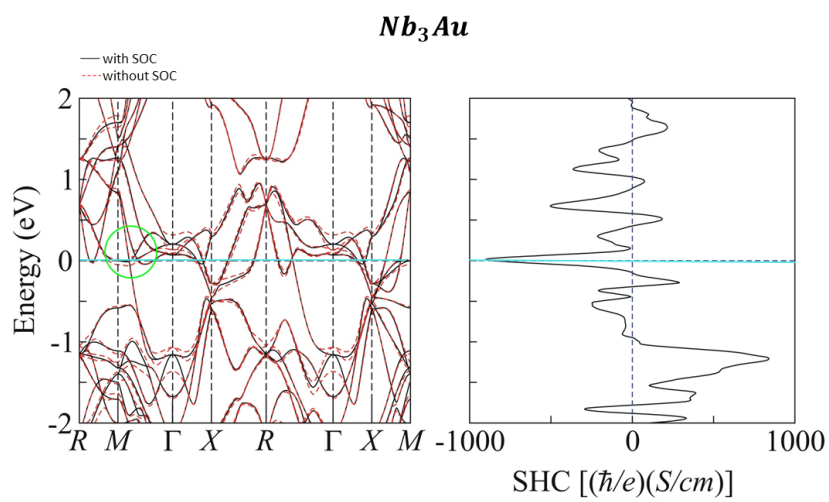


Figure 7.8: Electronic structure without and with SOC included as well as the SHC vs energy plot for Nb_3Au

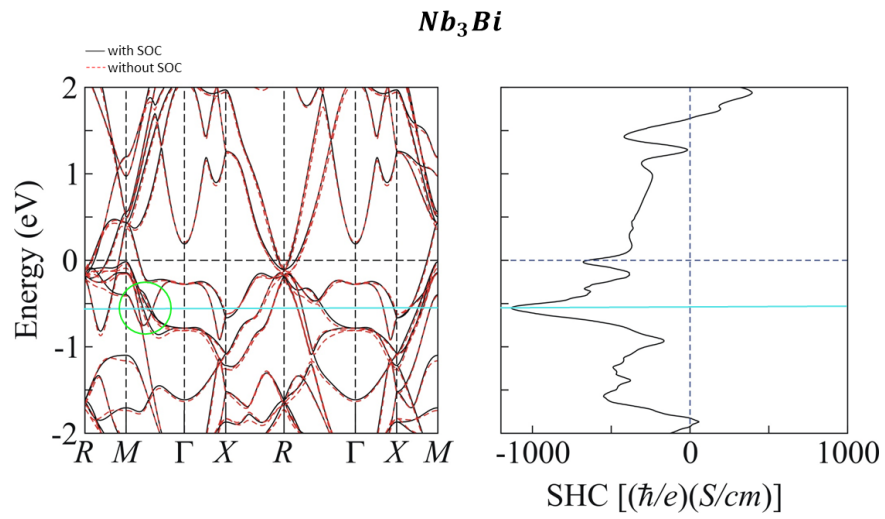


Figure 7.9: Electronic structure without and with SOC included as well as the SHC vs energy plot for Nb₃Bi

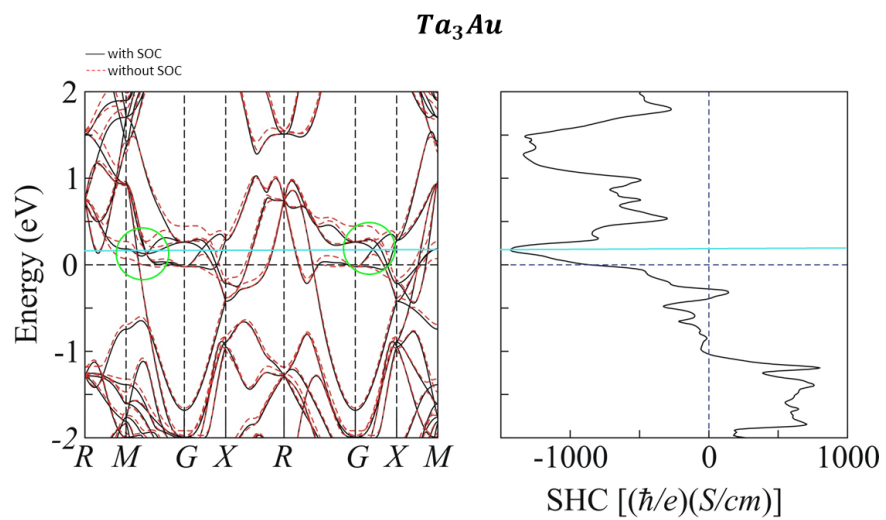


Figure 7.10: Electronic structure without and with SOC included as well as the SHC vs energy plot for Ta₃Au

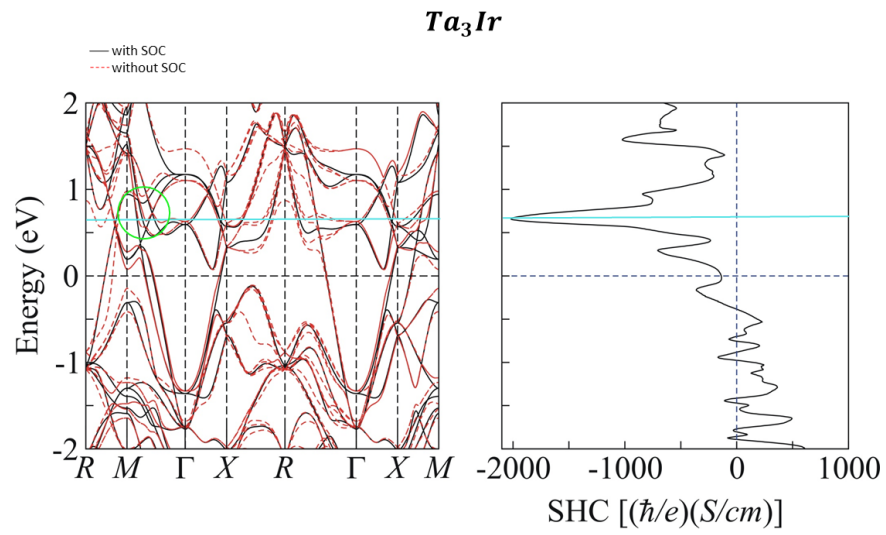


Figure 7.11: Electronic structure without and with SOC included as well as the SHC vs energy plot for Ta₃Ir

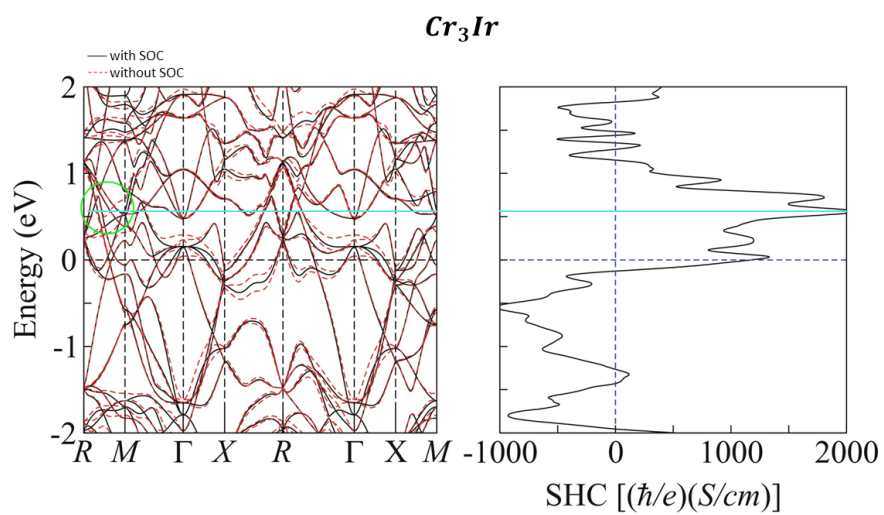


Figure 7.12: Electronic structure without and with SOC included as well as the SHC vs energy plot for Cr_3Ir

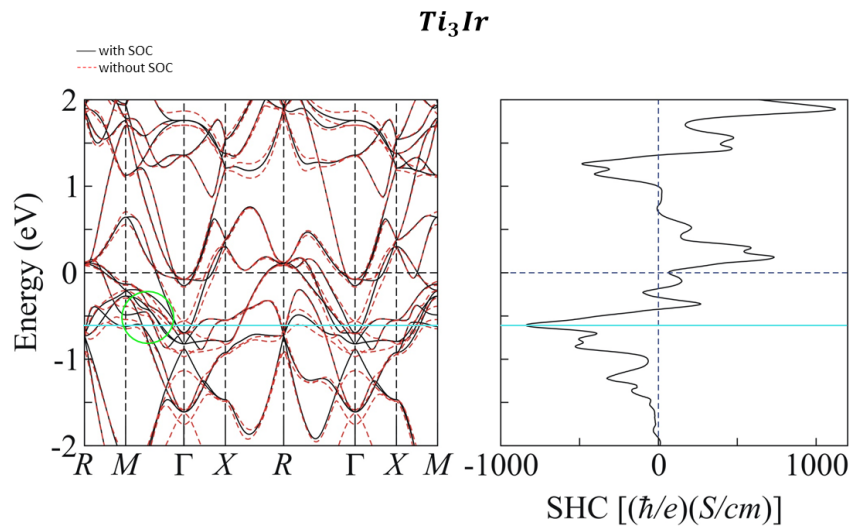


Figure 7.13: Electronic structure without and with SOC included as well as the SHC vs energy plot for Ti_3Ir

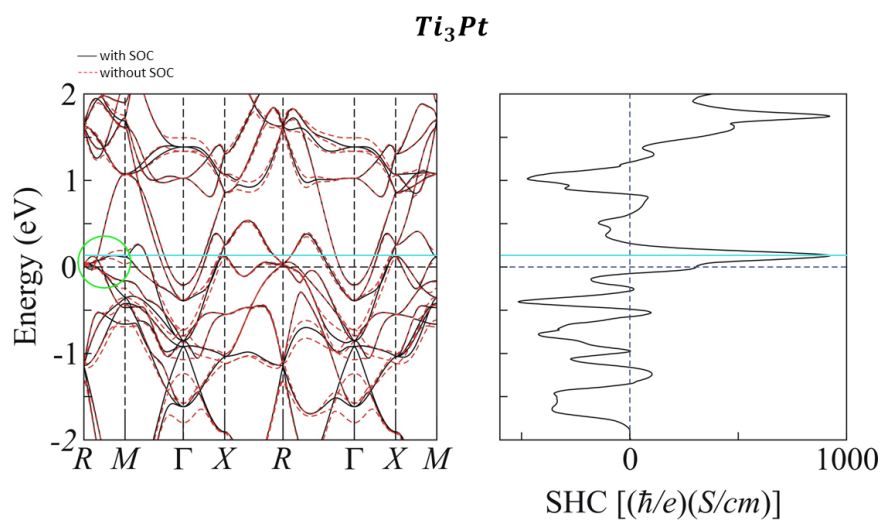


Figure 7.14: Electronic structure without and with SOC included as well as the SHC vs energy plot for Ti_3Pt

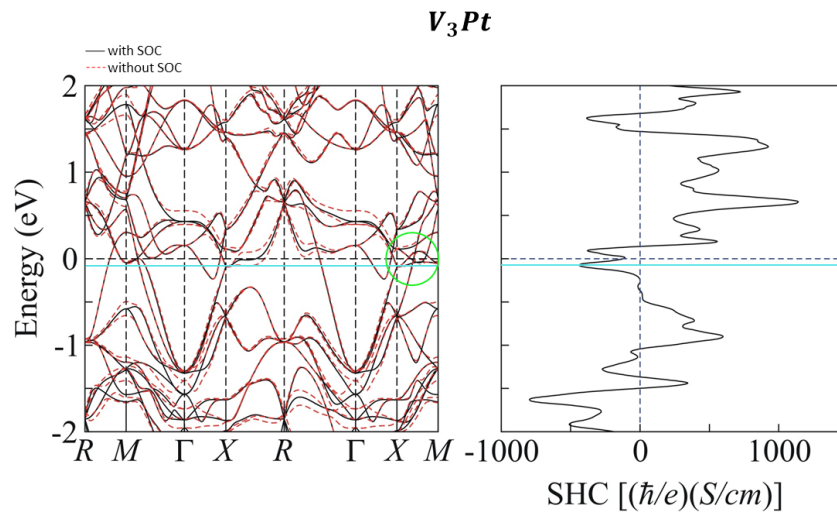


Figure 7.15: Electronic structure without and with SOC included as well as the SHC vs energy plot for V_3Pt

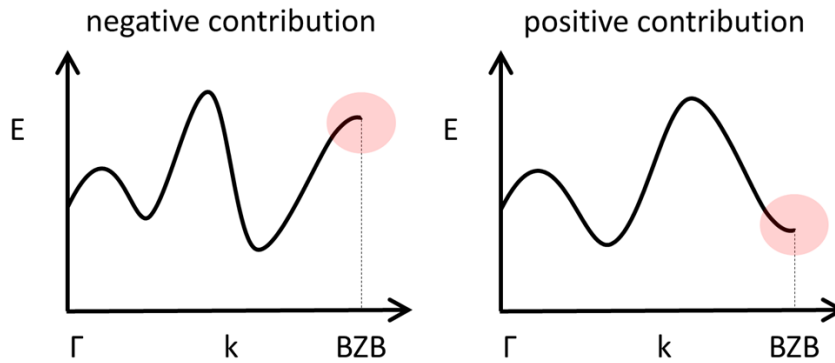


Figure 7.16: Schematic plot of negatively and positively contributing bands to the \mathbb{H}_F . The red circle highlights the band habit at the BZB (Brillouin zone boundary) where the sign of the curvature (second derivative of the band) is used for identification of the contribution type. A consistent choice of BZB is used for analysis of all bands.

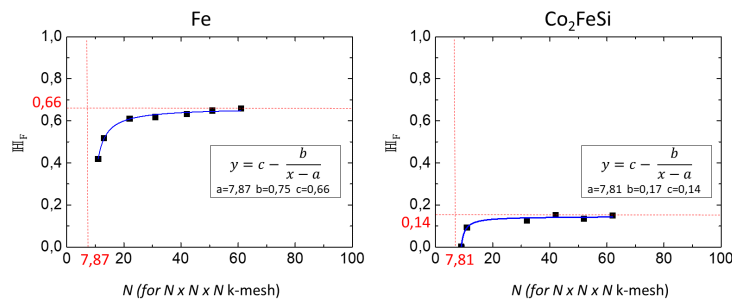


Figure 7.17: \mathbb{H}_F dependence of k-mesh density for Fe and Co_2FeSi . y-axis is the calculated total \mathbb{H}_F , and the x-axis is k-points cubed.

Supplementary information

Bibliography

- [1] Haijun Zhang, Chao-Xing Liu, Xiao-Liang Qi, Xi Dai, Zhong Fang, and Shou-Cheng Zhang. Topological insulators in Bi_2Se_3 , Bi_2Te_3 and Sb_2Te_3 with a single Dirac cone on the surface. *Nature Physics*, 5(6):438–442, 2009.
- [2] Markus König, Steffen Wiedmann, Christoph Brune, Andreas Roth, Hartmut Buhmann, Laurens W. Molenkamp, Xiao-Liang Qi, and Shou-Cheng Zhang. Quantum Spin Hall Insulator State in HgTe Quantum Wells. *Science*, 318(5851):766–770, 2007.
- [3] H Cercellier, C Monney, F Clerc, C Battaglia, L Despont, MG Garnier, H Beck, P Aebi, L Patthey, H Berger, et al. Evidence for an excitonic insulator phase in 1T-TiSe₂. *Physical review letters*, 99(14):146403, 2007.
- [4] Hideo Ohno, Mark D Stiles, and Bernard Dieny. Spintronics. *Proceedings of the IEEE. Institute of Electrical and Electronics Engineers*, 104(10):1782, 2016.
- [5] Albert Fert. Nobel lecture: Origin, development, and future of spintronics. *Rev. Mod. Phys.*, 80:1517–1530, Dec 2008.
- [6] Cheng-Cheng Liu, Wanxiang Feng, and Yugui Yao. Quantum spin Hall effect in silicene and two-dimensional germanium. *Physical review letters*, 107(7):076802, 2011.
- [7] CL Kane and EJ Mele. Quantum spin Hall effect in graphene. *Physical Review Letters*, 95(22):226801, 2005.
- [8] Di Xiao, Ming-Che Chang, and Qian Niu. Berry phase effects on electronic properties. *Rev. Mod. Phys.*, 82(3):1959–2007, July 2010.
- [9] Xinjie Wang, David Vanderbilt, Jonathan R. Yates, and Ivo Souza. Fermi-surface calculation of the anomalous hall conductivity. *Phys. Rev. B*, 76:195109, Nov 2007.

Supplementary information

- [10] Vitaly L. Ginzburg. On superconductivity and superfluidity as well as on the physical minimum at the beginning of the 21st century. *ChemPhysChem*, 5(7):930–945, 2004.
- [11] M. Cyrot. The hubbard hamiltonian. *Physica B+C*, 91:141 – 150, 1977.
- [12] Barry Bradlyn, L. Elcoro, Jennifer Cano, M. G. Vergniory, Zhijun Wang, C. Felser, M. I. Aroyo, and B. Andrei Bernevig. Topological quantum chemistry. *Nature*, 547:298 EP –, Jul 2017. Article.
- [13] C. Kittel. *Introduction to Solid State Physics*. Wiley, 1996.
- [14] R. J. Elliott. Theory of the effect of spin-orbit coupling on magnetic resonance in some semiconductors. *Phys. Rev.*, 96:266–279, Oct 1954.
- [15] L. D. Landau and L. M. Lifshitz. *Quantum Mechanics Non-Relativistic Theory, Third Edition: Volume 3*. Butterworth-Heinemann, 3 edition, January 1981.
- [16] R. Hoffmann. *Solids and surfaces: a chemist's view of bonding in extended structures*. VCH Publishers, 1988.
- [17] Shuo-Ying Yang, Hao Yang, Elena Derunova, Stuart S. P. Parkin, Binghai Yan, and Mazhar N. Ali. Symmetry demanded topological nodal-line materials. *Advances in Physics: X*, 3(1):1414631, 2018.
- [18] Hao Yang, Yan Sun, Yang Zhang, Wu-Jun Shi, Stuart S P Parkin, and Binghai Yan. Topological weyl semimetals in the chiral antiferromagnetic materials mn₃ge and mn₃sn. *New Journal of Physics*, 19(1):015008, jan 2017.
- [19] B.-B. Fu, C.-J. Yi, T.-T. Zhang, M. Caputo, J.-Z. Ma, X. Gao, B. Q. Lv, L.-Y. Kong, Y.-B. Huang, P. Richard, M. Shi, V. N. Strocov, C. Fang, H.-M. Weng, Y.-G. Shi, T. Qian, and H. Ding. Dirac nodal surfaces and nodal lines in zrsis. *Science Advances*, 5(5), 2019.
- [20] W. Kohn and L. J. Sham. Self-consistent equations including exchange and correlation effects. *Phys. Rev.*, 140:A1133–A1138, Nov 1965.
- [21] P. Hohenberg and W. Kohn. Inhomogeneous electron gas. *Phys. Rev.*, 136:B864–B871, Nov 1964.
- [22] J.C Stoddart and N.H March. Density-functional theory of magnetic instabilities in metals. *Annals of Physics*, 64(1):174–210, 1971.

Supplementary information

- [23] J C Stoddart and P Hanks. The exchange and correlation energy of a spin-polarised electron gas. *Journal of Physics C: Solid State Physics*, 10(16):3167–3178, aug 1977.
- [24] Neil Ashcroft and Davic Mermin. *Solid State Physics*. Brooks and Cole, 1976.
- [25] A. Alexandradinata and Leonid Glazman. Geometric phase and orbital moment in quantization rules for magnetic breakdown. *Phys. Rev. Lett.*, 119:256601, Dec 2017.
- [26] M. Reed and B. Simon. *Methods of Modern Mathematical Physics. IV Analysis of Operators*. Academic Press, New York, 1978.
- [27] John C. Inkson. *Green's Functions of the Single-Particle Schrödinger Equation*, pages 27–41. Springer US, Boston, MA, 1984.
- [28] T. Dieck. *Algebraic Topology*. EMS textbooks in mathematics. European Mathematical Society, 2008.
- [29] M. Born and V. Fock. Beweis des adiabatenatzes. *Zeitschrift fur Physik*, 51:165–180, mar 1928.
- [30] Hassler Whitney. Differentiable manifolds. *Annals of Mathematics*, 37(3):645–680, 1936.
- [31] J.L. Kelley. *General Topology*. Graduate Texts in Mathematics. Springer New York, 1975.
- [32] V. Guillemin and A. Pollack. *Differential Topology*. AMS Chelsea Publishing. AMS Chelsea Pub., 2010.
- [33] M.W. Hirsch. *Differential Topology*. Graduate Texts in Mathematics. Springer New York, 2012.
- [34] H.P. Cartan. *Differential Calculus*. Kershaw, 1971.
- [35] A. Bohm and M. Loewe. *Quantum Mechanics: Foundations and Applications*. Springer study edition. Springer New York, 1993.
- [36] Lochlainn O’Raifeartaigh and Norbert Straumann. Gauge theory: Historical origins and some modern developments. *Rev. Mod. Phys.*, 72:1–23, Jan 2000.
- [37] T. Akitsu. *Symmetry (Group Theory) and Mathematical Treatment in Chemistry*. IntechOpen, 2018.

Supplementary information

- [38] Di Xiao, Ming-Che Chang, and Qian Niu. Berry phase effects on electronic properties. *Rev. Mod. Phys.*, 82:1959–2007, Jul 2010.
- [39] B.A. Bernevig and T.L. Hughes. *Topological Insulators and Topological Superconductors*. Princeton University Press, 2013.
- [40] A. Alexandradinata, Zhijun Wang, and B. Andrei Bernevig. Topological insulators from group cohomology. *Phys. Rev. X*, 6:021008, Apr 2016.
- [41] Nicola Marzari, Arash A. Mostofi, Jonathan R. Yates, Ivo Souza, and David Vanderbilt. Maximally localized Wannier functions: Theory and applications. *Reviews of Modern Physics*, 84(4):1419–1475, October 2012.
- [42] M Gradhand, DV Fedorov, Falko Pientka, P Zahn, I Mertig, and BL Györffy. First-principle calculations of the berry curvature of bloch states for charge and spin transport of electrons. *Journal of Physics: Condensed Matter*, 24(21):213202, 2012.
- [43] F. D. M. Haldane. Berry Curvature on the Fermi Surface: Anomalous Hall Effect as a Topological Fermi-Liquid Property. *Physical Review Letters*, 93(20), November 2004.
- [44] Jairo Sinova, Sergio O. Valenzuela, J. Wunderlich, C. H. Back, and T. Jungwirth. Spin Hall effects. *Reviews of Modern Physics*, 87(4):1213–1260, October 2015.
- [45] Jairo Sinova, Dimitrie Culcer, Q. Niu, N. A. Sinitsyn, T. Jungwirth, and A. H. MacDonald. Universal Intrinsic Spin Hall Effect. *Physical Review Letters*, 92(12), March 2004.
- [46] M Gradhand, D V Fedorov, F Pientka, P Zahn, I Mertig, and B L Györffy. First-principle calculations of the Berry curvature of Bloch states for charge and spin transport of electrons. *Journal of Physics: Condensed Matter*, 24(21):213202, May 2012.
- [47] M.I. Dyakonov and V.I. Perel. Current-induced spin orientation of electrons in semiconductors. *Physics Letters A*, 35(6):459–460, 1971.
- [48] Shigeki Onoda, Naoyuki Sugimoto, and Naoto Nagaosa. Intrinsic versus extrinsic anomalous hall effect in ferromagnets. *Phys. Rev. Lett.*, 97:126602, Sep 2006.
- [49] A. Hoffmann. Spin hall effects in metals. *IEEE Transactions on Magnetism*, 49(10):5172–5193, Oct 2013.

Supplementary information

- [50] Jairo Sinova, Sergio O. Valenzuela, J. Wunderlich, C. H. Back, and T. Jungwirth. Spin hall effects. *Rev. Mod. Phys.*, 87:1213–1260, Oct 2015.
- [51] T. Jungwirth, Qian Niu, and A. H. MacDonald. Anomalous hall effect in ferromagnetic semiconductors. *Phys. Rev. Lett.*, 88:207208, May 2002.
- [52] Enke Liu, Yan Sun, Nitesh Kumar, Lukas Muechler, Aili Sun, Lin Jiao, Shuo-Ying Yang, Defa Liu, Aiji Liang, Qiunan Xu, Johannes Kroder, Vicky Süß, Horst Borrmann, Chandra Shekhar, Zhaosheng Wang, Chuanying Xi, Wenhong Wang, Walter Schnelle, Steffen Wirth, Yulin Chen, Sebastian T. B. Goennenwein, and Claudia Felser. Giant anomalous Hall effect in a ferromagnetic kagome-lattice semimetal. *Nature Physics*, 14(11):1125–1131, November 2018.
- [53] T. Miyasato, N. Abe, T. Fujii, A. Asamitsu, S. Onoda, Y. Onose, N. Nagaosa, and Y. Tokura. Crossover Behavior of the Anomalous Hall Effect and Anomalous Nernst Effect in Itinerant Ferromagnets. *Physical Review Letters*, 99(8), August 2007.
- [54] Ajaya K. Nayak, Julia Erika Fischer, Yan Sun, Binghai Yan, Julie Karel, Alexander C. Komarek, Chandra Shekhar, Nitesh Kumar, Walter Schnelle, Jürgen Kübler, Claudia Felser, and Stuart S. P. Parkin. Large anomalous Hall effect driven by a nonvanishing Berry curvature in the noncolinear antiferromagnet Mn_3Ge . *Science Advances*, 2(4):e1501870, April 2016.
- [55] Jürgen Kübler and Claudia Felser. Weyl Fermions in antiferromagnetic Mn_3Sn and Mn_3Ge . *EPL (Europhysics Letters)*, 120(4):47002, November 2017. arXiv: 1711.03891.
- [56] Changgan Zeng, Yugui Yao, Qian Niu, and Hanno H. Weitering. Linear Magnetization Dependence of the Intrinsic Anomalous Hall Effect. *Physical Review Letters*, 96(3), January 2006.
- [57] Zhong Fang, Naoto Nagaosa, Kei S. Takahashi, Atsushi Asamitsu, Roland Mathieu, Takeshi Ogasawara, Hiroyuki Yamada, Masashi Kawasaki, Yoshinori Tokura, and Kiyoyuki Terakura. The anomalous hall effect and magnetic monopoles in momentum space. *Science*, 302(5642):92–95, 2003.
- [58] I.M. Imort, P. Thomas, G. Reiss, and A. Thomas. Anomalous Hall effect in the Co-based Heusler compounds Co_2FeSi and Co_2FeAl . *Journal of Applied Physics*, 111(7):07D313, 2012.

- [59] Jen-Chuan Tung and Guang-Yu Guo. High spin polarization of the anomalous Hall current in Co-based Heusler compounds. *New Journal of Physics*, 15(3):033014, 2013.
- [60] Anastasios Markou, Dominik Kriegner, Jacob Gayles, Liguozhang, Yi-Cheng Chen, Benedikt Ernst, Yu-Hong Lai, Walter Schnelle, Ying-Hao Chu, Yan Sun, and Claudia Felser. Thickness dependence of the anomalous hall effect in thin films of the topological semimetal Co_2MnGa . *Phys. Rev. B*, 100:054422, Aug 2019.
- [61] Pavel Středa. Anomalous hall conductivity: Local orbitals approach. *Phys. Rev. B*, 82:045115, Jul 2010.
- [62] T. Tanaka, H. Kontani, M. Naito, T. Naito, D. S. Hirashima, K. Yamada, and J. Inoue. Intrinsic spin hall effect and orbital hall effect in 4d and 5d transition metals. *Phys. Rev. B*, 77:165117, Apr 2008.
- [63] G. Y. Guo, S. Murakami, T.-W. Chen, and N. Nagaosa. Intrinsic spin hall effect in platinum: First-principles calculations. *Phys. Rev. Lett.*, 100:096401, Mar 2008.
- [64] E. Derunova, Y. Sun, C. Felser, S. S. P. Parkin, B. Yan, and M. N. Ali. Giant intrinsic spin Hall effect in W_3Ta and other A15 superconductors. *Science Advances*, 5(4), 2019.
- [65] Frank Freimuth, Stefan Blügel, and Yuriy Mokrousov. Spin-orbit torques in $\text{Co}/\text{Pt}(111)$ and $\text{Mn}/\text{W}(001)$ magnetic bilayers from first principles. *Phys. Rev. B*, 90:174423, Nov 2014.
- [66] E.S. Fedorov. *Symmetry of Crystals*. ACA monograph. American Crystallographic Association, 1971.
- [67] Wolfgang Tremel and Roald Hoffmann. Square nets of main-group elements in solid-state materials. *Journal of the American Chemical Society*, 109(1):124–140, 1987.
- [68] G. Y. Guo, S. Murakami, T.-W. Chen, and N. Nagaosa. Intrinsic spin hall effect in platinum: First-principles calculations. *Phys. Rev. Lett.*, 100:096401, Mar 2008.
- [69] M. Morota, Y. Niimi, K. Ohnishi, D. H. Wei, T. Tanaka, H. Kontani, T. Kimura, and Y. Otani. Indication of intrinsic spin hall effect in 4d and 5d transition metals. *Phys. Rev. B*, 83:174405, May 2011.
- [70] Qiang Hao, Wenzhe Chen, and Gang Xiao. Beta (β) tungsten thin films: structure, electron transport, and giant spin hall effect. *Applied Physics Letters*, 106(18):182403, 2015.

- [71] Kai-Uwe Demasius, Timothy Phung, Weifeng Zhang, Brian P Hughes, See-Hun Yang, Andrew Kellock, Wei Han, Aakash Pushp, and Stuart SP Parkin. Enhanced spin-orbit torques by oxygen incorporation in tungsten films. *Nature communications*, 7, 2016.
- [72] Weifeng Zhang, Wei Han, Xin Jiang, See-Hun Yang, and Stuart SP Parkin. Role of transparency of platinum-ferromagnet interfaces in determining the intrinsic magnitude of the spin hall effect. *Nature Physics*, 11(6):496–502, 2015.
- [73] Q. D. Gibson, L. M. Schoop, L. Muechler, L. S. Xie, M. Hirschberger, N. P. Ong, R. Car, and R. J. Cava. Three-dimensional dirac semimetals: Design principles and predictions of new materials. *Phys. Rev. B*, 91:205128, May 2015.
- [74] Hoi Chun Po, Ashvin Vishwanath, and Haruki Watanabe. Symmetry-based indicators of band topology in the 230 space groups. *Nature Communications*, 8(1):50, 2017.
- [75] Satoru Nakatsuji, Naoki Kiyohara, and Tomoya Higo. Large anomalous hall effect in a non-collinear antiferromagnet at room temperature. *Nature*, 2015.
- [76] Ajaya K. Nayak, Julia Erika Fischer, Yan Sun, Binghai Yan, Julie Karel, Alexander C. Komarek, Chandra Shekhar, Nitesh Kumar, Walter Schnelle, Jürgen Kübler, Claudia Felser, and Stuart S. P. Parkin. Large anomalous hall effect driven by a nonvanishing berry curvature in the noncolinear antiferromagnet mn₃ge. *Science Advances*, 2(4), 2016.
- [77] Chi-Feng Pai, Luqiao Liu, Y. Li, H. W. Tseng, D. C. Ralph, and R. A. Buhrman. Spin transfer torque devices utilizing the giant spin hall effect of tungsten. *Applied Physics Letters*, 101(12):122404, 2012.
- [78] G.R. Stewart. Superconductivity in the a15 structure. *Physica C: Superconductivity and its Applications*, 514:28 – 35, 2015.
- [79] Barry Bradlyn, Jennifer Cano, Zhijun Wang, M. G. Vergniory, C. Felser, R. J. Cava, and B. Andrei Bernevig. Beyond dirac and weyl fermions: Unconventional quasiparticles in conventional crystals. *Science*, 353(6299), 2016.
- [80] A.V. Narlikar. *Superconductors*. OUP Oxford, 2014.
- [81] Mohsin Z Minhas, Avanindra K Pandeya, Bharat Grover, Alessandro Fumarola, Ilya Kostanovskiy, Binoy K Hazra, Wolfgang Hoppe, Georg Woltersdorf, Amilcar Bedoya-Pinto,

Supplementary information

- Stuart S P Parkin, and Mazhar N Ali. Doping-induced spin hall ratio enhancement in a15-phase, ta-doped β -w thin films. *Journal of Physics: Materials*, 3(4):044001, aug 2020.
- [82] N. P. Ong. Geometric interpretation of the weak-field hall conductivity in two-dimensional metals with arbitrary fermi surface. *Phys. Rev. B*, 43:193–201, Jan 1991.
- [83] V.A. Toponogov and V. Rovenski. *Differential Geometry of Curves and Surfaces: A Concise Guide*. Birkhauser Boston, 2006.
- [84] J. Jost and J. Jost. *Riemannian Geometry and Geometric Analysis*. Springer Universitat texts. Springer, 2005.
- [85] H. Poincaré. Sur l’uniformisation des fonctions analytiques. *Acta Math.*, 31:1–63, 1908.
- [86] William Abikoff. The uniformization theorem. *The American Mathematical Monthly*, 88(8):574–592, 1981.
- [87] T. Poston and I. Stewart. *Catastrophe Theory and Its Applications*. Dover books on mathematics. Dover Publications, 1996.
- [88] Li Ye, Yuan Tian, Xiaofeng Jin, and Di Xiao. Temperature dependence of the intrinsic anomalous hall effect in nickel. *Phys. Rev. B*, 85:220403, Jun 2012.
- [89] William P. Thurston. Three dimensional manifolds, kleinian groups and hyperbolic geometry. *Bull. Amer. Math. Soc.*, (6):357–381, 1982.
- [90] G. Perelman. Finite extinction time for the solutions to the ricci flow on certain three-manifolds. *Topologica*, 1(1):005, 2008.

Publications

1. "Fermi Surface local Geometry", .
E. Derunova, J. Gayles, Y. Sun, M.Gaultois, and M. N. Ali.
submitted to Nature. Physics (2021)
2. "Giant Intrinsic Spin Hall Effect in W3Ta and other A15 Superconductors" .
E. Derunova , Y. Sun, C. Felser, S. S. P. Parkin, B. Yan and M. N. Ali
Science Advances 05 Apr 2019, DOI:10.1126/sciadv.aav8575 (2019)
3. "Linking Symmetry, Crystallography, Topology, and Fundamental Physics in Crystalline Solids".
E. Derunova , M. N. Ali.
Chapter in the book "Symmetry (Group Theory) and Mathematical Treatment in Chemistry". July 18th 2018. DOI: 10.5772/intechopen.74175 (2018)
4. "Hard magnetic topological semimetals in XPt3 compounds with harmony of Berry curvature" .
A. Markou, J.Gayles, **E. Derunova**, P. Swekis, J. Noky, L. Zhang, M.Ali, Y. Sun, and C. Felser
accepted for publication in Nature. Communications Physics (2021)
5. "Large, unconventional anomalous Hall effect in the topological frustrated magnet candidate, KV₃Sb₅"
S.-Y. Yang, Y. Wang, B. R. Ortiz, D. Liu, J. Gayles,**E. Derunova**, R. G.-Hernandez, L. Smejkal, Y. Chen, S. S. P. Parkin, S. D. Wilson, E. S. Toberer, T. McQueen, M. N. Ali
Science Advances, 31 Jul 2020: Vol. 6, no. 31. DOI: 10.1126/sciadv.abb6003 (2020)
6. "Band structure engineering of chemically tunable LnSbTe (Ln = La, Ce, Pr)"
A. Weiland, D. G. Chaparro, M. G. Vergniory, **E. Derunova** , J. Yoon, I. W. H. Oswald,

Publications

G. T. McCandless, M. Ali, and J. Y. Chan

APL Materials 7, 101113 (2019) DOI:10.1063/1.5123396 (2019)

7. “Symmetry demanded topological Nodal-line materials”.

S.-Y. Yang, H. Yang, **E. Derunova**, S. S. P. Parkin, B. Yan and M. N. Ali

Advances in Physics: X, 3, 1414631 (2018)

Acknowledgments

This work is dedicated to my father, Derunov Vladimir, who was a researcher in thin film materials and had been inspiring me to study physics from a very young age to the time he passed away.

The special thanks I'd like to give the Dr. Maz for the faith, passion and patience, whilst supervising this work. His openness and enthusiasm let me step inside the doors of quantum material science. I highly appreciate the given me opportunity to work in Sofia Kovalevskaja group independently and self-sufficient, but at the same time getting help and experience from colleagues.

Additionally, I'd like to acknowledge Dr. Parkin for building excellent environment in the NISE department of MPI-Halle. The unique combination of facilities and people selected by Dr. Parkin created a unique possibility to carry out research in best conditions. Also I'd like to thanks all the colleague for making PhD time to a fun and exciting experience, especially Elisa, Alessandro and the whole Mango team. Also I'd like to notice efforts of the secretaries and particularly, Simone.

In the end I'd like to thank Alice Dee for inspiring me over all this time.

Acknowledgments

Curriculum Vitae

Elena Derunova

Max Planck Institute of Microstructure Physics

Weinberg 2

Halle (Saale), Germany, 06120

(+49) 17675163045

ederunov@mpi-halle.mpg.de

EDUCATION

PhD candidate in Physics

December 2016 - Present

Max Planck Institute of Microstructure Physics, Germany

Supervisors: prof. Dr. M.N. Ali, prof. Dr. S. Parkin.

Master of Science

2010 - 2012

Voronezh State University, Voronezh, Russia, with honors.

Specialization: Mathematics. Computer science.

Thesis “Bifurcations of extremals of Fredholm functionals with a circular symmetry”

Supervisor prof. Dr. Y. Sapronov

Bachelor of Science

Curriculum Vitae

2006 - 2010

Voronezh State University, Voronezh, Russia, with honors.

Specialization: Mathematics. Applied mathematics.

Thesis “Bifurcations of extremals of Fredholm functionals with a circular symmetry in case of resonance 1:2:4.”

Supervisor prof. Dr. Y. Sapronov

Eidesstattliche Erklärung

Hiermit erkläre ich, Elena Derunova, dass ich die vorliegende Arbeit mit dem Titel: **Fermi Surface Local Geometry and Anomalous Quantum Transport** in allen Teilen selbständig verfasst und keine anderen als die angegebenen Quellen und Hilfsmittel benutzt habe. Alle wörtlich oder sinngemäß übernommenen Textstellen habe ich als solche kenntlich gemacht.

Ferner liegen gegen mich weder gerichtliche Vorstrafen vor, noch sind staatsanwaltliche Ermittlungen oder Disziplinarverfahren eingeleitet worden.

Des Weiteren erkläre ich hiermit, dass ich bisher keine andere Arbeit zur Promotion eingereicht noch mit einer anderen Arbeit den Versuch zur Promotion unternommen habe.

Halle (Saale), 15.06.2021

Elena Derunova